Lithos 340–341 (2019) 287–315

Contents lists available at ScienceDirect

Lithos

journal homepage: www.elsevier.com/locate/lithos

# Petrogenesis and tectonic implications of the Eocene-Oligocene potassic felsic suites in western Yunnan, eastern Tibetan Plateau: Evidence from petrology, zircon chronology, elemental and Sr-Nd-Pb-Hf isotopic geochemistry

Xin Tong [a,b], Zhidan Zhao [a,*], Yaoling Niu [a,c,d,e], Shuangquan Zhang [b], Brian Cousens [b], Dong Liu [a], Yong Zhang [a], Meizhi Han [a], Yuanxin Zhao [a], Hangshan Lei [a], Qingshang Shi [a], Di-Cheng Zhu [a], Lawangin Sheikh [a], Wasiq Lutfi [a]

[a] State Key Laboratory of Geological Processes and Mineral Resources, and School of Earth Science and Resources, China University of Geosciences, Beijing 100083, China
[b] Isotope Geochemistry and Geochronology Research Centre, Ottawa-Carleton-Geoscience Centre, Department of Earth Sciences, Carleton University, Ottawa, ON K1S 5B6, Canada
[c] Department of Earth Sciences, Durham University, Durham DH1 3LE, UK
[d] Laboratory for Marine Geology, Qingdao National Laboratory for Marine Science and Technology, Qingdao 266061, China
[e] Institute of Oceanology, Chinese Academy of Sciences, Qingdao 266071, China

ARTICLE INFO

*Article history:*
Received 4 March 2019
Accepted 29 April 2019
Available online 06 May 2019

*Keywords:*
Sr-Nd-Pb isotopes
Geochronology
Potassic magmatism
Lithospheric removal
Eastern Tibetan Plateau
Western Yunnan

ABSTRACT

In western Yunnan, potassic felsic suites with important Cu mineralization have been interpreted as being genetically associated with the Ailao Shan-Red River (ASRR) shear zone. In this paper, we show that the magmatism is unrelated to the shear zone, but shares many characteristics in common with potassic suites along the Jinsha suture to the north and northwest on the northern Tibetan Plateau, representing a magmatic response to the continued India-Asia convergence since the collision in the early Eocene. These felsic suites include syenite, monzogranite porphyries and granite porphyries. We dated 15 representative samples using zircon U-Pb method that gives a tight emplacement age of ~37–35 Ma. On 45 representative samples, we have done bulk-rock major element, trace element and Sr-Nd-Pb isotope analysis. We use these data, together with zircon Hf isotope data and the literature data on potassic mafic suites in the region to discuss the petrogenesis of these rocks. We conclude that the petrogenesis of the felsic potassic suites is most consistent with a scenario of deep (≥ 40 km) melting of thickened crust. The crustal melting is caused by intrusion and underplating of potassic mafic melts derived from melting of metasomatized mantle lithosphere. The mafic potassic suites in the region result from such mantle melts. Mixing of the mafic melts with the felsic melts explains the syenite and monzogranite porphyries and their extended fractional crystallization gives rise to the granite porphyries. The potassic suites along the Jinsha suture, including those from northern Tibet, western Yunnan and Vietnam, share the same tectonic setting during the Eocene-Oligocene. In response to the continued India-Asia convergence, removal of the lower continental lithospheric mantle triggered by Rayleigh-Taylor convective instability induces asthenosphere upwelling, partial melting of the metasomatized mantle lithosphere. We hypothesize that the eastward migration of the potassic magmatism along the Jinsha suture in the period of Eocene-Oligocene results from eastward thickening and removing of the continental lithospheric mantle along the suture, which, in time and space, correlates with the dischronal subduction of the torn Indian continental slab at ca. 52 Ma along the India-Asia collision zone.



## 1. Introduction

Potassic magmas carry important messages on the structure and composition of the crust and mantle, and thus allow studying deep geodynamic processes and associated mineralization in varying tectonic settings (e.g. Cousens et al., 2004, 2011; Guo et al., 2005; Huang et al., 2010; Lu et al., 2013). A cluster of Eocene-Oligocene potassic igneous rocks occur along the Jinsha suture in the Sanjinag and Northern Tibet regions with a number of large associated porphyry Cu-Mo and Cu-Au deposits (Chung et al., 2005). There have been many studies on potassic-ultrapotassic magmatic rocks from this belt over the past several decades (see Deng et al., 2014 for a review), but disputes remain on their petrogenesis.

In western Yunnan, potassic felsic suites, many associated with porphyry Cu-Au deposits, occur along the ASRR (Ailaoshan-Red River)

* Corresponding author at: State Key Laboratory of Geological Processes and Mineral Resources, and School of Earth Science and Resources, China University of Geosciences, Beijing 100083, China.
*E-mail address:* zdzhao@cugb.edu.cn (Z. Zhao).

https://doi.org/10.1016/j.lithos.2019.04.023
0024-4937/

shear zone (He et al., 2016; Huang et al., 2010; Lu et al., 2012), with emplacement ages ranging from 40 Ma to 23 Ma (c.f. Lu et al., 2012). Diverse interpretations exist on the petrogenesis of these rocks and the mineralization. The Eocene-Oligocene potassic suites in western Yunnan have long been thought to have a genetic relationship with the ASRR shear zone (e.g. Guo et al., 2005; Liang et al., 2006; Liang et al., 2007; Schärer et al., 1994; Zhang and Schärer, 1999). However, other studies argue that emplacement of these potassic suites predates the initiation of the ASRR shear zone (e.g. Cao et al., 2011; Chung et al., 2008; Lu et al., 2012). The petrogenesis of these rocks is also controversial. He et al. (2016) proposed that all of the Eocene felsic intrusions in western Yunnan were derived from partial melting of a subduction-modified thickened lower crust with some incorporation of mafic melts. However, some studies divide the potassic felsic rocks into compositionally separate suites, giving different petrogenetic interpretations. The shoshonitic syenites and quartz monzonites may result from congenetic shoshonitic mafic melts by fractional crystallization, the potassic quartz monzonites may be derived by mixing between lower-crustal felsic melts and shoshonitic mantle mafic melts, whereas the potassic adakite-like granites may have formed from partial melting of a thickened mafic lower crust (Chen et al., 2017; Lu et al., 2013). In addition, Chen et al. (2017) proposed that all the granites in western Yunnan were generated by partial melting of an ancient crust. Mafic components are generally assumed to originate from partial melting of a metasomatically enriched continental lithospheric mantle (e.g. Chen et al., 2017; Guo et al., 2005; Huang et al., 2010; Lu et al., 2015). Yet, mantle metasomatic processes and cause or causes that may have triggered the magmatism remain controversial (e.g., Deng et al., 2014; He et al., 2016; Huang et al., 2010; Lu et al., 2013, 2015; Wang et al., 2001; Xu et al., 2001).

To address these issues, we carried out a systematic study of the Eocene-Oligocene potassic felsic igneous rocks and their hosted enclaves from western Yunnan using a combined approach of electron probe microanalysis, zircon geochronology, bulk-rock elemental and Sr-Nd-Pb isotope geochemistry as well as zircon Hf isotopic systematics. We have also used geothermobarometric and thermodynamic models to constrain the compositional and physical conditions of the potassic magmatic system. The available database, including new and literature data, allow us (1) to reveal the nature and petrogenesis of the potassic felsic rocks, (2) to clarify their relationship with the mafic counterparts in the magmatic system along the ASRR shear zone, (3) to provide better constraints on the metasomatic history of the mantle and the physical control on the potassic magmatism beneath western Yangtze Craton, and (4) to better understand the deep geodynamic processes of the Eocene-Oligocene time period along the entire Jinsha suture. In this paper, we report the results of this study, which underscore the importance of potassic rocks in a post-collisional setting to reveal geodynamic processes in the deep earth by means of petrology, geochemistry and thermodynamic modelling.

## 2. Geological setting and sampling

The Tibetan Plateau formed via the closure of the Paleotethyan ocean and subsequent amalgamation of Gondwana-derived micro-continental blocks and Paleozoic arc terranes (Zhu et al., 2013). It consists primarily of three terranes, which are, from south to north, the Lhasa terrane, Qiangtang terrane (Simao-Indochina Block in western Yunnan) and Songpan-Ganze terrane, separated by the Bangong-Nujiang and Jinsha sutures, respectively (Fig. 1).

The Jinsha suture, also termed Jinshajiang-Ailaoshan suture zone, extends over 2000 km from Tibet to the Ailaoshan area in western Yunnan. It is represented by the Jinshajiang ophiolitic belt and Weixi arc in eastern Tibet, and Ailaoshan ophiolitic belt and Mojiang-Luchun arc in the Ailaoshan area in western Yunnan (Yang, 1998). In the Sanjiang region, it separates the Yangtze Craton from the Simao-Indochina Block (Figs. 1b, 2).

The Sanjiang region is named because it is geographically the drainage/catchment region shared by the three major rivers (the Jinshajiang, Lancangjiang, and Nujiang), which covers western Yunnan Province and the southeastern part of the Tibetan Plateau. Ore deposits of varying types, such as porphyry-skarn Cu-Au, were formed in the region during the Cenozoic, makes it one of the most productive regions with great metal resources prospect in China (Deng et al., 2014).

After the amalgamation, large-scale Cenozoic geological processes, such as the ongoing India-Asia collision/convergence and distant seafloor plate subduction, have continue to re-shaped the lithospheric structure of the Tibet Plateau, especially the Sanjiang region (Deng et al., 2014). The lithosphere has been shortened, accommodated by underthrusting of the Indian continental lithosphere, thickening of the Asian lithosphere, and in part by southeastward extrusion tectonics facilitated by strike-slip motion along the NW-SE-trending Ailao Shan-Red River (ASRR) shear zone (Leloup et al., 1995; Tapponnier et al., 1990).

The ASRR shear zone extends over 1000 km from SW China through Vietnam, and into the South China Sea along the western margin of the Yangtze Craton (Leloup et al., 1995; Tapponnier et al., 1990). The shear zone locally overprints the Jinsha suture. Dismembered ophiolitic fragments of the Jinsha suture are well exposed in the vicinity of the shear zone in the Ailaoshan area (Leloup et al., 1995). The ASRR shear zone is a sinistral strike-slip fault that allowed the Indochina Block to be extruded southeastward in response to the India-Asia collision (Tapponnier et al., 1990). The Yangtze Craton lies to the southeast of the Tibetan Plateau, separated from the Simao-Indochina Block by the ASRR shear zone and the Jinsha suture (Fig. 1, Li et al., 2008).

The potassic igneous belt occurs along the Jinsha suture across North Tibet and the Sanjiang regions from Fenghuoshan to Lüchun County (Chung et al., 2005; Guo et al., 2005; Huang et al., 2010; Lu et al., 2012). In northern Vietnam, the potassic suites exposed in FanSiPan on the belt were also reported (Phan, 1991). All these potassic suites have been dated to be emplaced between ca. 45 Ma and 33 Ma (Guo et al., 2006; Hou et al., 2003; Liang et al., 2007; Zhang and Schärer, 1999).

The potassic felsic rocks intrude sedimentary country rocks in the form of stocks widely exposed in western Yunnan (Fig. 2). All the samples of this study are least altered intrusions from Machangqing, Liuhe and Jianchuan (Table 1) on the west margin of the Yangtze craton.

## 3. Petrography

The samples are light- or grey-colored, medium- to coarse-grained with porphyritic texture. According to the mineral assemblage, these samples are divided into three groups. They are syenite porphyries, monzogranite porphyries, and granite porphyries.

Syenite porphyries were collected from Jianchuan and Liuhe (Fig. 3a). At Jianchuan, the potassic feldspar and amphibole phenocrysts commonly appear tabular. Clinopyroxene, biotite, and plagioclase are also observed in the matrix, although some are altered to clays (Fig. 4b). At Liuhe, the syenite porphyries contain K-feldspar phenocrysts, clinopyroxene, amphibole, plagioclase and minor biotite, with accessory titanite, apatite, zircon and iron oxides (Fig. 3b, c, Fig. 4a). Of the major phenocrysts, K-feldspar and amphibole are euhedral to subhedral, whereas clinopyroxene and plagioclase are subhedral to anhedral (Fig. 4a). Abundant mafic microgranular enclaves (MMEs) and xenoliths, including garnet-clinopyroxene granulite, garnet-bearing pyroxene granulite, garnet amphibolite, amphibolite, and biotite gneiss, are present in Liuhe syenite porphyry and have sharp contacts with the host (Fig. 3b, c). Chilled margins and reaction rims are common around these enclaves (Fig. 3c). Xenoliths of garnet-clinopyroxene granulites have homeoblastic texture, consisting primarily of, subhedral to anhedral, garnet (Gt), clinopyroxene (Cpx), amphibole (Amp) and plagioclase (Pl) with minor rutile (Ru) (Fig. 4c, d). Orthopyroxene (Opx) is absent. Concentric opaque and amphibole

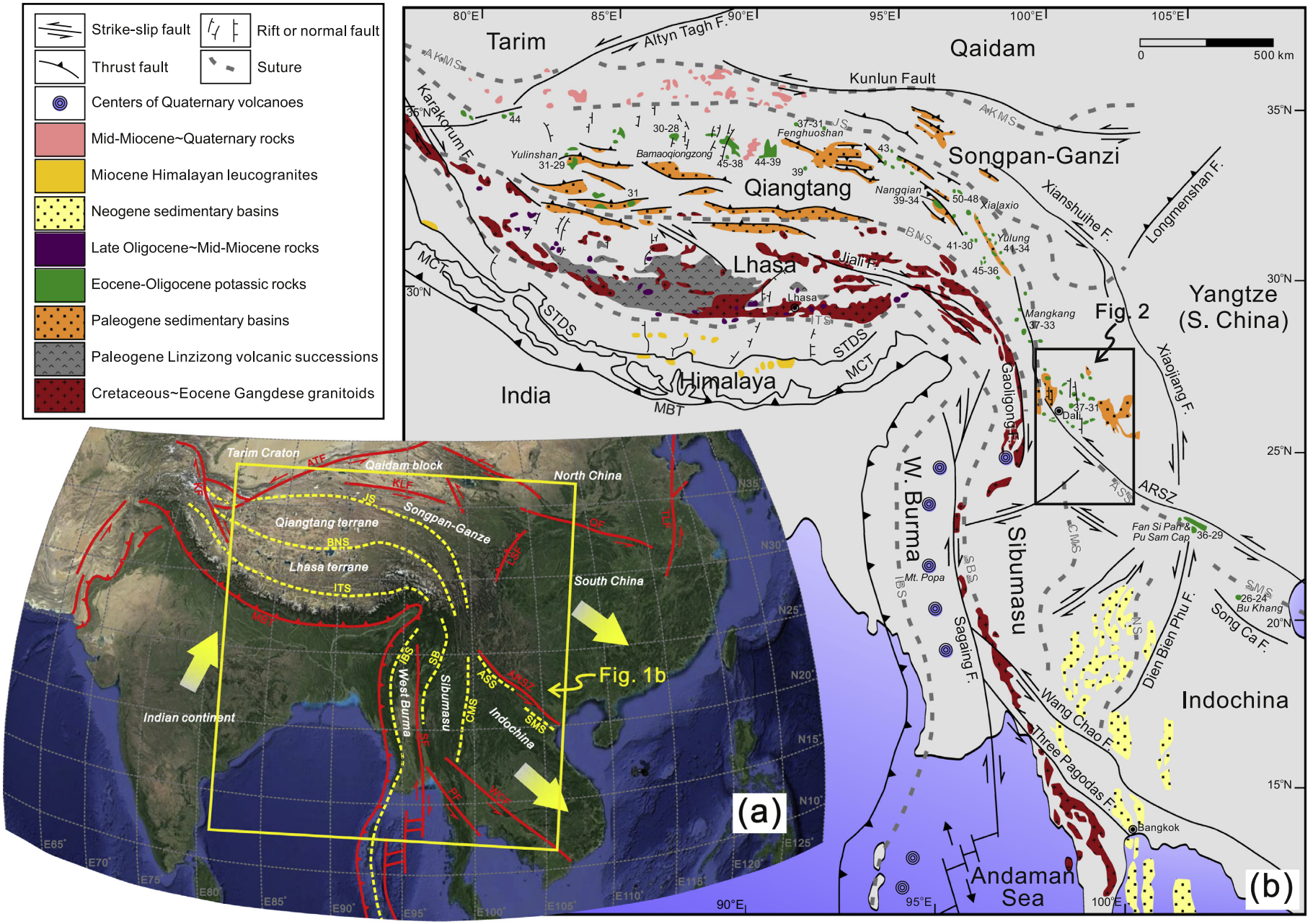


**Fig. 1.** (a) Distribution of principal continental blocks affecting the tectonic evolution of Tibetan Plateau (modified after Tapponnier et al., 1990; Chung et al., 2005, 2008; Deng et al., 2014, suing the Google Earth base map); (b) Simplified tectonic map of the Tibetan Plateau showing major Cenozoic magmatic rocks (modified from Leloup et al., 1995; Chung et al., 2005, 2008). Abbreviation: AKMS, Anyimaqin-Kunlun-Muztagh suture; JS, Jinsha suture; BNS, Bangong-Nujiang suture; ITS, Indus-Tsangpo suture; MBT, Main Boundary Thrust; ARSZ, Ailaoshan-Red River shear zone; KF, Karakorum Fault; ATF, Altyn Tagh Fault; KLF, Kunlun Fault; QF, Qinling Fault; TLF, Tancheng-Lushan Fault; LSF, Longmenshan Fault; IBS, Indus-Burma suture; SB, Shan Boundary; SF, Sagaing Fault; PF, Three Pagodas Fault; WCF, Wang Chao Fault; CMS, Changning Menglian suture; ASS, Ailaoshan suture; SMS, Song Ma suture; MCT, Main Central Thrust; STDS, South Tibet Detachment System. (For interpretation of the references to colour in this figure legend, the reader is referred to the web version of this article.)

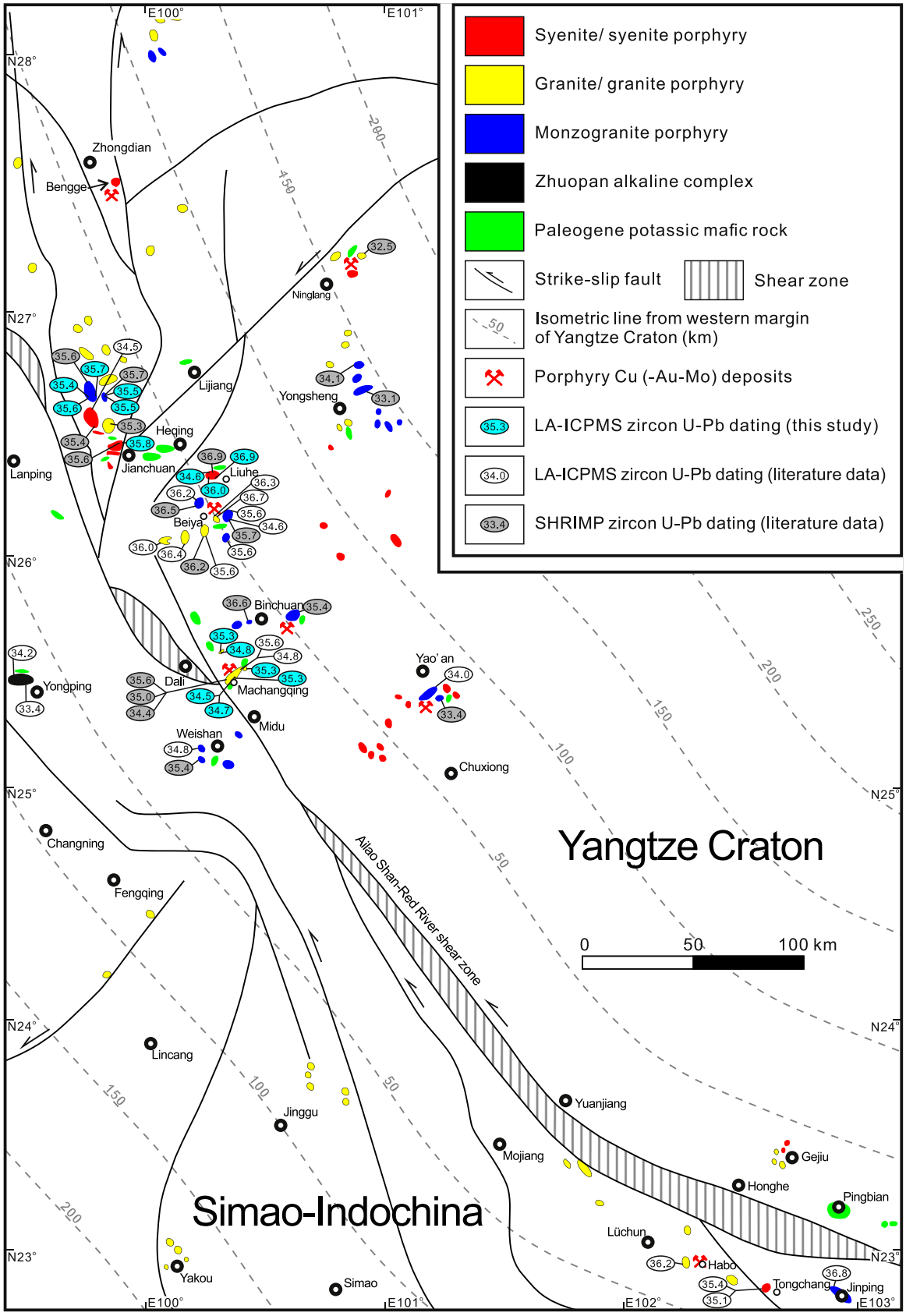


**Fig. 2.** Simplified geological map showing the distribution and age of Cenozoic potassic felsic intrusions in western Yunnan (modified from Guo et al., 2005; Huang et al., 2010; Lu et al., 2013). Literature data are from Liang et al. (2007), Lu et al. (2012) and references therein.

**Table 1**
Major oxide (wt%), trace element (ppm) and whole-rock Sr-Nd-Pb compositons of Eocene-Oligocene potassic felsic intrusions in western Yunnan.

| No. | 1 | 2 | 3 | 4 | 5 | 6 | 7 | 8 |
|---|---|---|---|---|---|---|---|---|
| Sample | XY1503 | XY1504 | XY1509 | XY1510 | XY1511 | XY1513 | XY1515 | XY1517 |
| Locality | Machangqing | Machangqing | Machangqing | Machangqing | Machangqing | Machangqing | Machangqing | Machangqing |
| Latitude | 25°32′40.5” | 25°32′59.5” | 25°31′32.9” | 25°31′32.9” | 25°31′32.9” | 25°31′32.9” | 25°31′32.9” | 25°31′14.3” |
| Longitude | 100°30′45.7” | 100°30′43.9” | 100°26′26.8” | 100°26′26.8” | 100°26′26.8” | 100°26′26.8” | 100°26′26.8” | 100°26′10.0” |
| Lithology | GP | GP | GP | GP | GP | GP | GP | GP |
| $SiO_2$ | 68.77 | 62.08 | 69.45 | 68.79 | 72.69 | 65.04 | 71.07 | 70.56 |
| $TiO_2$ | 0.29 | 0.61 | 0.37 | 0.37 | 0.21 | 0.44 | 0.31 | 0.33 |
| $Al_2O_3$ | 16.53 | 16.27 | 14.93 | 15.04 | 15.19 | 15.81 | 15.49 | 13.69 |
| $Fe_2O_3$ | 1.50 | 4.71 | 2.57 | 2.48 | 0.99 | 2.33 | 1.74 | 2.24 |
| MnO | 0.01 | 0.05 | 0.01 | 0.01 | 0.01 | 0.02 | 0.02 | 0.02 |
| MgO | 0.17 | 1.51 | 1.43 | 1.40 | 0.29 | 1.45 | 0.35 | 1.35 |
| CaO | 0.53 | 3.73 | 1.44 | 1.52 | 0.21 | 2.01 | 0.27 | 2.09 |
| $Na_2O$ | 4.27 | 4.31 | 3.76 | 3.72 | 4.12 | 3.11 | 3.72 | 4.14 |
| $K_2O$ | 5.81 | 4.76 | 4.43 | 4.65 | 4.82 | 6.76 | 5.03 | 3.98 |
| $P_2O_5$ | 0.03 | 0.48 | 0.11 | 0.16 | 0.04 | 0.23 | 0.15 | 0.17 |
| LOI | 1.41 | 0.87 | 1.03 | 1.05 | 1.32 | 1.98 | 1.73 | 0.55 |
| Total | 99.32 | 99.38 | 99.53 | 99.20 | 99.89 | 99.17 | 99.88 | 99.12 |
| Mg# | 0.18 | 0.39 | 0.52 | 0.53 | 0.37 | 0.55 | 0.28 | 0.54 |
| $K_2O/Na_2O$ | 1.36 | 1.10 | 1.18 | 1.25 | 1.17 | 2.17 | 1.35 | 0.96 |
| A/CNK | 1.16 | 0.86 | 1.10 | 1.08 | 1.23 | 0.98 | 1.28 | 0.92 |
| Li | 12.5 | 18.3 | 31.3 | 24.2 | 15.2 | 54.9 | 16.6 | 12.5 |
| Be | 5.40 | 3.86 | 4.05 | 4.52 | 3.70 | 4.25 | 3.76 | 4.09 |
| Sc | 3.23 | 9.23 | 5.10 | 5.46 | 2.77 | 5.68 | 4.16 | 4.47 |
| V | 14.4 | 76.5 | 43.5 | 51.3 | 26.2 | 42.6 | 39.4 | 38.9 |
| Cr | 1.72 | 41.4 | 35.4 | 33.9 | 7.82 | 20.4 | 43.9 | 37.4 |
| Co | 0.76 | 13.7 | 8.49 | 5.03 | 5.52 | 6.33 | 6.97 | 5.21 |
| Ni | 0.99 | 23.5 | 22.4 | 21.9 | 5.22 | 20.4 | 43.1 | 23.1 |
| Cu | 2.19 | 19.7 | 199 | 268 | 339 | 611 | 483 | 8.92 |
| Zn | 46.2 | 50.4 | 17.9 | 20.7 | 11.6 | 27.3 | 35.8 | 23.2 |
| Ga | 22.7 | 21.3 | 20.8 | 21.7 | 21.3 | 20.7 | 21.3 | 20.4 |
| Rb | 210 | 154 | 205 | 212 | 251 | 263 | 319 | 165 |
| Sr | 231 | 1818 | 531 | 572 | 300 | 692 | 492 | 684 |
| Y | 31.8 | 21.6 | 9.33 | 14.1 | 5.19 | 15.8 | 9.00 | 12.5 |
| Zr | 478 | 252 | 162 | 200 | 114 | 184 | 142 | 172 |
| Nb | 31.7 | 16.7 | 10.5 | 12.2 | 5.86 | 13.3 | 5.77 | 11.2 |
| Sn | 1.90 | 0.92 | 1.55 | 1.71 | 1.61 | 1.49 | 2.23 | 1.30 |
| Cs | 3.17 | 4.37 | 5.55 | 5.00 | 6.16 | 6.61 | 7.28 | 3.35 |
| Ba | 393 | 2780 | 983 | 953 | 627 | 1686 | 966 | 1453 |
| La | 187 | 123 | 45.6 | 72.2 | 17.7 | 89.3 | 36.6 | 55.3 |
| Ce | 342 | 217 | 78.1 | 119 | 29.8 | 155 | 60.1 | 96.1 |
| Pr | 34.9 | 22.8 | 7.79 | 12.1 | 3.29 | 16.0 | 6.89 | 9.96 |
| Nd | 118 | 82.0 | 25.2 | 41.3 | 12.1 | 57.7 | 23.3 | 35.3 |
| Sm | 16.5 | 11.7 | 3.80 | 5.81 | 2.19 | 8.20 | 3.82 | 5.14 |
| Eu | 2.75 | 2.59 | 0.79 | 1.15 | 0.37 | 1.66 | 0.68 | 1.01 |
| Gd | 9.97 | 7.48 | 2.61 | 3.86 | 1.61 | 5.30 | 2.55 | 3.49 |
| Tb | 1.28 | 0.92 | 0.33 | 0.52 | 0.21 | 0.63 | 0.31 | 0.47 |
| Dy | 6.35 | 4.44 | 1.68 | 2.61 | 1.06 | 3.16 | 1.57 | 2.22 |
| Ho | 1.08 | 0.73 | 0.31 | 0.47 | 0.18 | 0.55 | 0.26 | 0.41 |
| Er | 3.15 | 2.02 | 0.90 | 1.33 | 0.51 | 1.54 | 0.72 | 1.20 |
| Tm | 0.43 | 0.26 | 0.13 | 0.20 | 0.09 | 0.22 | 0.11 | 0.17 |
| Yb | 2.78 | 1.61 | 0.80 | 1.22 | 0.49 | 1.32 | 0.62 | 1.05 |
| Lu | 0.43 | 0.24 | 0.14 | 0.18 | 0.07 | 0.21 | 0.10 | 0.16 |
| Hf | 11.6 | 6.15 | 4.48 | 5.61 | 3.44 | 5.13 | 4.07 | 5.03 |
| Ta | 1.84 | 1.07 | 0.82 | 0.95 | 0.69 | 1.00 | 0.54 | 0.89 |
| Tl | 0.59 | 0.24 | 1.29 | 1.35 | 1.55 | 1.63 | 2.29 | 0.87 |
| Pb | 41.8 | 24.4 | 14.2 | 19.3 | 16.1 | 24.1 | 12.9 | 34.4 |
| Th | 68.7 | 35.7 | 24.4 | 28.3 | 12.9 | 30.4 | 17.8 | 25.7 |
| U | 11.3 | 7.93 | 5.21 | 6.87 | 3.51 | 11.7 | 4.92 | 8.89 |
| $Eu/Eu^*$ | 0.66 | 0.85 | 0.76 | 0.74 | 0.60 | 0.77 | 0.67 | 0.73 |
| Sr/Y | 7.25 | 84.32 | 56.93 | 40.42 | 57.75 | 43.65 | 54.66 | 54.92 |
| La/Yb | 67.51 | 76.57 | 56.74 | 59.29 | 36.48 | 67.72 | 58.78 | 52.52 |
| $(La/Yb)_N$ | 48.43 | 54.92 | 40.70 | 42.53 | 26.17 | 48.58 | 42.16 | 37.67 |
| Dy/Yb | 2.29 | 2.76 | 2.09 | 2.14 | 2.19 | 2.40 | 2.52 | 2.11 |
| $^{87}Sr/^{86}Sr$ | 0.708520 | 0.707152 | – | – | – | – | – | – |
| $^{87}Sr/^{86}Sr_{(i)}$ | 0.707168 | 0.707027 | – | – | – | – | – | – |
| $^{143}Nd/^{144}Nd$ | 0.512220 | 0.512286 | – | – | – | – | – | – |
| $^{143}Nd/^{144}Nd_{(i)}$ | 0.512201 | 0.512266 | – | – | – | – | – | – |
| $\varepsilon Nd_{(t)}$ | −7.6 | −6.4 | – | – | – | – | – | – |
| $T_{DM}$ (Ma) | 1099 | 1032 | – | – | – | – | – | – |
| $^{206}Pb/^{204}Pb$ | 18.475 | 18.501 | – | – | – | – | – | – |
| $^{207}Pb/^{204}Pb$ | 15.607 | 15.604 | – | – | – | – | – | – |
| $^{208}Pb/^{204}Pb$ | 39.057 | 39.023 | – | – | – | – | – | – |

(continued on next page)

**Table 1** (*continued*)

| No. | 9 | 10 | 11 | 12 | 13 | 14 | 15 | 16 |
|---|---|---|---|---|---|---|---|---|
| Sample | XY1518 | XY1519 | XY1520 | BC1501 | BC1503 | BC1504 | BC1505 | HQBT02-J |
| Locality | Machangqing | Machangqing | Machangqing | Machangqing | Machangqing | Machangqing | Machangqing | Liuhe |
| Latitude | 25°31′14.3” | 25°31′14.3” | 25°31′14.3” | 25°39′14.5” | 25°39′14.5” | 25°39′14.5” | 25°39′14.5” | 26°28′16.8” |
| Longitude | 100°26′10.0” | 100°26′10.0” | 100°26′10.0” | 100°22′7.1” | 100°22′7.1” | 100°22′7.1” | 100°22′7.1” | 100°18′55.3” |
| Lithology | GP | GP | GP | GP | GP | GP | GP | SP |
| $SiO_2$ | 69.02 | 68.07 | 60.24 | 64.35 | 64.31 | 63.76 | 64.04 | 59.97 |
| $TiO_2$ | 0.35 | 0.29 | 0.53 | 0.49 | 0.52 | 0.42 | 0.48 | 0.75 |
| $Al_2O_3$ | 14.96 | 16.08 | 15.72 | 15.30 | 15.02 | 14.43 | 15.09 | 14.32 |
| $Fe_2O_3$ | 2.11 | 1.19 | 5.68 | 3.81 | 4.24 | 5.83 | 4.37 | 4.99 |
| MnO | 0.02 | 0.02 | 0.02 | 0.06 | 0.08 | 0.09 | 0.07 | 0.09 |
| MgO | 1.09 | 1.17 | 2.22 | 2.01 | 2.18 | 1.96 | 2.14 | 2.74 |
| CaO | 2.03 | 2.38 | 2.13 | 2.88 | 3.49 | 2.48 | 3.01 | 4.59 |
| $Na_2O$ | 4.22 | 4.71 | 3.78 | 4.09 | 4.03 | 3.81 | 4.21 | 3.81 |
| $K_2O$ | 4.75 | 4.73 | 5.75 | 4.71 | 4.32 | 5.12 | 4.53 | 6.19 |
| $P_2O_5$ | 0.12 | 0.10 | 0.44 | 0.38 | 0.32 | 0.33 | 0.37 | 0.48 |
| LOI | 0.62 | 1.62 | 3.82 | 1.07 | 1.26 | 0.97 | 0.84 | 1.10 |
| Total | 99.29 | 100.36 | 100.33 | 99.16 | 99.77 | 99.20 | 99.15 | 99.03 |
| Mg# | 0.51 | 0.66 | 0.44 | 0.51 | 0.50 | 0.40 | 0.49 | 0.52 |
| $K_2O/Na_2O$ | 1.13 | 1.00 | 1.52 | 1.15 | 1.07 | 1.34 | 1.08 | 1.62 |
| A/CNK | 0.95 | 0.94 | 0.96 | 0.90 | 0.85 | 0.88 | 0.87 | 0.67 |
| Li | 19.3 | 15.5 | 57.1 | 12.0 | 10.6 | 9.47 | 10.7 | 20.2 |
| Be | 4.54 | 3.15 | 7.46 | 3.99 | 5.16 | 4.24 | 5.06 | 5.96 |
| Sc | 3.65 | 3.99 | 7.82 | 7.12 | 7.38 | 6.06 | 6.65 | 13.4 |
| V | 34.4 | 33.3 | 71.9 | 61.4 | 62.1 | 63.4 | 57.3 | 94.4 |
| Cr | 20.5 | 28.9 | 19.0 | 38.0 | 42.5 | 37.2 | 39.7 | 80.9 |
| Co | 4.96 | 15.4 | 9.86 | 9.92 | 11.3 | 11.6 | 10.2 | 14.2 |
| Ni | 13.5 | 18.9 | 18.0 | 27.1 | 27.7 | 28.4 | 25.1 | 42.1 |
| Cu | 54.8 | 3.96 | 63.7 | 227 | 181 | 316 | 414 | 36.9 |
| Zn | 17.6 | 13.6 | 22.6 | 85.9 | 105 | 123 | 136 | 58.6 |
| Ga | 20.1 | 21.1 | 22.1 | 19.8 | 20.1 | 19.8 | 19.7 | 18.9 |
| Rb | 191 | 207 | 460 | 142 | 152 | 142 | 145 | 220 |
| Sr | 742 | 838 | 833 | 1446 | 1269 | 1279 | 1297 | 780 |
| Y | 15.2 | 8.18 | 19.4 | 21.1 | 23.1 | 21.3 | 21.6 | 20.4 |
| Zr | 173 | 122 | 221 | 229 | 225 | 199 | 212 | 207 |
| Nb | 15.0 | 6.45 | 16.6 | 17.3 | 19.0 | 12.8 | 19.4 | 12.4 |
| Sn | 1.64 | 1.25 | 4.47 | 1.41 | 1.38 | 1.19 | 1.50 | 1.68 |
| Cs | 4.06 | 4.49 | 21.9 | 1.64 | 1.50 | 1.75 | 1.96 | 6.59 |
| Ba | 1224 | 1676 | 2323 | 2176 | 1903 | 2432 | 1793 | 2106 |
| La | 72.3 | 33.2 | 114 | 104 | 109 | 95.0 | 107 | 32.4 |
| Ce | 124 | 60.0 | 207 | 187 | 197 | 157 | 187 | 62.7 |
| Pr | 12.7 | 6.52 | 22.5 | 19.8 | 20.4 | 16.9 | 19.2 | 7.15 |
| Nd | 44.8 | 22.9 | 82.7 | 72.1 | 74.7 | 61.0 | 67.9 | 26.9 |
| Sm | 6.34 | 3.70 | 12.1 | 10.7 | 11.2 | 8.98 | 9.86 | 5.36 |
| Eu | 1.35 | 0.78 | 2.58 | 2.23 | 2.39 | 2.02 | 2.11 | 1.19 |
| Gd | 4.38 | 2.54 | 7.32 | 7.22 | 7.65 | 6.10 | 6.71 | 4.73 |
| Tb | 0.56 | 0.32 | 0.87 | 0.85 | 0.92 | 0.75 | 0.79 | 0.67 |
| Dy | 2.76 | 1.53 | 3.88 | 4.04 | 4.40 | 3.61 | 3.79 | 3.64 |
| Ho | 0.47 | 0.25 | 0.65 | 0.69 | 0.74 | 0.63 | 0.66 | 0.72 |
| Er | 1.40 | 0.71 | 1.82 | 1.92 | 2.14 | 1.81 | 1.89 | 1.99 |
| Tm | 0.19 | 0.10 | 0.21 | 0.25 | 0.27 | 0.23 | 0.25 | 0.28 |
| Yb | 1.25 | 0.61 | 1.38 | 1.55 | 1.75 | 1.55 | 1.57 | 1.81 |
| Lu | 0.18 | 0.09 | 0.20 | 0.24 | 0.26 | 0.23 | 0.25 | 0.26 |
| Hf | 5.03 | 3.45 | 5.42 | 5.84 | 5.88 | 5.22 | 5.64 | 5.71 |
| Ta | 1.19 | 0.54 | 1.03 | 1.14 | 1.42 | 1.03 | 1.37 | 0.73 |
| Tl | 1.19 | 1.41 | 2.66 | 0.98 | 1.00 | 0.93 | 0.96 | 1.54 |
| Pb | 23.3 | 20.9 | 9.42 | 57.1 | 60.6 | 65.9 | 80.2 | 32.0 |
| Th | 33.9 | 14.1 | 33.4 | 41.5 | 44.8 | 37.4 | 44.8 | 9.84 |
| U | 10.5 | 5.01 | 11.5 | 8.26 | 9.76 | 8.16 | 10.3 | 3.65 |
| Eu/Eu* | 0.78 | 0.78 | 0.84 | 0.77 | 0.79 | 0.83 | 0.79 | 0.72 |
| Sr/Y | 48.77 | 102.50 | 42.85 | 68.45 | 54.91 | 59.99 | 59.96 | 38.22 |
| La/Yb | 57.71 | 53.98 | 82.32 | 67.37 | 62.57 | 61.42 | 68.44 | 17.92 |
| $(La/Yb)_N$ | 41.39 | 38.72 | 59.05 | 48.33 | 44.88 | 44.05 | 49.09 | 12.85 |
| Dy/Yb | 2.20 | 2.48 | 2.80 | 2.61 | 2.51 | 2.33 | 2.42 | 2.01 |
| $^{87}Sr/^{86}Sr$ | – | – | – | 0.707184 | – | – | – | – |
| $^{87}Sr/^{86}Sr_{(i)}$ | – | – | – | 0.707038 | – | – | – | – |
| $^{143}Nd/^{144}Nd$ | – | – | – | 0.512208 | – | – | – | – |
| $^{143}Nd/^{144}Nd_{(i)}$ | – | – | – | 0.512187 | – | – | – | – |
| $\varepsilon Nd_{(t)}$ | – | – | – | −7.9 | – | – | – | – |
| $T_{DM}$ (Ma) | – | – | – | 1158 | – | – | – | – |
| $^{206}Pb/^{204}Pb$ | – | – | – | 18.467 | – | – | – | – |
| $^{207}Pb/^{204}Pb$ | – | – | – | 15.603 | – | – | – | – |
| $^{208}Pb/^{204}Pb$ | – | – | – | 38.952 | – | – | – | – |

(*continued on next page*)

**Table 1** (*continued*)

| No. | 17 | 18 | 19 | 20 | 21 | 22 | 23 | 24 |
|---|---|---|---|---|---|---|---|---|
| Sample | HQBT11-J | HQBT14-J | LHB1728–2 | JC1701 | JC1702 | JC1703 | JC1504 | JC1506 |
| Locality | Liuhe | Liuhe | Liuhe | Jianchuan | Jianchuan | Jianchuan | Jianchuan | Jianchuan |
| Latitude | 26°26′58.5" | 26°26′40.6" | 26°28′45.8″ | 26°32′32.9″ | 26°32′32.9″ | 26°32′32.9″ | 26°26′51.5" | 26°26′51.5" |
| Longitude | 100°18′21.6" | 100°19′41.5" | 100°18′36.8″ | 99°53′51.6″ | 99°53′51.6″ | 99°53′51.6″ | 99°51′51.7" | 99°51′51.7" |
| Lithology: | SP | SP | SP | SP | SP | SP | SP | SP |
| $SiO_2$ | 65.96 | 61.01 | 61.90 | 61.98 | 62.22 | 61.67 | 58.99 | 61.24 |
| $TiO_2$ | 0.43 | 0.70 | 0.68 | 0.61 | 0.61 | 0.63 | 0.79 | 0.69 |
| $Al_2O_3$ | 14.85 | 14.38 | 14.44 | 14.94 | 15.35 | 15.01 | 13.39 | 14.72 |
| $Fe_2O_3$ | 2.81 | 4.61 | 4.53 | 5.41 | 5.23 | 5.40 | 6.67 | 6.23 |
| MnO | 0.05 | 0.07 | 0.08 | 0.10 | 0.10 | 0.11 | 0.10 | 0.09 |
| MgO | 1.18 | 2.27 | 2.27 | 1.82 | 1.39 | 1.67 | 3.90 | 2.24 |
| CaO | 3.01 | 4.31 | 4.39 | 3.91 | 3.27 | 3.71 | 4.00 | 3.17 |
| $Na_2O$ | 4.16 | 3.50 | 3.93 | 3.86 | 4.09 | 3.92 | 2.80 | 3.51 |
| $K_2O$ | 6.16 | 6.49 | 6.16 | 6.26 | 6.43 | 6.23 | 6.75 | 6.70 |
| $P_2O_5$ | 0.26 | 0.41 | 0.41 | 0.32 | 0.31 | 0.34 | 0.52 | 0.66 |
| LOI | 0.55 | 1.95 | 0.87 | 0.41 | 0.36 | 0.58 | 1.27 | 0.86 |
| Total | 99.42 | 99.69 | 99.65 | 99.61 | 99.37 | 99.28 | 99.17 | 100.11 |
| Mg# | 0.45 | 0.49 | 0.50 | 0.40 | 0.34 | 0.38 | 0.54 | 0.42 |
| $K_2O/Na_2O$ | 1.48 | 1.86 | 1.57 | 1.62 | 1.57 | 1.59 | 2.41 | 1.91 |
| A/CNK | 0.78 | 0.70 | 0.68 | 0.74 | 0.78 | 0.75 | 0.70 | 0.78 |
| Li | 21.6 | 22.4 | 18.6 | 24.9 | 22.2 | 22.6 | 22.3 | 22.4 |
| Be | 6.61 | 4.86 | 5.66 | 7.90 | 6.80 | 6.93 | 7.86 | 8.36 |
| Sc | 7.53 | 12.2 | 12.0 | 10.1 | 9.81 | 10.0 | 15.8 | 11.4 |
| V | 48.3 | 89.3 | 87.0 | 96.5 | 93.4 | 94.3 | 123 | 95.7 |
| Cr | 31.1 | 70.6 | 68.1 | 33.5 | 32.1 | 33.7 | 200 | 89.0 |
| Co | 6.20 | 12.4 | 12.3 | 10.3 | 10.3 | 10.9 | 21.3 | 13.1 |
| Ni | 16.0 | 34.6 | 36.5 | 14.6 | 14.9 | 15.4 | 119 | 47.4 |
| Cu | 7.33 | 31.9 | 31.0 | 36.1 | 57.9 | 34.5 | 29.9 | 41.1 |
| Zn | 43.4 | 53.6 | 62.4 | 78.9 | 70.8 | 77.2 | 58.7 | 75.3 |
| Ga | 18.7 | 17.6 | 18.6 | 20.7 | 21.4 | 21.1 | 19.2 | 20.5 |
| Rb | 242 | 230 | 218 | 244 | 261 | 242 | 304 | 301 |
| Sr | 904 | 808 | 854 | 1527 | 1576 | 1513 | 907 | 1244 |
| Y | 14.0 | 19.7 | 19.1 | 33.9 | 36.0 | 33.3 | 31.4 | 28.6 |
| Zr | 184 | 205 | 206 | 262 | 290 | 272 | 240 | 252 |
| Nb | 11.2 | 12.4 | 12.6 | 15.9 | 16.5 | 16.1 | 14.2 | 15.5 |
| Sn | 1.47 | 1.73 | 1.73 | 2.81 | 2.82 | 2.96 | 2.77 | 2.42 |
| Cs | 6.77 | 3.89 | 6.07 | 11.4 | 12.8 | 8.88 | 6.38 | 9.17 |
| Ba | 2128 | 2202 | 2185 | 2078 | 2092 | 1972 | 1830 | 2084 |
| La | 26.3 | 30.0 | 31.8 | 56.5 | 57.6 | 57.4 | 49.0 | 48.1 |
| Ce | 51.0 | 60.1 | 60.9 | 106 | 107 | 109 | 102 | 97.8 |
| Pr | 5.76 | 6.81 | 6.83 | 11.8 | 12.2 | 12.5 | 11.3 | 10.7 |
| Nd | 20.7 | 26.3 | 25.9 | 45.7 | 46.3 | 47.1 | 45.3 | 42.0 |
| Sm | 3.99 | 5.14 | 5.07 | 9.09 | 9.39 | 9.58 | 9.22 | 8.49 |
| Eu | 0.71 | 1.08 | 1.32 | 2.19 | 2.26 | 2.19 | 2.24 | 2.15 |
| Gd | 3.23 | 4.57 | 4.38 | 7.60 | 7.77 | 7.89 | 7.46 | 6.70 |
| Tb | 0.47 | 0.64 | 0.63 | 1.12 | 1.14 | 1.11 | 1.05 | 0.97 |
| Dy | 2.48 | 3.67 | 3.46 | 5.90 | 6.24 | 6.08 | 5.67 | 5.17 |
| Ho | 0.47 | 0.66 | 0.64 | 1.07 | 1.12 | 1.09 | 1.07 | 0.94 |
| Er | 1.33 | 1.94 | 1.84 | 3.10 | 3.27 | 3.13 | 2.81 | 2.67 |
| Tm | 0.18 | 0.27 | 0.25 | 0.44 | 0.46 | 0.45 | 0.40 | 0.40 |
| Yb | 1.16 | 1.71 | 1.67 | 2.74 | 2.89 | 2.87 | 2.61 | 2.56 |
| Lu | 0.18 | 0.26 | 0.25 | 0.44 | 0.46 | 0.47 | 0.37 | 0.38 |
| Hf | 5.33 | 5.55 | 5.36 | 6.98 | 7.42 | 7.16 | 6.25 | 6.74 |
| Ta | 0.68 | 0.73 | 0.71 | 1.06 | 1.08 | 1.09 | 0.90 | 1.06 |
| Tl | 1.81 | 1.59 | 1.34 | 2.08 | 2.03 | 1.55 | 1.92 | 1.90 |
| Pb | 38.2 | 30.6 | 46.1 | 76.7 | 61.0 | 50.9 | 30.8 | 40.8 |
| Th | 10.6 | 9.52 | 9.67 | 24.0 | 26.6 | 25.5 | 17.9 | 21.5 |
| U | 3.79 | 2.56 | 3.33 | 6.62 | 6.93 | 6.56 | 2.78 | 4.50 |
| Eu/Eu* | 0.60 | 0.68 | 0.80 | 0.80 | 0.81 | 0.77 | 0.83 | 0.87 |
| Sr/Y | 64.33 | 41.12 | 44.61 | 45.00 | 43.74 | 45.46 | 28.93 | 43.51 |
| La/Yb | 22.57 | 17.57 | 19.03 | 20.61 | 19.91 | 19.97 | 18.77 | 18.77 |
| $(La/Yb)_N$ | 16.19 | 12.60 | 14.78 | 14.78 | 14.28 | 14.33 | 13.46 | 13.46 |
| Dy/Yb | 2.13 | 2.15 | 2.07 | 2.15 | 2.15 | 2.12 | 2.17 | 2.02 |
| $^{87}Sr/^{86}Sr$ | 0.707774 | 0.707670 | 0.707695 | – | 0.707410 | – | – | 0.707655 |
| $^{87}Sr/^{86}Sr_{(i)}$ | 0.707377 | 0.707247 | 0.707316 | – | 0.707164 | – | – | 0.707296 |
| $^{143}Nd/^{144}Nd$ | 0.512354 | 0.512345 | 0.512346 | – | 0.512450 | – | – | 0.512418 |
| $^{143}Nd/^{144}Nd_{(i)}$ | 0.512327 | 0.512318 | 0.512319 | – | 0.512422 | – | – | 0.512390 |
| $\varepsilon Nd_{(t)}$ | −5.2 | −5.4 | −5.4 | – | −3.3 | – | – | −4.0 |
| $T_{DM}$ (Ma) | 1251 | 1286 | 1285 | – | 1172 | – | – | 1219 |
| $^{206}Pb/^{204}Pb$ | 18.615 | 18.586 | 18.557 | – | 18.678 | – | – | 18.698 |
| $^{207}Pb/^{204}Pb$ | 15.660 | 15.652 | 15.649 | – | 15.629 | – | – | 15.634 |
| $^{208}Pb/^{204}Pb$ | 38.935 | 38.881 | 38.849 | – | 38.785 | – | – | 38.813 |

(*continued on next page*)

**Table 1** (*continued*)

| No. | 25 | 26 | 27 | 28 | 29 | 30 | 31 | 32 |
|---|---|---|---|---|---|---|---|---|
| Sample | JC1508 | JC1509 | JC1510 | JC1511 | JC1513 | LJ1501 | LJ1502 | LJ1503 |
| Locality | Jianchuan | Jianchuan | Jianchuan | Jianchuan | Jianchuan | Jianchuan | Jianchuan | Jianchuan |
| Latitude | 26°33′003” | 26°33′003” | 26°35′02.2” | 26°35′02.2” | 26°35′29.1” | 26°47′24.9” | 26°47′24.3” | 26°47′21.8” |
| Longitude | 99°54′37.8” | 99°54′37.8” | 99°55′12.7” | 99°55′12.7” | 99°53′56.8” | 99°49′21.8” | 99°49′07.2” | 99°48′52.5” |
| Lithology | SP | SP | SP | SP | SP | MGP | MGP | MGP |
| $SiO_2$ | 58.23 | 57.22 | 61.88 | 60.84 | 63.04 | 69.69 | 68.78 | 69.39 |
| $TiO_2$ | 0.80 | 0.88 | 0.63 | 0.65 | 0.54 | 0.27 | 0.32 | 0.28 |
| $Al_2O_3$ | 14.69 | 14.24 | 14.97 | 14.92 | 15.69 | 15.18 | 15.78 | 15.39 |
| $Fe_2O_3$ | 7.42 | 7.96 | 5.27 | 5.47 | 4.27 | 1.76 | 1.83 | 1.86 |
| MnO | 0.12 | 0.15 | 0.09 | 0.11 | 0.07 | 0.03 | 0.03 | 0.03 |
| MgO | 2.22 | 2.51 | 1.67 | 1.69 | 1.70 | 0.58 | 0.57 | 0.55 |
| CaO | 4.13 | 4.33 | 3.65 | 4.37 | 3.75 | 2.11 | 2.20 | 2.08 |
| $Na_2O$ | 3.80 | 2.63 | 3.73 | 3.76 | 3.58 | 4.70 | 4.94 | 4.81 |
| $K_2O$ | 6.94 | 7.79 | 6.28 | 6.42 | 4.37 | 3.85 | 3.94 | 3.86 |
| $P_2O_5$ | 0.64 | 0.60 | 0.31 | 0.31 | 0.38 | 0.20 | 0.18 | 0.16 |
| LOI | 0.84 | 1.78 | 0.77 | 0.72 | 2.51 | 0.66 | 0.46 | 0.91 |
| Total | 99.83 | 100.09 | 99.25 | 99.26 | 99.90 | 99.04 | 99.03 | 99.32 |
| Mg# | 0.37 | 0.38 | 0.39 | 0.38 | 0.44 | 0.39 | 0.38 | 0.37 |
| $K_2O/Na_2O$ | 1.83 | 2.96 | 1.68 | 1.71 | 1.22 | 0.82 | 0.80 | 0.80 |
| A/CNK | 0.69 | 0.69 | 0.76 | 0.71 | 0.90 | 0.96 | 0.96 | 0.97 |
| Li | 31.5 | 27.5 | 23.4 | 22.7 | 16.6 | 18.5 | 14.0 | 19.8 |
| Be | 5.17 | 8.68 | 6.73 | 8.27 | 4.75 | 4.31 | 4.52 | 4.45 |
| Sc | 11.9 | 13.8 | 9.52 | 9.85 | 9.24 | 3.05 | 3.07 | 2.90 |
| V | 134 | 155 | 93.2 | 97.4 | 65.9 | 23.9 | 25.1 | 23.3 |
| Cr | 33.6 | 35.1 | 35.4 | 36.0 | 38.7 | 2.15 | 2.13 | 2.79 |
| Co | 15.2 | 15.1 | 9.87 | 10.3 | 8.98 | 2.82 | 2.99 | 2.72 |
| Ni | 19.1 | 19.4 | 14.5 | 14.8 | 17.4 | 1.48 | 1.54 | 1.53 |
| Cu | 39.2 | 78.7 | 33.1 | 30.4 | 19.5 | 0.78 | 0.74 | 0.92 |
| Zn | 93.4 | 104 | 75.9 | 73.0 | 73.3 | 42.1 | 33.7 | 53.0 |
| Ga | 21.8 | 21.0 | 21.1 | 20.5 | 21.0 | 21.7 | 22.6 | 21.1 |
| Rb | 269 | 281 | 264 | 261 | 152 | 132 | 132 | 125 |
| Sr | 2233 | 2578 | 1592 | 1627 | 1550 | 1403 | 1528 | 1309 |
| Y | 37.2 | 43.7 | 33.6 | 31.1 | 38.1 | 9.72 | 10.3 | 9.19 |
| Zr | 346 | 345 | 255 | 262 | 233 | 126 | 129 | 122 |
| Nb | 19.8 | 17.5 | 15.9 | 15.2 | 12.5 | 7.57 | 7.72 | 7.48 |
| Sn | 3.79 | 3.83 | 2.58 | 2.87 | 1.89 | 1.37 | 1.44 | 1.40 |
| Cs | 10.2 | 8.70 | 8.24 | 4.94 | 4.48 | 6.88 | 6.47 | 7.19 |
| Ba | 2934 | 3446 | 2228 | 2283 | 1966 | 1651 | 1671 | 1595 |
| La | 67.1 | 75.1 | 56.3 | 51.7 | 52.7 | 21.8 | 22.7 | 20.2 |
| Ce | 135 | 146 | 109 | 105 | 107 | 42.0 | 43.1 | 39.2 |
| Pr | 15.1 | 16.7 | 12.0 | 11.3 | 11.3 | 4.76 | 4.92 | 4.53 |
| Nd | 59.0 | 66.3 | 45.8 | 43.1 | 43.5 | 18.5 | 18.9 | 17.4 |
| Sm | 11.9 | 13.2 | 9.18 | 8.68 | 8.59 | 3.41 | 3.58 | 3.28 |
| Eu | 2.97 | 3.24 | 2.27 | 2.20 | 1.87 | 0.94 | 0.96 | 0.89 |
| Gd | 9.17 | 10.6 | 7.44 | 7.10 | 7.04 | 2.59 | 2.66 | 2.44 |
| Tb | 1.30 | 1.47 | 1.06 | 1.04 | 1.00 | 0.33 | 0.35 | 0.32 |
| Dy | 6.95 | 7.88 | 5.83 | 5.41 | 5.73 | 1.69 | 1.81 | 1.66 |
| Ho | 1.28 | 1.44 | 1.11 | 1.02 | 1.12 | 0.29 | 0.31 | 0.29 |
| Er | 3.38 | 3.82 | 2.98 | 2.83 | 3.29 | 0.77 | 0.81 | 0.77 |
| Tm | 0.48 | 0.54 | 0.45 | 0.42 | 0.51 | 0.11 | 0.12 | 0.12 |
| Yb | 3.12 | 3.44 | 2.86 | 2.70 | 3.20 | 0.74 | 0.76 | 0.74 |
| Lu | 0.44 | 0.50 | 0.42 | 0.39 | 0.47 | 0.10 | 0.11 | 0.11 |
| Hf | 8.97 | 8.93 | 6.74 | 6.92 | 6.17 | 4.02 | 4.16 | 4.01 |
| Ta | 1.28 | 1.10 | 1.04 | 0.99 | 0.83 | 0.55 | 0.58 | 0.55 |
| Tl | 0.76 | 0.73 | 1.64 | 1.44 | 0.47 | 0.98 | 0.95 | 1.07 |
| Pb | 80.4 | 62.4 | 51.2 | 43.2 | 52.8 | 49.9 | 44.8 | 48.6 |
| Th | 31.0 | 28.7 | 23.8 | 23.0 | 20.9 | 8.88 | 9.59 | 9.13 |
| U | 3.24 | 2.78 | 6.20 | 6.28 | 6.22 | 2.86 | 3.22 | 2.57 |
| $Eu/Eu^*$ | 0.87 | 0.84 | 0.84 | 0.86 | 0.74 | 0.97 | 0.95 | 0.96 |
| Sr/Y | 59.95 | 58.94 | 47.41 | 52.28 | 40.64 | 144.35 | 147.99 | 142.55 |
| La/Yb | 21.54 | 21.80 | 19.67 | 19.13 | 16.45 | 29.51 | 29.86 | 27.42 |
| $(La/Yb)_N$ | 15.45 | 15.64 | 14.11 | 13.72 | 11.80 | 21.16 | 21.42 | 19.67 |
| Dy/Yb | 2.23 | 2.29 | 2.04 | 2.00 | 1.79 | 2.28 | 2.38 | 2.25 |
| $^{87}Sr/^{86}Sr$ | – | – | 0.707407 | – | – | 0.705784 | – | – |
| $^{87}Sr/^{86}Sr_{(i)}$ | – | – | 0.707162 | – | – | 0.705645 | – | – |
| $^{143}Nd/^{144}Nd$ | – | – | 0.512410 | – | – | 0.512524 | – | – |
| $^{143}Nd/^{144}Nd_{(i)}$ | – | – | 0.512382 | – | – | 0.512498 | – | – |
| $\varepsilon Nd_{(t)}$ | – | – | −4.1 | – | – | −1.8 | – | – |
| $T_{DM}$ (Ma) | – | – | 1222 | – | – | 935 | – | – |
| $^{206}Pb/^{204}Pb$ | – | – | – | – | – | 18.666 | – | – |
| $^{207}Pb/^{204}Pb$ | – | – | – | – | – | 15.624 | – | – |
| $^{208}Pb/^{204}Pb$ | – | – | – | – | – | 38.727 | – | – |

(*continued on next page*)

**Table 1** (*continued*)

| No. | 33 | 34 | 35 | 36 | 37 | 38 | 39 | 40 |
|---|---|---|---|---|---|---|---|---|
| Sample | LJ1504 | LJ1505 | LJ1506 | LJ1507 | LJ1508 | LJ1509 | LJ1510 | LJ1511 |
| Locality | Jianchuan | Jianchuan | Jianchuan | Jianchuan | Jianchuan | Jianchuan | Jianchuan | Jianchuan |
| Latitude | 26°46′53.2” | 26°46′27.4” | 26°45′41” | 26°45′41” | 26°45′41.5” | 26°45′41.5” | 26°45′43.9” | 26°45′43.4” |
| Longitude | 99°46′32.0” | 99°45′33.7” | 99°43′29.2” | 99°43′29.2” | 99°42′51.0” | 99°42′51.0” | 99°42′13.5” | 99°42′08.7” |
| Lithology | MGP | MGP | MGP | MGP | MGP | MGP | MGP | MGP |
| $SiO_2$ | 70.28 | 68.10 | 69.09 | 67.85 | 68.61 | 67.36 | 68.61 | 65.77 |
| $TiO_2$ | 0.25 | 0.23 | 0.34 | 0.38 | 0.32 | 0.36 | 0.35 | 0.39 |
| $Al_2O_3$ | 15.55 | 14.75 | 15.01 | 15.62 | 15.32 | 15.29 | 14.82 | 14.78 |
| $Fe_2O_3$ | 1.21 | 2.86 | 2.48 | 2.69 | 2.47 | 2.72 | 2.78 | 2.85 |
| MnO | 0.01 | 0.07 | 0.04 | 0.04 | 0.04 | 0.05 | 0.05 | 0.06 |
| MgO | 0.40 | 0.38 | 0.89 | 1.03 | 0.72 | 1.01 | 0.98 | 1.24 |
| CaO | 0.98 | 1.76 | 1.75 | 2.15 | 1.44 | 2.09 | 2.18 | 2.84 |
| $Na_2O$ | 4.34 | 2.50 | 4.91 | 4.63 | 5.08 | 4.93 | 4.54 | 4.04 |
| $K_2O$ | 5.54 | 5.79 | 3.98 | 4.17 | 4.25 | 4.23 | 3.84 | 3.96 |
| $P_2O_5$ | 0.11 | 0.10 | 0.25 | 0.17 | 0.17 | 0.21 | 0.22 | 0.14 |
| LOI | 0.97 | 2.67 | 0.82 | 0.96 | 0.74 | 1.06 | 0.81 | 3.06 |
| Total | 99.64 | 99.21 | 99.56 | 99.69 | 99.16 | 99.31 | 99.18 | 99.13 |
| Mg# | 0.40 | 0.21 | 0.42 | 0.43 | 0.37 | 0.42 | 0.41 | 0.46 |
| $K_2O/Na_2O$ | 1.28 | 2.32 | 0.81 | 0.90 | 0.84 | 0.86 | 0.85 | 0.98 |
| A/CNK | 1.04 | 1.09 | 0.96 | 0.97 | 0.98 | 0.93 | 0.95 | 0.92 |
| Li | 7.88 | 4.17 | 11.4 | 13.4 | 17.0 | 18.3 | 19.6 | 21.1 |
| Be | 4.25 | 3.24 | 4.44 | 4.48 | 4.81 | 4.63 | 4.58 | 3.71 |
| Sc | 2.64 | 2.33 | 4.68 | 5.21 | 4.11 | 4.91 | 4.90 | 6.19 |
| V | 19.5 | 18.5 | 34.6 | 39.6 | 34.4 | 39.9 | 40.1 | 44.4 |
| Cr | 1.71 | 1.55 | 7.98 | 11.2 | 4.12 | 4.17 | 8.97 | 15.6 |
| Co | 2.03 | 1.89 | 4.40 | 5.21 | 3.98 | 4.98 | 4.80 | 6.18 |
| Ni | 1.00 | 1.13 | 4.69 | 6.23 | 2.68 | 3.23 | 4.70 | 7.32 |
| Cu | 112 | 17.1 | 4.10 | 5.51 | 3.49 | 4.91 | 3.61 | 4.18 |
| Zn | 15.0 | 41.7 | 40.5 | 44.5 | 43.3 | 50.9 | 52.1 | 52.2 |
| Ga | 21.3 | 20.6 | 21.0 | 21.3 | 21.8 | 21.7 | 20.8 | 19.4 |
| Rb | 203 | 246 | 130 | 142 | 131 | 131 | 136 | 127 |
| Sr | 910 | 256 | 1252 | 1329 | 1453 | 1420 | 1288 | 905 |
| Y | 9.00 | 8.41 | 13.7 | 16.3 | 13.2 | 15.1 | 15.2 | 16.7 |
| Zr | 118 | 116 | 154 | 159 | 146 | 160 | 158 | 153 |
| Nb | 7.12 | 6.66 | 8.41 | 8.69 | 8.55 | 8.79 | 8.65 | 8.58 |
| Sn | 2.35 | 1.41 | 1.50 | 1.61 | 1.58 | 1.55 | 1.55 | 1.46 |
| Cs | 2.52 | 5.39 | 4.25 | 4.68 | 2.51 | 4.72 | 6.79 | 7.39 |
| Ba | 1777 | 1762 | 1673 | 1720 | 1869 | 1834 | 1775 | 1773 |
| La | 17.5 | 19.2 | 26.1 | 33.5 | 25.8 | 28.1 | 29.9 | 27.1 |
| Ce | 32.6 | 35.8 | 50.0 | 55.8 | 49.7 | 54.3 | 52.8 | 51.4 |
| Pr | 3.76 | 4.01 | 5.84 | 7.18 | 5.76 | 6.35 | 6.53 | 5.97 |
| Nd | 14.6 | 15.0 | 22.2 | 27.2 | 22.2 | 24.3 | 24.8 | 22.7 |
| Sm | 2.92 | 2.81 | 4.28 | 5.14 | 4.27 | 4.65 | 4.74 | 4.48 |
| Eu | 0.84 | 1.03 | 1.12 | 1.33 | 1.13 | 1.25 | 1.23 | 1.10 |
| Gd | 2.21 | 2.19 | 3.32 | 3.96 | 3.20 | 3.69 | 3.69 | 3.54 |
| Tb | 0.31 | 0.30 | 0.47 | 0.56 | 0.44 | 0.49 | 0.52 | 0.52 |
| Dy | 1.54 | 1.52 | 2.34 | 2.94 | 2.33 | 2.61 | 2.71 | 2.76 |
| Ho | 0.27 | 0.26 | 0.44 | 0.54 | 0.40 | 0.47 | 0.48 | 0.54 |
| Er | 0.74 | 0.68 | 1.18 | 1.42 | 1.12 | 1.26 | 1.33 | 1.45 |
| Tm | 0.10 | 0.09 | 0.17 | 0.20 | 0.16 | 0.20 | 0.19 | 0.22 |
| Yb | 0.69 | 0.57 | 1.12 | 1.26 | 1.03 | 1.21 | 1.25 | 1.39 |
| Lu | 0.10 | 0.08 | 0.16 | 0.19 | 0.16 | 0.18 | 0.18 | 0.22 |
| Hf | 3.87 | 3.73 | 4.45 | 4.58 | 4.47 | 4.50 | 4.49 | 4.29 |
| Ta | 0.52 | 0.49 | 0.59 | 0.61 | 0.59 | 0.62 | 0.58 | 0.64 |
| Tl | 1.59 | 2.63 | 1.00 | 1.15 | 0.98 | 1.13 | 0.98 | 1.11 |
| Pb | 83.4 | 84.1 | 43.0 | 42.4 | 34.0 | 44.4 | 44.4 | 51.4 |
| Th | 8.70 | 8.06 | 10.3 | 11.4 | 11.1 | 11.5 | 11.1 | 12.2 |
| U | 6.95 | 6.82 | 4.00 | 4.04 | 4.78 | 4.28 | 3.94 | 3.77 |
| Eu/Eu* | 1.01 | 1.26 | 0.90 | 0.90 | 0.94 | 0.92 | 0.90 | 0.84 |
| Sr/Y | 101.18 | 30.47 | 91.62 | 81.79 | 110.32 | 93.82 | 84.86 | 54.18 |
| La/Yb | 25.39 | 33.91 | 23.34 | 26.66 | 24.97 | 23.31 | 23.97 | 19.53 |
| $(La/Yb)_N$ | 18.21 | 24.32 | 16.74 | 19.12 | 17.91 | 16.72 | 17.20 | 14.01 |
| Dy/Yb | 2.24 | 2.68 | 2.09 | 2.34 | 2.26 | 2.16 | 2.18 | 1.99 |
| $^{87}Sr/^{86}Sr$ | 0.706419 | – | – | – | – | 0.706065 | – | 0.706627 |
| $^{87}Sr/^{86}Sr_{(i)}$ | 0.706090 | – | – | – | – | 0.705928 | – | 0.706419 |
| $^{143}Nd/^{144}Nd$ | 0.512569 | – | – | – | – | 0.512565 | – | 0.512456 |
| $^{143}Nd/^{144}Nd_{(i)}$ | 0.512541 | – | – | – | – | 0.512538 | – | 0.512429 |
| $\varepsilon Nd_{(t)}$ | −1.0 | – | – | – | – | −1.1 | – | −3.2 |
| $T_{DM}$ (Ma) | 957 | – | – | – | – | 912 | – | 1119 |
| $^{206}Pb/^{204}Pb$ | – | – | – | – | – | 18.687 | – | 18.676 |
| $^{207}Pb/^{204}Pb$ | – | – | – | – | – | 15.626 | – | 15.631 |
| $^{208}Pb/^{204}Pb$ | – | – | – | – | – | 38.747 | – | 38.773 |

(*continued on next page*)

**Table 1** (*continued*)

| No. | 41 | 42 | 43 | 44 | 45 |
|---|---|---|---|---|---|
| Sample | LJ1512 | XQBT02-J | XQBT09-J | XQBT10-J | HQBT14 |
| Locality | Jianchuan | Jianchuan | Jianchuan | Jianchuan | Liuhe |
| Latitude | 26°45′38.6” | 26°45′42.1” | 26°45′38.6” | 26°45′38.6” | 26°26′40.6” |
| Longitude | 99°41′42.4” | 99°41′55.9” | 99°41′42.4” | 99°41′42.4” | 100°19′41.5” |
| Lithology | MGP | MGP | MGP | MGP | AX |
| $SiO_2$ | 68.19 | 67.04 | 68.99 | 68.03 | 46.43 |
| $TiO_2$ | 0.35 | 0.34 | 0.35 | 0.33 | 1.77 |
| $Al_2O_3$ | 15.31 | 14.93 | 14.73 | 15.39 | 14.35 |
| $Fe_2O_3$ | 2.41 | 2.43 | 2.47 | 2.29 | 14.98 |
| MnO | 0.05 | 0.04 | 0.04 | 0.04 | 0.23 |
| MgO | 0.91 | 0.85 | 0.73 | 0.80 | 5.97 |
| CaO | 2.24 | 2.15 | 2.07 | 2.06 | 8.87 |
| $Na_2O$ | 4.74 | 4.75 | 4.71 | 4.98 | 3.45 |
| $K_2O$ | 4.02 | 4.26 | 3.81 | 4.14 | 1.17 |
| $P_2O_5$ | 0.17 | 0.18 | 0.16 | 0.18 | 0.2 |
| LOI | 1.11 | 3.19 | 1.00 | 1.15 | 2.06 |
| Total | 99.50 | 100.16 | 99.04 | 99.39 | 99.48 |
| Mg# | 0.43 | 0.41 | 0.37 | 0.41 | 0.44 |
| $K_2O/Na_2O$ | 0.85 | 0.90 | 0.81 | 0.83 | 0.34 |
| A/CNK | 0.94 | 0.91 | 0.94 | 0.94 | 0.62 |
| Li | 24.0 | 13.0 | 21.1 | 21.2 | 37.9 |
| Be | 4.35 | 3.68 | 3.93 | 3.96 | 3.52 |
| Sc | 4.61 | 4.59 | 4.59 | 4.56 | 52.5 |
| V | 32.1 | 38.7 | 38.4 | 37.3 | 311 |
| Cr | 6.90 | 7.95 | 6.50 | 6.80 | 102 |
| Co | 7.57 | 4.28 | 4.07 | 4.23 | 54.2 |
| Ni | 4.05 | 4.73 | 4.74 | 4.71 | 73.0 |
| Cu | 8.36 | 3.47 | 7.26 | 8.08 | 93.1 |
| Zn | 51.3 | 52.1 | 42.6 | 43.0 | 126 |
| Ga | 20.9 | 20.4 | 20.6 | 20.9 | 21.6 |
| Rb | 134 | 132 | 125 | 127 | 36.7 |
| Sr | 1387 | 803 | 1340 | 1440 | 461 |
| Y | 13.8 | 13.5 | 13.0 | 13.2 | 32.7 |
| Zr | 145 | 145 | 144 | 152 | 88.4 |
| Nb | 8.15 | 8.14 | 8.03 | 8.02 | 5.74 |
| Sn | 1.41 | 1.42 | 1.44 | 1.39 | 1.26 |
| Cs | 5.18 | 5.66 | 4.76 | 4.50 | 3.55 |
| Ba | 1814 | 1575 | 1459 | 1703 | 398 |
| La | 26.4 | 25.2 | 25.5 | 25.3 | 9.54 |
| Ce | 51.2 | 48.9 | 49.1 | 49.0 | 18.0 |
| Pr | 5.96 | 5.78 | 5.77 | 5.73 | 2.34 |
| Nd | 22.6 | 21.7 | 21.0 | 21.5 | 12.2 |
| Sm | 4.35 | 4.20 | 4.28 | 4.23 | 3.82 |
| Eu | 1.15 | 0.91 | 0.92 | 0.88 | 1.33 |
| Gd | 3.34 | 3.36 | 3.23 | 3.35 | 5.02 |
| Tb | 0.44 | 0.47 | 0.45 | 0.47 | 0.89 |
| Dy | 2.37 | 2.40 | 2.41 | 2.26 | 5.69 |
| Ho | 0.44 | 0.42 | 0.42 | 0.43 | 1.17 |
| Er | 1.19 | 1.18 | 1.22 | 1.18 | 3.40 |
| Tm | 0.17 | 0.17 | 0.16 | 0.16 | 0.50 |
| Yb | 1.08 | 1.08 | 1.11 | 1.09 | 3.19 |
| Lu | 0.16 | 0.17 | 0.16 | 0.16 | 0.46 |
| Hf | 4.51 | 4.38 | 4.27 | 4.37 | 2.66 |
| Ta | 0.99 | 0.60 | 0.57 | 0.60 | 0.38 |
| Tl | 1.05 | 1.20 | 1.09 | 1.10 | 0.25 |
| Pb | 50.1 | 50.1 | 57.9 | 48.9 | 18.3 |
| Th | 10.7 | 11.1 | 10.5 | 10.5 | 0.82 |
| U | 3.40 | 3.66 | 3.46 | 3.28 | 0.51 |
| Eu/Eu* | 0.92 | 0.74 | 0.76 | 0.71 | 0.93 |
| Sr/Y | 100.72 | 59.59 | 103.18 | 108.69 | 14.07 |
| La/Yb | 24.40 | 23.37 | 22.96 | 23.19 | 2.99 |
| $(La/Yb)_N$ | 17.50 | 16.76 | 16.47 | 16.64 | 2.15 |
| Dy/Yb | 2.19 | 2.22 | 2.17 | 2.07 | 1.78 |
| $^{87}Sr/^{86}Sr$ | – | – | – | – | – |
| $^{87}Sr/^{86}Sr_{(i)}$ | – | – | – | – | – |
| $^{143}Nd/^{144}Nd$ | – | – | – | – | – |
| $^{143}Nd/^{144}Nd_{(i)}$ | – | – | – | – | – |
| $\varepsilon Nd_{(t)}$ | – | – | – | – | – |
| $T_{DM}$ (Ma) | – | – | – | – | – |
| $^{206}Pb/^{204}Pb$ | – | – | – | – | – |
| $^{207}Pb/^{204}Pb$ | – | – | – | – | – |
| $^{208}Pb/^{204}Pb$ | – | – | – | – | – |

GP, granite porphyry; SP, syenite porphyry; MGP, monzogranite porphyry; AX, amphibolite xenolith.
All initial isotopic ratios are corrected to t = 35 Ma.

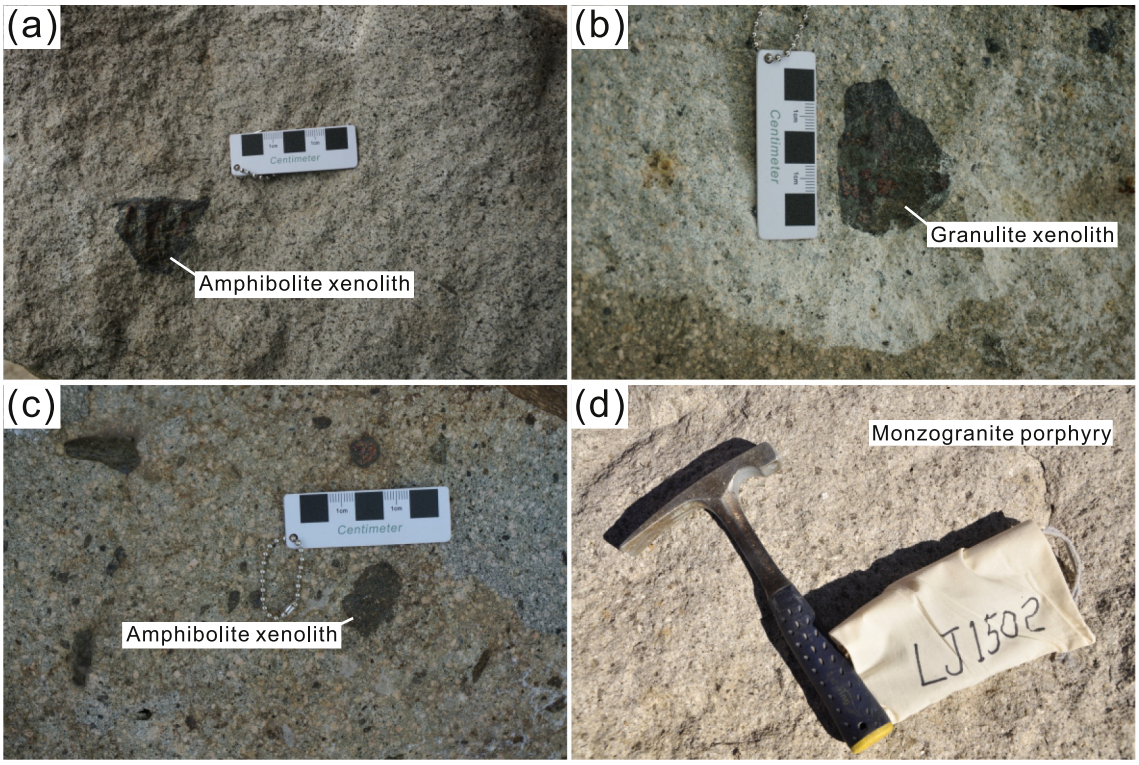


**Fig. 3.** Field closeup photos of the potassic felsic intrusions. (a) Jianchuan syenite porphyry with amphibolite xenolith; Liuhe syenite porphyry with (b) granulite and (c) amphibolite xenoliths; (d) Jianchuan monzogranite porphyry.

coronas are common around garnet crystals (Fig. 4c, d). The mineral assemblage at the peak metamorphic conditions is Gt + Cpx + Pl + Qtz, indicating high-pressure granulite facies (O'Brien and Rötzler, 2003). Garnet-bearing pyroxene granulites have porphyroblastic texture. The main minerals are garnet, clinopyroxene, orthopyroxene, biotite, amphibole and plagioclase (Fig. 4e, f). Concentric coronas of opaque minerals and biotite are developed around garnet crystals (Fig. 4f). Beyond the coronas, a biotite-free zone about 500 μm wide is also developed surrounding garnet crystals. Two types of biotite could be distinguished. One is anhedral, evenly distributed in the matrix (Fig. 4e), the other appears as a corona phase around garnet xenocrysts with yellow-lime pleochroism (Fig. 4f).

Monzogranite porphyries were collected from Jianchuan, consisting of subhedral to anhedral phenocrysts of K-feldspar, plagioclase, quartz, amphibole and biotite. The matrix consists of felsic minerals and accessory apatite, zircon, iron oxides etc. (Fig. 3d, Fig. 4g). Some of the K-feldspar are veavily altered.

Granite porphyries were collected from Machangqing. These rocks are pale and grayish white and contain K-feldspar megacrysts (Fig. 4h). The main minerals in the granites are K-feldspar, plagioclase, quartz and minor amounts of subhedral biotite and amphibole (Fig. 4h).

## 4. Analytical methods

### 4.1. Electron probe microanalysis (EPMA) of minerals

Electron probe micro-analysis of minerals was carried out in the Institute of Geology and Geophysics, Chinese Academy of Sciences (IGGCAS), Beijing. A five-spectrometer Cameca SX-100 electron microprobe analyzer was used with an accelerating voltage of 15 kV and beam current of 30 nA. The precision of all analyzed elements was better than 1.5%.

### 4.2. Zircon U-Pb dating and Hf isotopes

Sample processing for zircon separation involved crushing, initial heavy liquid and subsequent magnetic separation. Representative zircon grains were hand-picked and mounted on adhesive tape, embedded in epoxy resin, polished to about half their size and photographed in reflected and transmitted light. Zircon structures were also studied using cathode luminescence (CL) imaging.

Zircon U-Pb dating for HQBT02 and HQBT11 was carried out in the Institute of Oceanology, Chinese Academy of Sciences, Qingdao, and in the State Key Laboratory of Geological Processes and Mineral Resources, China University of Geosciences, Beijing (GPMR-CUGB) for the other samples, using a laser ablation-inductively coupled plasma mass spectrometry (LA-ICPMS). The detailed operating conditions for the laser ablation system, the ICP-MS instrument, and data reduction followed those described in Liu et al. (2010). ICPMSDataCal (Liu et al., 2010) was used for data reduction and ISOPLOT (ver 3.0) (Ludwig, 2003) was used for age calculation for plotting the concordia diagrams.

Zircon in situ Hf isotope analysis was conducted using a Thermo-Finnigan Neptune MC-ICPMS equipped with a 193 nm Excimer ArF laser-ablation system (GeoLas Plus) in IGGCAS. Lu-Hf isotopic data were acquired with a spot size of 60 μm. Zircon standards, Mud Tank and GJ-1, were analyzed as quality control standards. The average $^{176}Hf/^{177}Hf$ ratios for the Mud Tank and GJ-1 were 0.282504 ± 0.000033 (2SD, n = 32) and 0.282017 ± 0.000044 (2SD, n = 30), respectively, which agree well with recommended values (Woodhead and Hergt, 2005).

### 4.3. Whole-rock major and trace elements

For samples JC1702, JC1702 and JC1703, the whole-rock major element oxides were analyzed in the Wuhan SampleSolution Analytical Technology Co., Ltd., Wuhan, by using X-ray fluorescence (XRF) with a ZSX Primus II spectrometer. For the other samples, the whole-rock major element oxides were analyzed using a Leeman Prodigy inductively coupled plasma-optical emission spectrometer (ICP-OES) at China University of Geosciences, Beijing (CUGB). Precisions (1σ) for most elements based on rock standards GSR-1, GSR-3 (National Geological Standard Reference Materials of China) and AGV-2 (US Geological

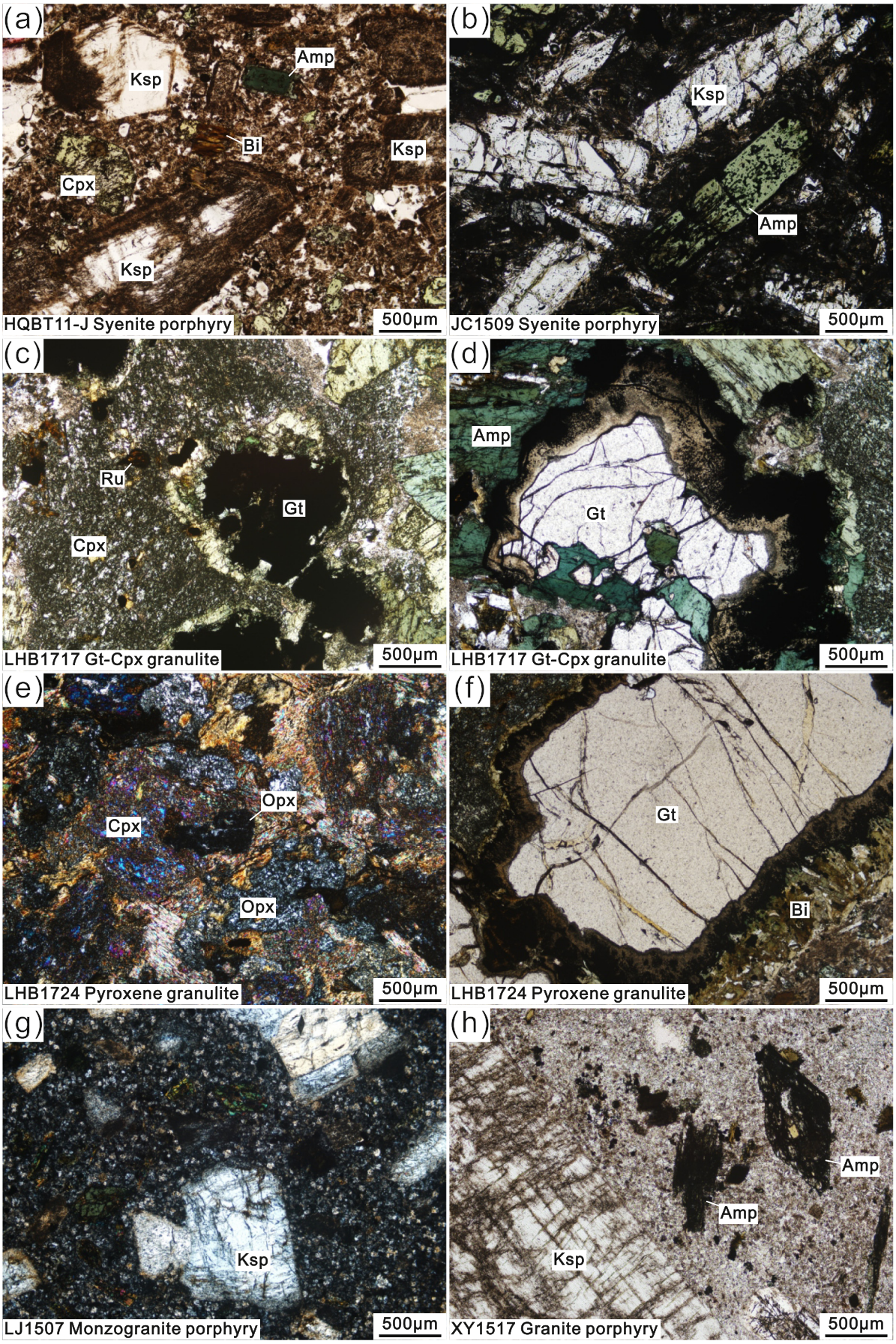


**Fig. 4.** Photomicrographs showing typical textures of the potassic felsic intrusions and xenoliths. K-feldspar and amphibole phenocrysts from syenite porphyries are euhedral to subhedral (a), some of which show argillic alteration (b). (c) Xenoliths of garnet-clinopyroxene granulite show homeoblastic texture with concentric opaque and amphibole coronas being common around garnet crystals (d). (e) Garnet-bearing pyroxene granulite has porphyroblastic texture with concentric coronas of opaque minerals and biotites developed around garnet (f). (g) Phenocrysts of K-feldspar, plagioclase, quartz, amphibole, and biotite from the Jianchuan monzogranite porphyries are subhedral to anhedral. (h) K-feldspar megacrysts from Machangqing granite porphyries.

Survey) are better than 1.0% except for $TiO_2$ (<1.5%) and $P_2O_5$ (1.0–1.5%). Loss on ignition (LOI) was determined by placing 500 mg of samples in a muffle furnace at 1000 °C for several hours before cooled in a desiccator and reweighed.

Whole-rock trace elements concentrations were determined using an Agilent 7700e ICP-MS in the Wuhan SampleSolution Analytical Technology Co., Ltd. The rock powder (~50 mg) was dissolved in a Teflon bomb using a mixture HF and $HNO_3$. The Teflon bomb was put in a stainless-steel pressure jacket and heated to 190 °C in an oven for >24 h. After cooling, the Teflon bomb was opened and placed on a hotplate at 140 °C and evaporated to dryness. The dried sample was refluxed with 1 ml of $HNO_3$. The final solution was diluted to ~100 g with 2% $HNO_3$ in a polyethylene bottle. Detailed operating conditions of the ICP-MS instrument and data reduction have been described by Liu et al. (2008).

### 4.4. Whole-rock Sr-Nd-Pb isotopes

Rock powders were dissolved using a mixture of concentrated HF and $HNO_3$ in Teflon-lined bombs (at GPMR-CUGB) or in Teflon beakers (in Isotope Geochemistry and Geochronology Research Centre, Carleton University (IGGRC-CU)), followed by 8 M $HNO_3$ and 6 M HCl. Pb, Sr and Nd were separated following the ion exchange column procedures described in Cousens (1996). Pb isotopes for all the samples, and Sr and Nd isotopes for samples HQBT11-J, HQBT14-J, JC1506, JC1702 and XY1504, were measured using a Thermo-Finnigan Neptune MC-ICP-MS at IGGRC-CU, while the Sr and Nd isotopic ratios for the other samples, were measured in GPMR-CUGB using a Thermo-Finnigan Triton thermal ionization mass spectrometer. Sr and Nd isotopic ratios were normalized against $^{86}Sr/^{88}Sr = 0.1194$ and $^{146}Nd/^{144}Nd = 0.7219$, respectively. In IGGRC-CU, thallium was used as an internal standard to correct for instrumental drift on Pb isotopes; the measured $^{143}Nd/^{144}Nd$ ratios for the samples were corrected for the offsets of the measured JNdi values against a reference value of 0.512115 (Tanaka et al., 2000). Pb isotope ratios were corrected for the offsets of measured NBS981 values against the reference values of Todt et al. (1996).

In IGGRC-CU, measurements of USGS rock standard BCR-2 and NBS987 yield average $^{87}Sr/^{86}Sr$ ratios of 0.705019 (n = 3) and 0.710258 ± 0.000025 (2SD, n = 13), respectively, while the average $^{143}Nd/^{144}Nd$ ratios of BCR-2 and international standard JNdi-1 are 0.512640 ± 0.000008 (n = 1) and 0.512088 ± 0.000013 (2SD, n = 18), respectively. NBS981 bracketing the samples, yields average ratios of $^{206}Pb/^{204}Pb = 16.9317 \pm 0.0012$ (2SD, n = 16), $^{207}Pb/^{204}Pb = 15.4853 \pm 0.11$ (2SD, n = 16), and $^{208}Pb/^{204}Pb = 36.6784 \pm 0.0035$ (2SD, n = 16). Analysis of BCR-2 yields $^{206}Pb/^{204}Pb = 18.7579$, $^{207}Pb/^{204}Pb = 15.6173$, and $^{208}Pb/^{204}Pb = 38.7226$. The total procedure blanks in IGGRC-CU are <100, <250 and < 50 pg for Pb, Sr and Nd respectively. In GPMR-CUGB, USGS rock standard BHVO-2 and NBS987 yield average $^{87}Sr/^{86}Sr$ ratios of 0.703488 ± 0.000002 (n = 2) and 0.710274 ± 0.000011 (2SD, n = 61), respectively. The average

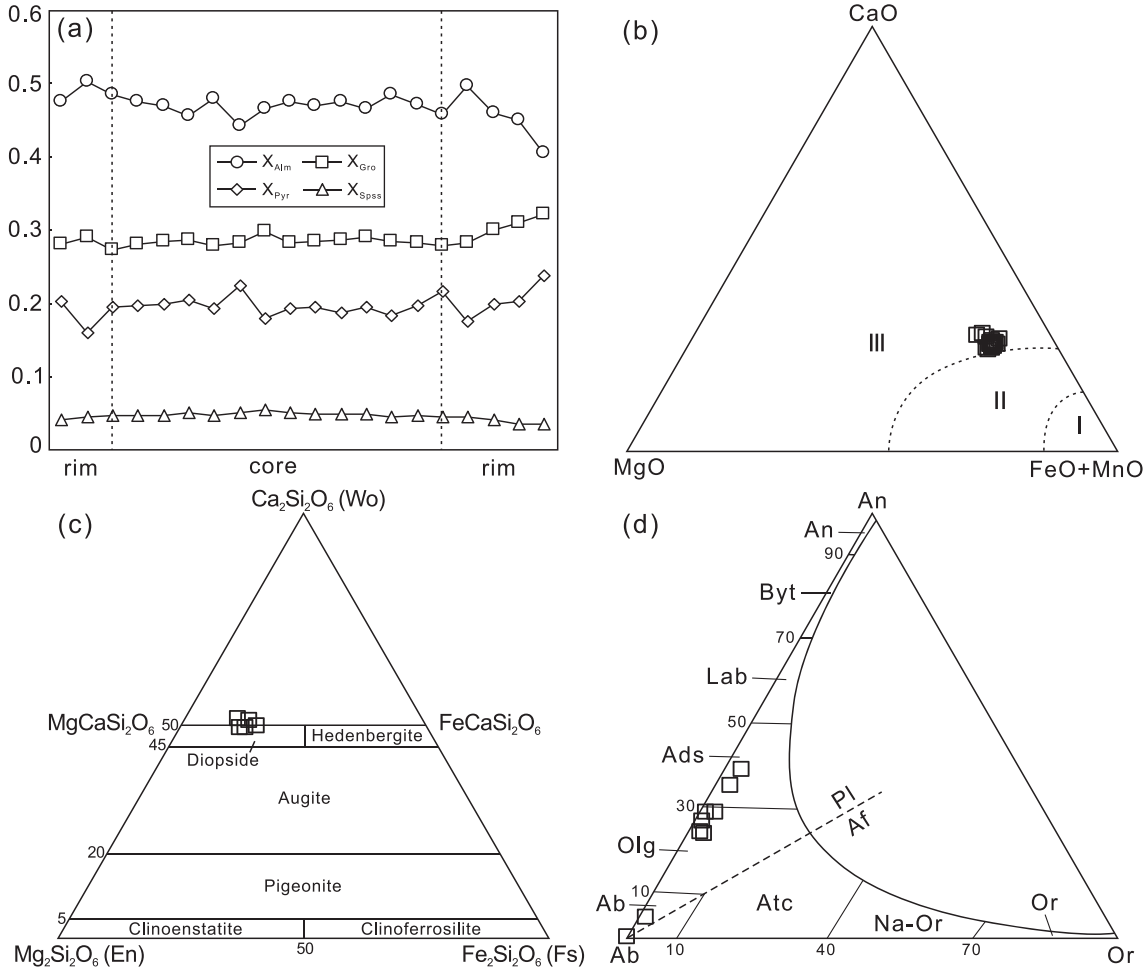


**Fig. 5.** (a) Compositional variations of garnet from sample LHB1717; (b) Triangular diagram of garnet showing metamorphic conditions of the host rock (Jin and Li, 1986, I, Amphibolite facies; II, Granulite facies; III, Eclogite facies); (c) Pyroxene classification diagram (Morimoto, 1988); (d) Feldspar classification diagram (Smith, 1974).

$^{143}Nd/^{144}Nd$ of BHVO-2 and Alfa Nd standard are 0.512957 ± 0.000010 (n = 2) and 0.512423 ± 0.000024 (2SD, n = 58), respectively.

## 5. Results

### 5.1. Mineral chemistry

To evaluate physical conditions of the magmatism, EPMA is used to study the mineral chemistry of garnet-clinopyroxene granulite minerals (LHB1717, Supplementary Table S1, Fig. 4c,d) entrained in the Liuhe syenite porphyry, which is assumed to represent the melting residue for the potassic magmas. Only mineral assemblage of Gt + Cpx + Pl + Qtz at the peak conditions is considered in this study. The content of $Fe^{3+}$ in garnet and clinopyroxene is calculated following Droop (1987).

Garnet could exist in various metamorphic rocks with different chemical types over a wide range of temperature and pressure. Compositions of garnet are often used to assess their thermal processes. Garnet crystals from the garnet-clinopyroxene granulite are almandine (Alm) -pyrope (Pyr) -grossular (Gro) -spessartine (Spss) solid solutions with the composition in the range $Alm_{38-50}Pyr_{16-22}Gro_{15-29}Spss_{3-5}$. The compositional variations of the garnet in sample LHB1717 include a homogeneous core domain, with a sharp increase in $X_{pyr}$, $X_{gro}$, and decrease in $X_{alm}$ towards rims (Fig. 5a). This zoning pattern suggests high temperature and continuous intra-crystalline diffusion forming the homogeneous core domain. Subsequently, intergranular diffusion occurred at the edge of the garnet crystals.

Clinopyroxenes in the granulite are diopsides with near-constant compositional ranges of 50–52 mol% Wo, 35–38 mol% En and 11–15 mol% Fs (Fig. 5c). It contains 1.5–5.9 wt% $Al_2O_3$ and $X_{Mg}$ (=Mg/[$Fe^{2+}$+Mg]) ranges from 0.70 to 0.79.

The plagioclase from the garnet-clinopyroxene granulite is mainly oligoclase to andesine with compositions of $An_{25-40}$ (Fig. 5d). Albite ($An_{0-5}$) is also present in late plagioclase (Fig. 5d).

### 5.2. Zircon U-Pb ages and Hf isotopes

Zircons from Liuhe syenite porphyries are euhedral to subhedral with magmatic oscillatory zoning in CL images (cf. Hoskin and Schaltegger, 2003), some of which exhibit weak zoning and growth rings. Crystal lengths are 80–150 μm with length-to-width ratios of 2:1 to 3:1 (Fig. 6a, b, c) and up to 6:1. Inherited cores and rounded xenocrystic zircons are common. The Th/U ratios range from 0.10 to 2.08, except for a few with extreme values. Zircons separated from the Jianchuan syenite porphyries are subhedral to anhedral, exhibiting subangular shape (Fig. 6d). Rounded xenocrystic zircons are also observed, with rare inherited cores. In contrast to zircons from Liuhe syenite porphyries, those from Jianchuan have relatively low Th (68–179 ppm) and U (111–226 ppm), with Th/U ratios of 0.47–0.95. Most of the zircons from granite and monzogranite porphyries are euhedral to subhedral with narrow and frequent oscillatory zoning, ranging from 60 to 150 μm in size with length-to-width ratios of 1:1 to 3:1 (Fig. 6e–o). Zircons from monzogranite porphyries exhibit variable concentrations of Th (87–2728 ppm) and U (369–2377 ppm) with Th/U ratio of 0.10 to 2.00. However, zircons from Machangqing show

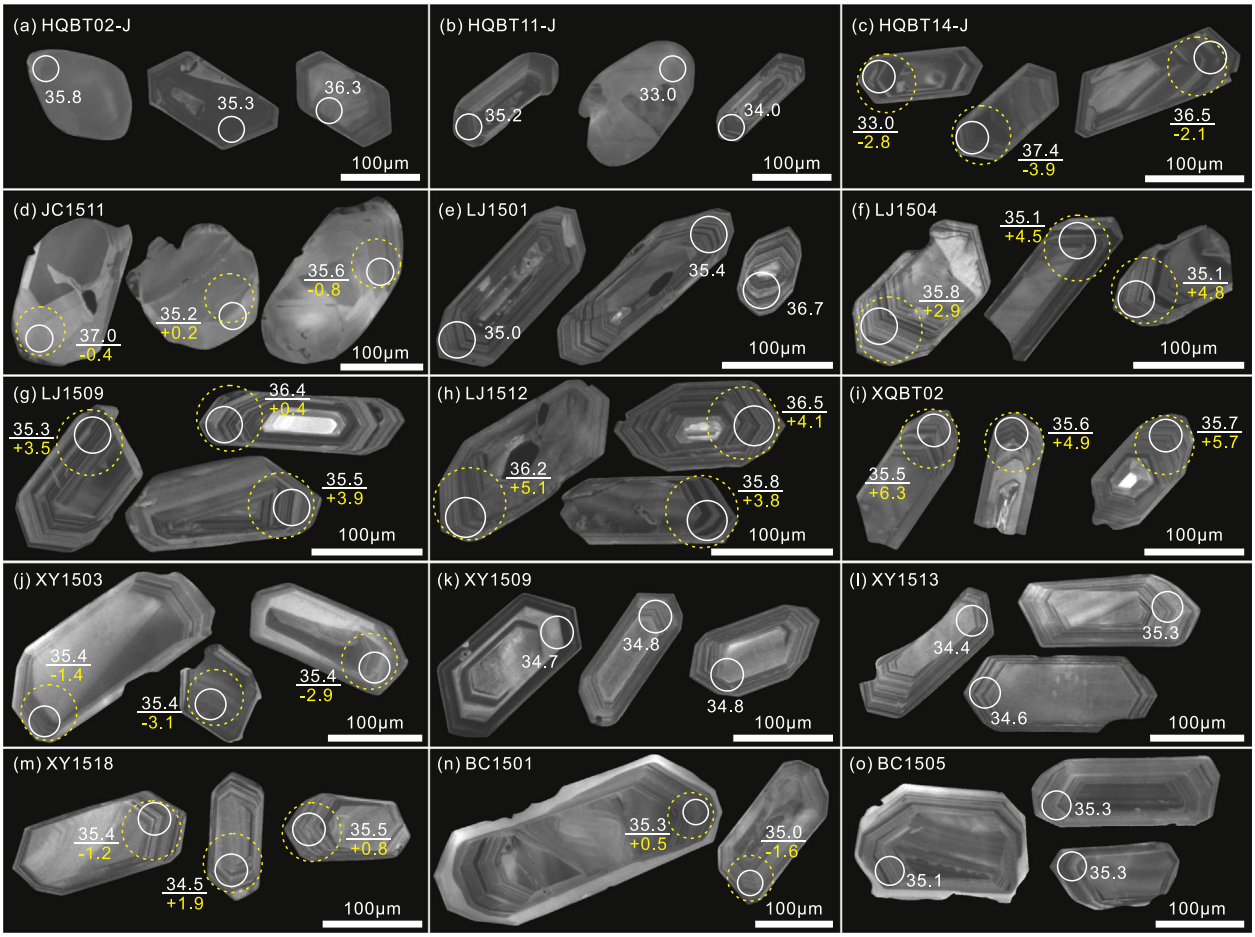


**Fig. 6.** Cathodoluminescence (CL) images of representative analyzed zircons from the potassic felsic rocks in western Yunnan. White and yellow dashed circles indicate the spots for LA-ICP-MS U-Pb age dating and Hf isotope analysis, respectively. Values of zircon U-Pb ages and $\varepsilon_{Hf}(t)$ are given. (For interpretation of the references to colour in this figure legend, the reader is referred to the web version of this article.)

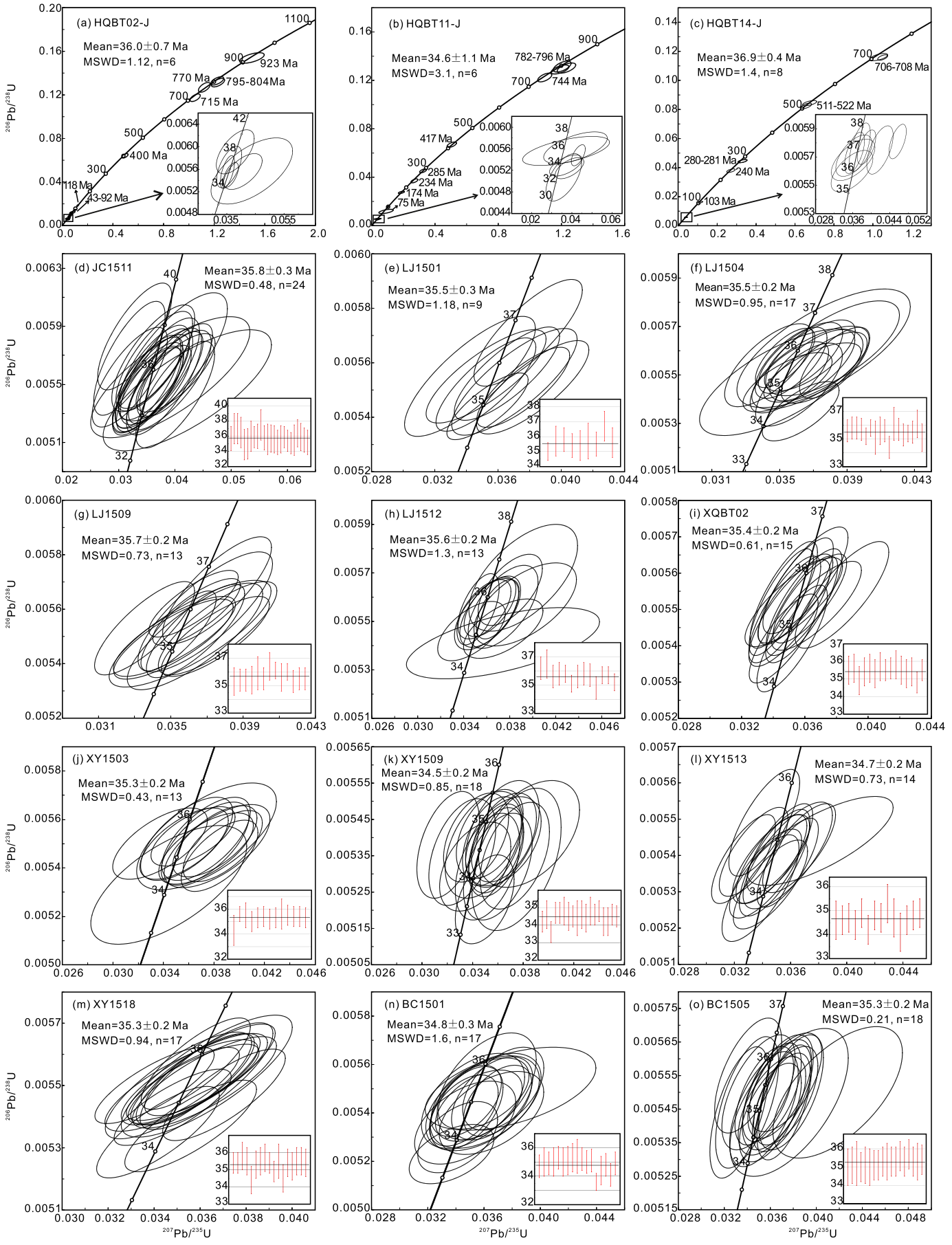


**Fig. 7.** U-Pb concordia for zircons in the potassic felsic rocks in western Yunnan.

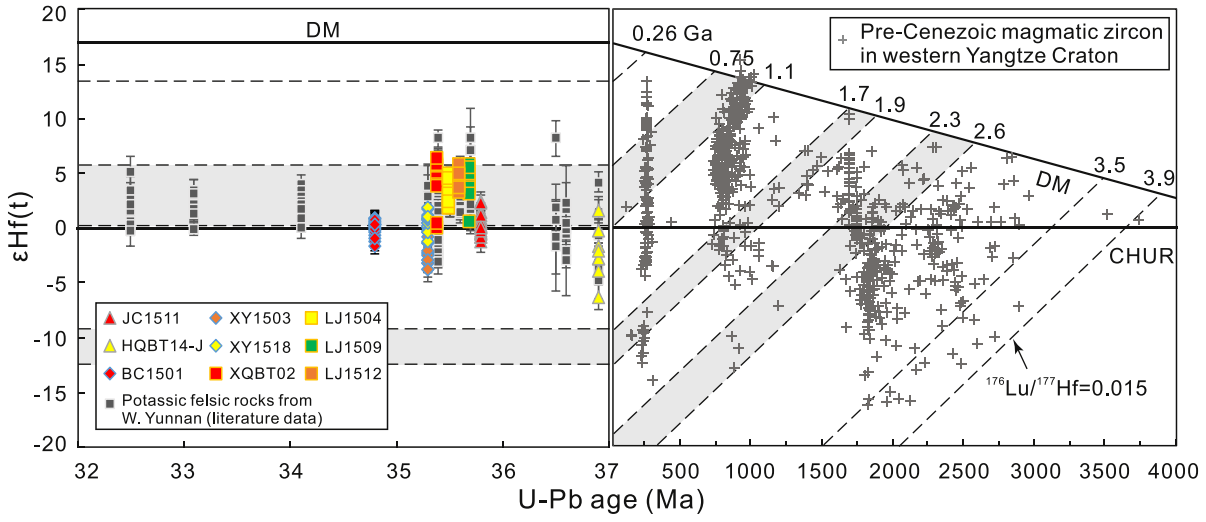


**Fig. 8.** Zircon $\varepsilon_{Hf}(t)$ vs. U-Pb ages (modified from Lu et al., 2013). Literature data are from Lu et al. (2012). Data of Pre-Cenozoic magmatic zircons are from Lu et al. (2013) and references therein. The grey fields represent episodes of major juvenile crustal growth in the Yangtze Craton. DM, Depleted Mantle; CHUR, Chondritic Uniform Reservior.

relatively high Th (246–2472 ppm) and U (189–1861 ppm) with Th/U ratio of 0.40–1.96.

Analyzed zircons from 15 samples cover a range of U-Pb ages from 35 Ma to 37 Ma (Supplementary Table S2). Zircons separated from Liuhe syenite porphyry sample HQBT14-J yield an oldest weighted mean $^{206}Pb/^{238}U$ age of 36.9 ± 0.4 Ma (Fig. 7c). Another two samples of Liuhe syenite porphyries yield weighted mean zircon U-Pb ages of 36.0 ± 0.7 Ma and 34.6 ± 1.1 Ma, respectively (Fig. 7a, b). Zircons from Jianchuan syenite porphyry sample JC1511 yield a zircon U-Pb age of 35.8 ± 0.3 Ma (Fig. 7d). Five Jianchuan monzogranite porphyries samples yield U-Pb ages of 35.5 ± 0.3 Ma, 35.5 ± 0.2 Ma, 35.7 ± 0.2 Ma, 35.6 ± 0.2 Ma, and 35.4 ± 0.2 Ma, respectively (Fig. 7e–i). Six granite porphyries samples from the Machangqing area yield zircon U-Pb ages of 35.3 ± 0.2 Ma, 34.5 ± 0.2 Ma, 34.7 ± 0.2 Ma, 35.3 ± 0.2 Ma, 34.8 ± 0.3 Ma, and 35.3 ± 0.2 Ma, respectively (Fig. 7j–o). Samples in the south are slightly younger than that in the north (Fig. 2).

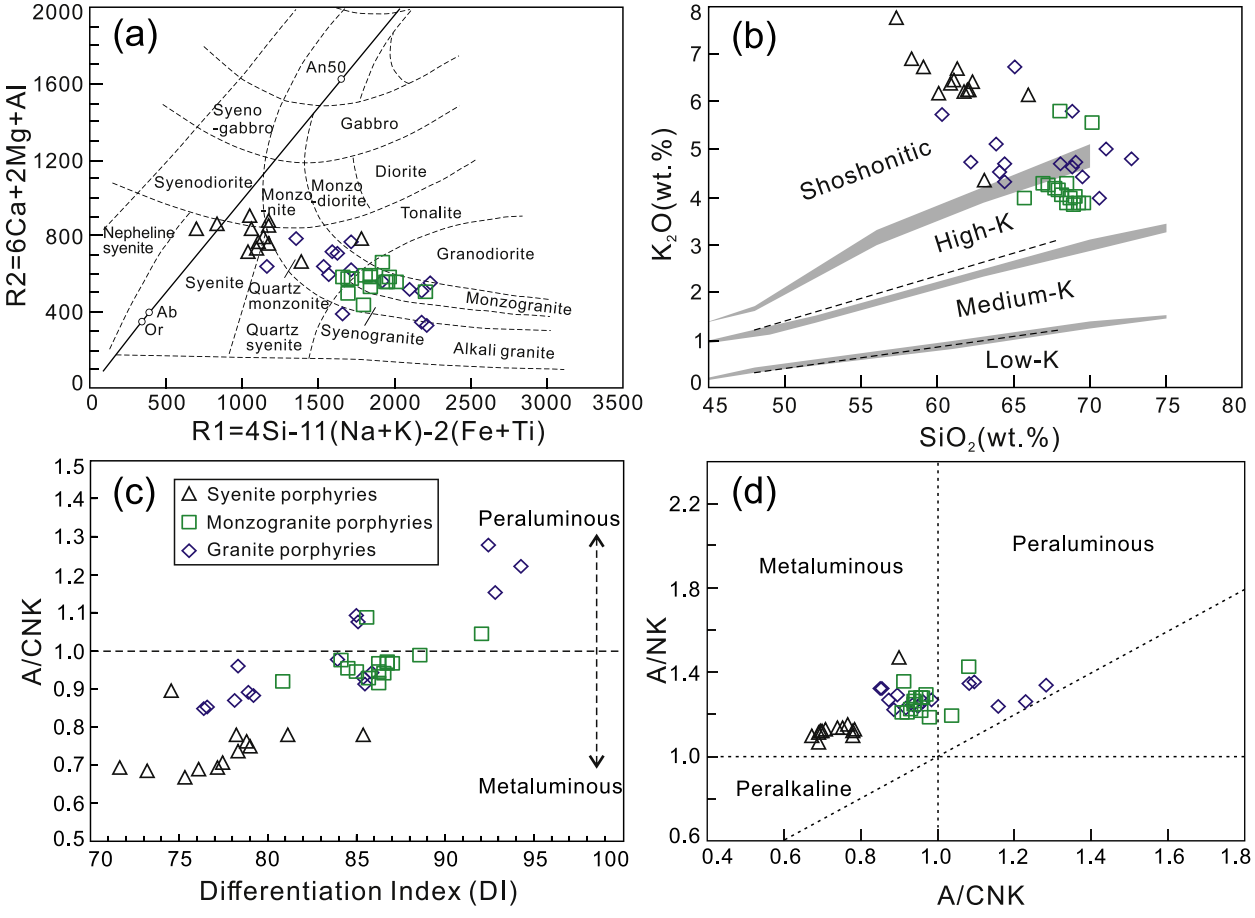


**Fig. 9.** (a) R2 vs. R1 diagram for rock classification (De la Roche et al., 1980); (b) K2O vs. SiO2 diagram (Rickwood, 1989); (c) A/CNK vs. differentiation index (DI); (d) A/NK vs. A/CNK.

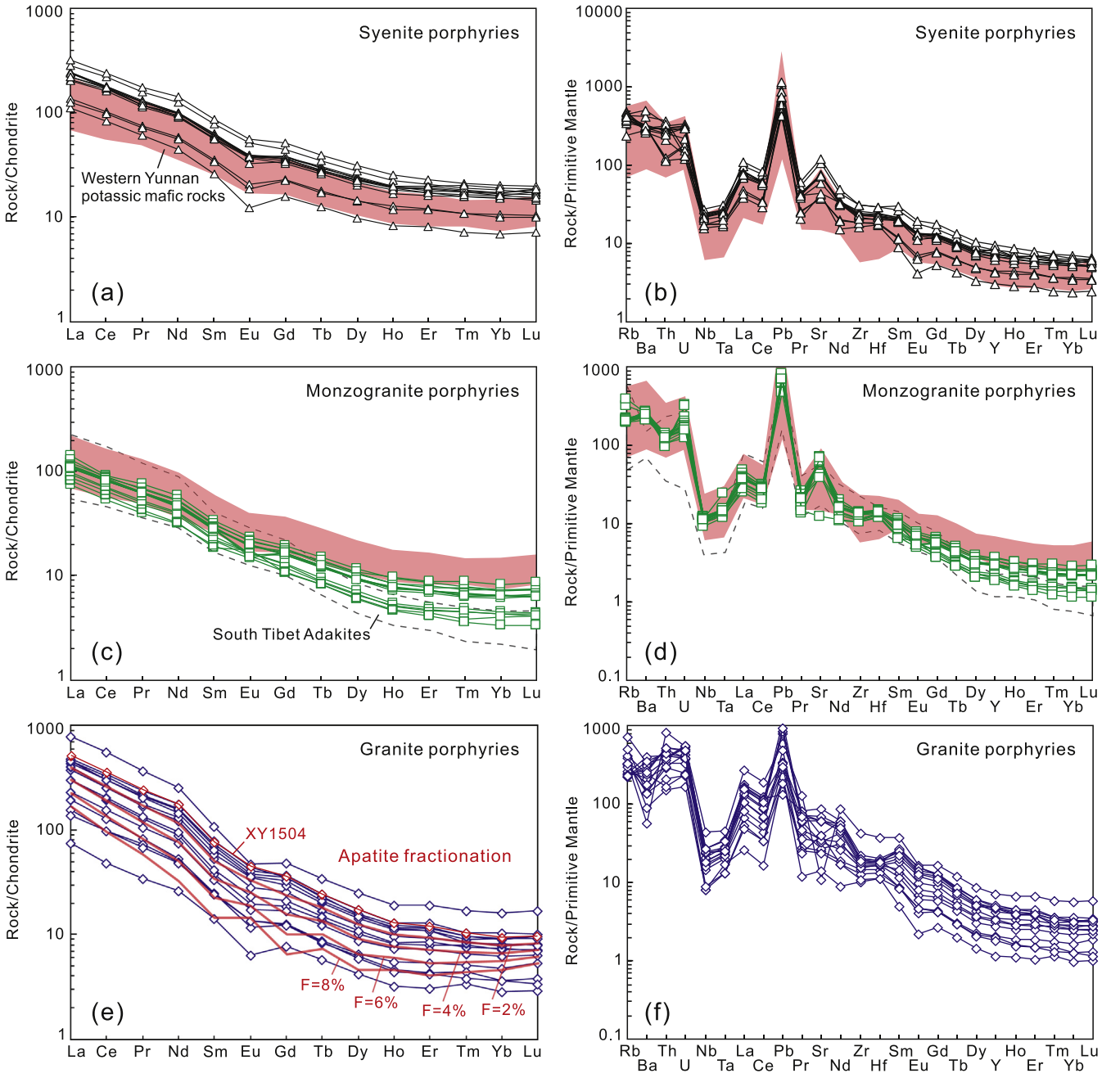


**Fig. 10.** Chondrite-normalized rare earth element (REE) and primitive-mantle-normalized trace element patterns of the potassic felsic intrusions in western Yunnan. Data for coeval potassic mafic rocks from western Yunnan are from the literature (Huang et al., 2010; Li et al., 2002; Xu et al., 2001). Fields with dashed outline represent the compositions of South Tibet adakites derived from thickened lower crust (Chung et al., 2003). Red lines in Fig. 10e represent modeled REE patterns of granite porphyries from western Yunnan, with varying degrees of fractional crystallization from the assumed parent magma composition (XY1504). Partition coefficients used are from Wang et al. (2015) and references therein. Normalization data are from Sun and McDonough (1989). (For interpretation of the references to colour in this figure legend, the reader is referred to the web version of this article.)

In situ zircon Hf isotopic analysis was performed on nine samples (Supplementary Table S3, Fig. 8). Three Machangqing granite porphyries samples show concentrated $\varepsilon_{Hf}(t)$ values with individual analyses range from −3.8 to −0.8 (XY1503), −1.2 to +1.9 (XY1518) and − 1.6 to +0.9 (BC1501), respectively, whose variation range smaller than four units, with crustal model ages (TC DM) of 1.2 to 1.4 Ga, 1.0 to 1.2 Ga and 1.1 to 1.2 Ga. For syenite porphyries, varying zircon $\varepsilon_{Hf}(t)$ values (−6.3 to +1.6) can be observed in the sample from Liuhe (HQBT14-J), but concentrated (−1.2 to +2.4) from Jianchuan (JC1511), with TC DM model ages of 0.8 to 1.5 Ga and 1.0 to 1.2 Ga, respectively. Four Jianchuan monzogranite porphyry samples (XQBT02, LJ1504, LJ1509, LJ1512) have relatively high zircon $\varepsilon_{Hf}(t)$ values. The average of that range from +3.3 to +4.0 with mean TC DM model ages of 0.9 Ga. Except for sample LJ1512, the other monzogranite porphyry samples show varying zircon $\varepsilon_{Hf}(t)$ values with variations greater than five epsilon units. These TC DM model ages support the understanding that the Neoproterozoic is the main period for crustal growth in the Yangtze craton (Fig. 8).

### 5.3. Bulk-rock geochemistry

In terms of bulk-rock major element compositions (Table 1), the samples in this study can be classified as syenite, quartz monzonite, monzogranite, monzogranite, and syenogranite (Fig. 9a).

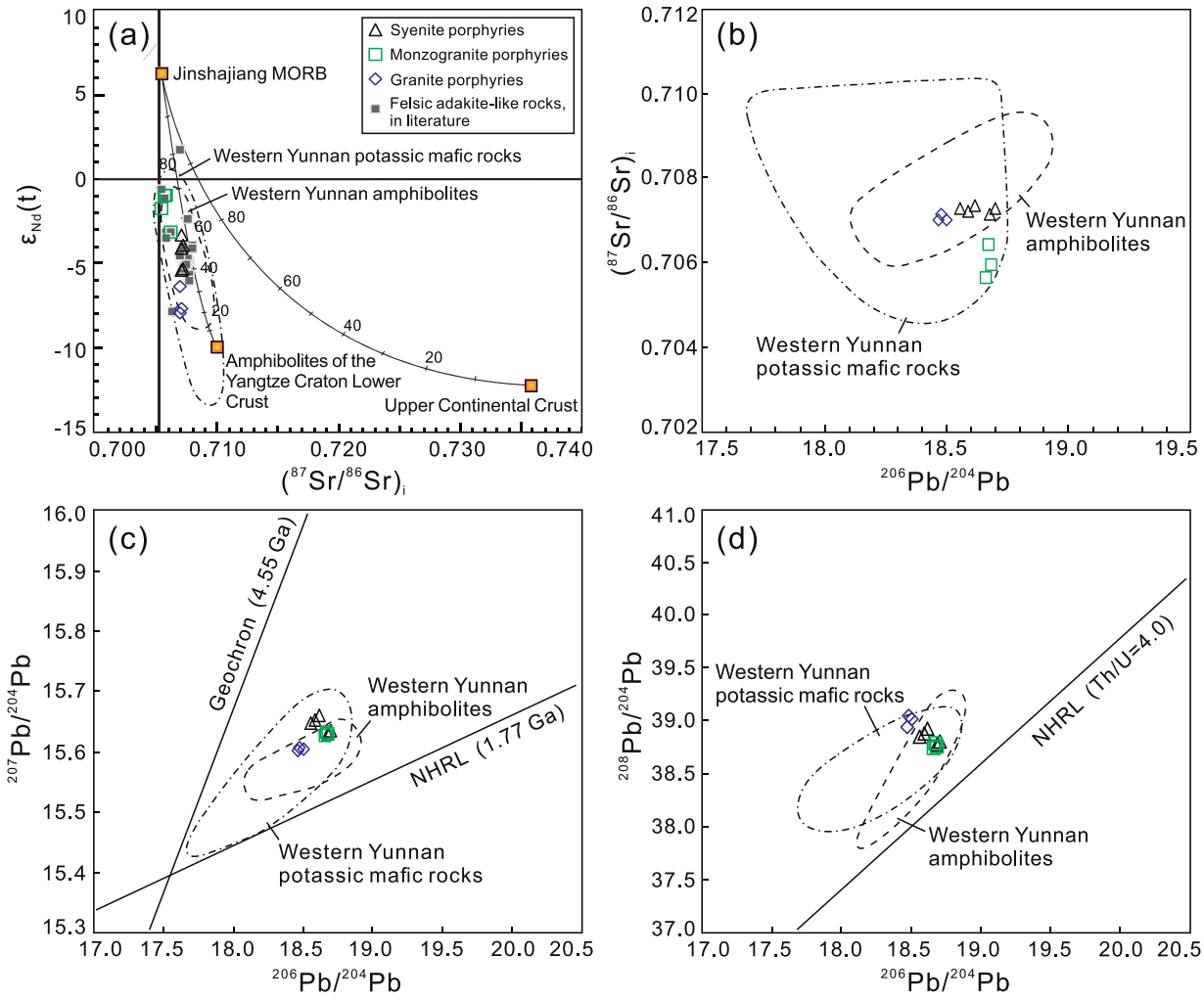


**Fig. 11.** (a) $(^{87}Sr/^{86}Sr)_i$ vs. $\varepsilon_{Nd}(t)$; (b) $^{206}Pb/^{204}Pb$ vs. $(^{87}Sr/^{86}Sr)_i$; (c) $^{206}Pb/^{204}Pb$ vs. $^{207}Pb/^{204}Pb$; (d) $^{206}Pb/^{204}Pb$ vs. $^{208}Pb/^{204}Pb$. Estimated endmembers of the Jinshajiang MORB, upper continental crust (UCC) and amphibolites of the Yangtze Craton lower crust are from He et al. (2016) and references therein. Data for western Yunnan potassic mafic rocks are from the literature (Guo et al., 2005; Huang et al., 2010; Li et al., 2002; Xu et al., 2001), for the western Yunnan amphibolite are from Deng et al. (1998). Northern Hemisphere Reference Line (NHRL) is from Hart (1984). All initial isotopic ratios are corrected to $t = 35$ Ma (see Fig. 7).

Shoshonitic syenite porphyries from Liuhe and Jianchuan have high $K_2O$ (4.37–7.79 wt%, Fig. 9b) and $K_2O/Na_2O$ (1.22–2.96), the lowest A/NK (1.07–1.48, Fig. 9d), high Y (14.0–43.7 ppm) and Yb (1.16–3.44 ppm), steep light rare earth element (REE) enrichment ($[La/Sm]_N = 3.43–4.25$), nearly flat heavy REE ($[Gd/Yb]_N = 1.82–2.55$) patterns, and moderate negative Eu anomalies ($Eu/Eu^* = 0.60–0.87$) (Fig. 10a,b).

Monzogranite porphyries from Jianchuan have a high-K calc-alkaline affinity with $K_2O/Na_2O$ ratio of 0.80–0.98, except for two relatively high $K_2O$ samples (Fig. 9b). These samples have high A/NK (1.18–1.42), A/CNK (0.91–1.09) (Fig. 9c,d), Sr (256–1528 ppm), but low Y (8.41–16.7 ppm) and Yb (0.57–1.39 ppm) (Fig. 14), and have fractionated REE patterns ($[La/Yb]_N = 14.01–24.32$) with no or weak negative Eu anomalies ($Eu/Eu^* = 0.71–1.01$, except for one sample with $Eu/Eu^*$ of 1.26) (Fig. 10c,d).

Compared with syenite and monzogranite porphyries, granite porphyries from Machangqing have variable $SiO_2$ (60.24–75.86 wt%; Fig. 9b) and A/CNK (0.85–1.28, Fig. 9c,d), and have variably evolved compositions with varying DI (76–96; Fig. 9c), which is consistent with a positive DI-A/CNK correlation (Fig. 9c). These samples have varying ΣREE of 59–726 with moderate negative Eu anomalies ($Eu/Eu^* = 0.60–0.85$) (Fig. 10e, f).

The trace elements in all these samples share a similar signature. They are relatively enriched in large ion lithophile elements (LILE, e.g., Rb, Th, and U) and light REEs, and relatively depleted in high field strength elements (HFSEs, e.g., Nb, Ta, and Ti) and heavy REEs (Fig. 10).

All the samples show a narrow range of $^{87}Sr/^{86}Sr$ (0.705784–0.70852). Syenite porphyries show a small range of bulk-rock $\varepsilon_{Nd}$ (t) (−5.4 to −3.3) and a similar narrow Pb isotopic compositions ($^{206}Pb/^{204}Pb$ = 18.557–18.698, $^{207}Pb/^{204}Pb$ = 15.629–15.660, $^{208}Pb/^{204}Pb$ = 38.785–38.935) (Fig. 11). Granite porphyries have bulk-rock $\varepsilon_{Nd}(t)$ of −7.9 to −6.4 with a small range Pb isotope compositions (18.467–18.501, 15.604–15.607, 38.952–39.057) (Fig. 11). Compared with syenite and granite porphyries, monzogranite porphyries from Jianchuan show the highest bulk-rock $^{143}Nd/^{144}Nd$ (0.512456–0.512569) with $\varepsilon_{Nd}(t)$ of −3.2 to −1.0, and similar radiogenic Pb isotope compositions (18.666–18.687, 15.624–15.631, and 38.727–38.774, Fig. 11).

## 6. Discussion

### *6.1. Spatial and temporal distribution of the Eocene-Oligocene K-rich intrusions along the Jinsha suture*

The Eocene-Oligocene potassic-ultrapotassic rocks are well exposed in many localities along with, and in the vicinity of, the Jinsha suture across the Qiangtang block, the Simao-Indochina block, and the western

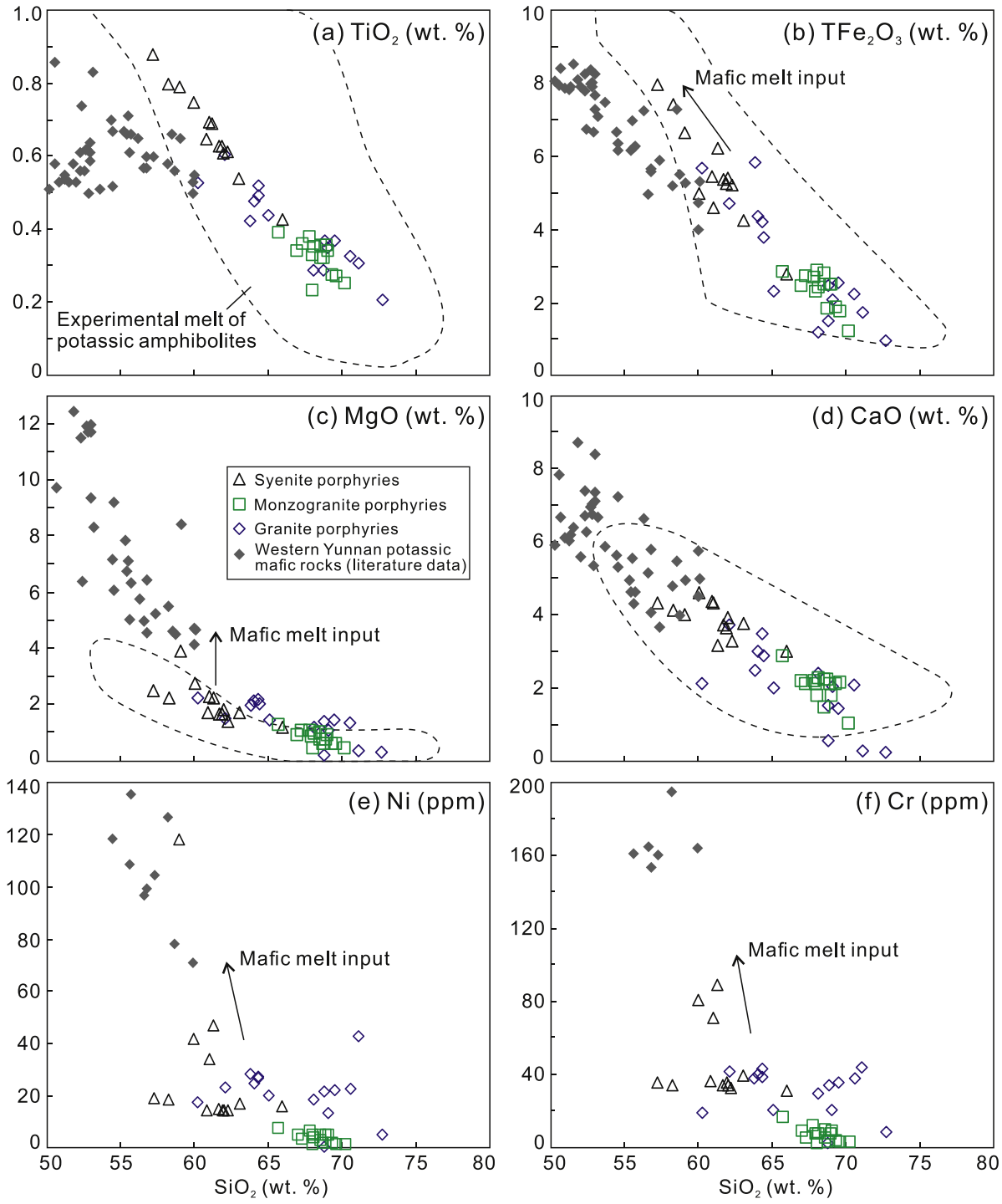


**Fig. 12.** $SiO_2$ variation diagrams with $TiO_2$ (a), $TFe_2O_3$ (b), MgO (c), CaO (d), Ni (e) and Cr (f), showing the major and compatible element compositions of the potassic felsic intrusions in western Yunnan. Data sources are as in Fig. 11. Dashed fields indicate experimental melt compositions derived from potassic amphibolites (Lu et al., 2013).

Yangtze Craton (Fig. 1b, Chung et al., 2005), extending over 2000 km along, forming a discontinuous potassic magmatic belt. It can be traced westward to Fenghuoshan in the west of the eastern Qiangtang block, and southeastward to the regions around the ASRR shear zone (Fig. 1b, Chung et al., 2005; Wang et al., 2001; Xu et al., 2001; Li et al., 2002). In the Sanjiang region, Deng et al. (2014) subdivided the alkaline intrusions into three segments: the north segment (intrusive rocks scattered around Yulung), the central segment (intrusions from Weixi to Dali), and the south segment (intrusions clustered to the southeast of Lüchun County. Along the ASRR shear zone, scattered potassic-ultrapotassic magmatic suites extend up to 50 km to the west within the Simao-Indochina block, and eastward into the Yangtze Craton for up to 150 km for the felsic intrusions and 270 km for the mafic rocks (Fig. 2, Guo et al., 2005).

The magmatic suites occurring in the eastern Qiangtang block are dated at ca. 45 Ma and 33 Ma, extending from Fenghuoshan to Mangkang, including Nangqian, Xialaxio and Yulung areas (Fig. 1b, Hou et al., 2003; Guo et al., 2006; Liang et al., 2007). Zircon U-Pb and biotite $^{40}Ar/^{39}Ar$ ages of ca. 49 Ma for a potassic monzonitic granite from the Xialaxio area are also reported (Roger et al., 2000). The potassic

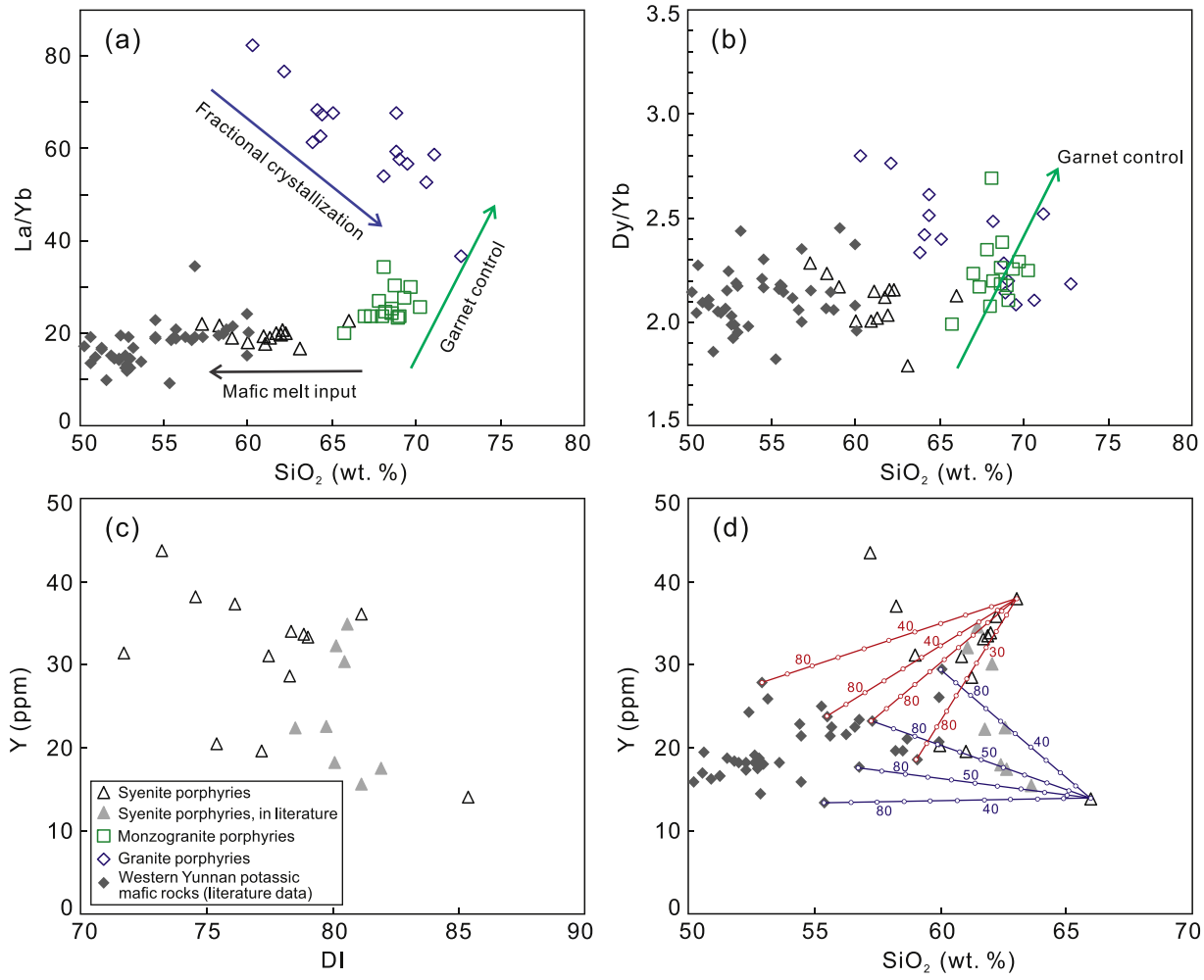


**Fig. 13.** La/Yb vs. $SiO_2$ (a) and Dy/Yb vs. $SiO_2$ (b) plots showing mafic melt input to syenite porphyries, monzogranite porphyries controlled by garnet in the source, and granite porphyries controlled by fractional crystallization. (c) Y vs. DI. (d) Y vs. $SiO_2$ showing the possible mixing between the coeval potassic mafic rocks and syenite porphyries in western Yunnan. Data sources are as in Fig. 8 and Fig. 11.

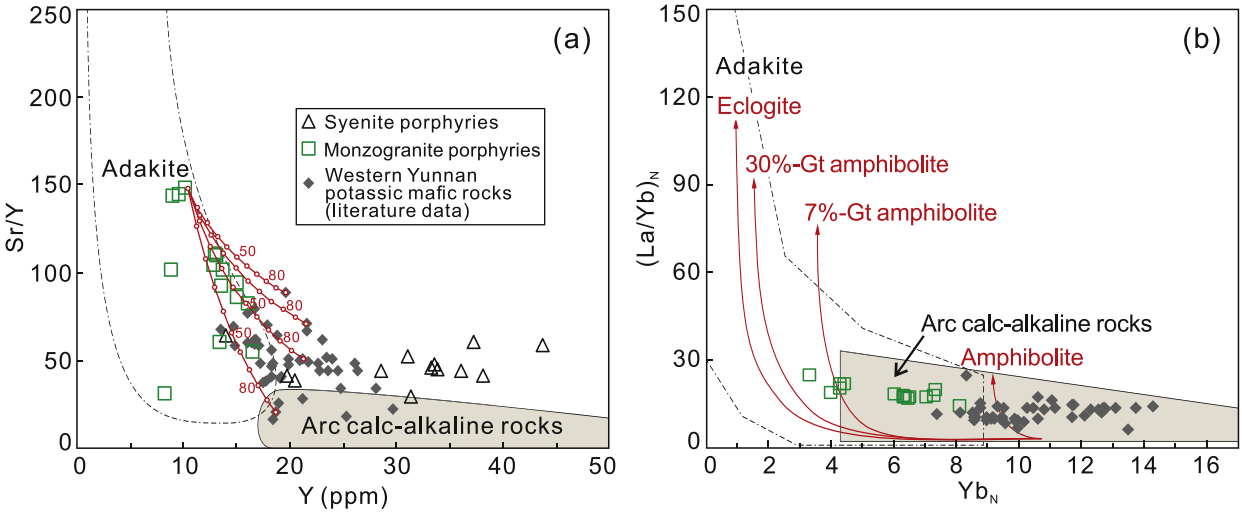


**Fig. 14.** Adakite discrimination diagrams of Sr/Y vs. Y (a) and $(La/Yb)_N$ vs. $Yb_N$ (b) showing the mixing relationships between the coeval potassic mafic rocks and monzogranite porphyries in western Yunnan. Data sources are as in Fig. 11. Data fields of adakite and arc calc-alkaline rocks are based Defant and Drummond (1990) and Petford and Atherton (1996). Red arrows represent batch partial melting trends with different sources (Petford and Atherton, 1996). (For interpretation of the references to colour in this figure legend, the reader is referred to the web version of this article.)

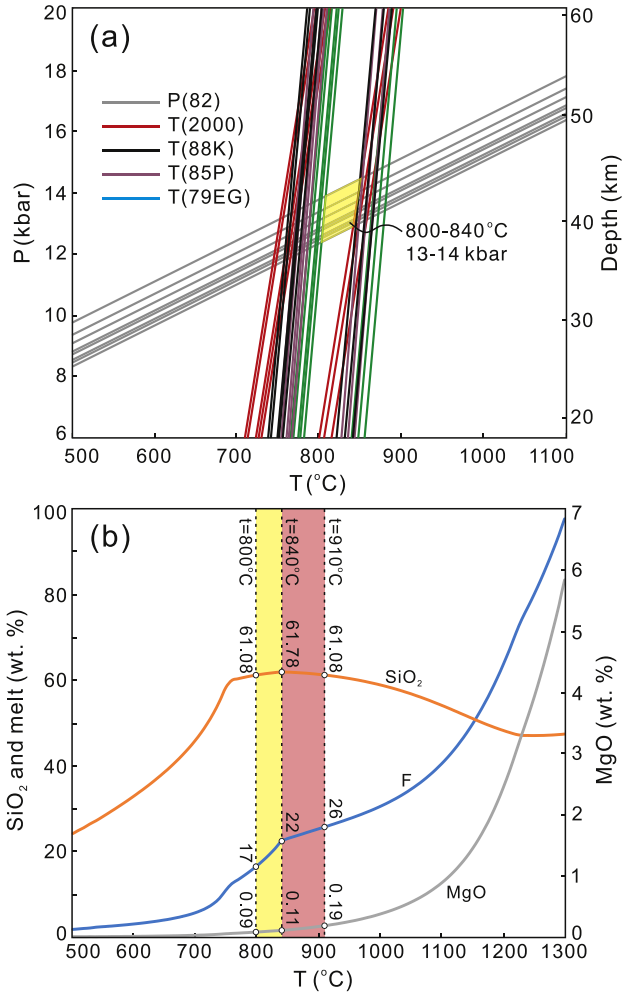


**Fig. 15.** (a) P (kbar)-T (°C)-D (km) plot showing the forming conditions of garnet-clinopyroxene granulite xenolith (LHB1717). (b) Mass fraction (wt%) vs. T (°C) plot showing the melt compositions of partial melting of lower crust amphibolite from western Yunnan. F, mass fraction of melt in the system.

and ultrapotassic intrusive rocks in Dali, Lüchun and nearby localities share similar ages of ~ 35 Ma, dated using zircon U-Pb, and whole-rock, phlogopite, and sanidine $^{40}Ar/^{39}Ar$ methods (Guo et al., 2005; He et al., 2016; Huang et al., 2010; Lu et al., 2012). The largest of the alkaline rocks along the ASRR shear zone is the FanSiPan intrusion located in northern Vietnam (Chung et al., 2008), which has a titanite U-Pb age of ca. 35 Ma (Zhang and Schärer, 1999). About 10 km south of the FanSiPan intrusion, there is another suite of potassic igneous rocks coined as the PuSamCap complex, comprising mafic to felsic undeformed intrusive and subvolcanic bodies (Phan, 1991), with varying $^{40}Ar/^{39}Ar$ ages between ca. 36 Ma and 29 Ma (Chung et al., 2008). Both suites are geochemically comparable to the igneous suites in western Yunnan (Chung et al., 2008).

We obtained fifteen zircon U-Pb ages of 34.5 to 36.9 Ma (Figs. 6, 7) on potassic intrusions from the central segment of the Sanjiang region. Using our new age data and the ages in the literature, we recognize that potassic-ultrapotassic magmatism is younger in the south and east than those in the north and west along the Jinsha suture (Fig. 1b, Fig. 2, Deng et al., 2014).

### 6.2. Petrogenesis of the potassic felsic suites in western Yunnan

#### 6.2.1. Petrogenesis of the shoshonitic syenite porphyries

Coeval shoshonitic mafic and felsic suites in western Yunnan exhibit continuous trends in major element compositions (Lu et al., 2013). They also have similar Sr-Nd-Pb isotope compositions and parallel REE and trace element patterns (Fig. 10a, b; Fig. 11). Thus, it can be argued that the shoshonitic syenite porphyries in western Yunnan may have evolved from mafic magmas parental to the coeval shoshonitic mafic suites (Lu et al., 2013).

The mafic suites show a compositional spectrum from trachybasalt to latite, dominated by lamprophyres in volcanic pipes of dikes closely controlled by subsidiary fractures or faults (Guo et al., 2005; Huang et al., 2010; Li et al., 2002; Lu et al., 2013). The mafic suites from western Yunnan share the same Sr-Nd-Pb isotope compositions (Fig. 11). These observations may reflect the fractionation of olivine, clinopyroxene and plagioclase, resulting in negative correlations of $TiO_2$, $TFe_2O_3$, MgO, CaO, Ni, Cr, and Eu/Eu* with $SiO_2$ (Fig. 12), However, simple fractional crystallization is inadequate because it cannot effectively explain the varying La/Yb and Dy/Yb with increasing $SiO_2$ (Fig. 13a, b) nor the scattered Y variation with increasing of DI and $SiO_2$ (Fig. 13c, d). The fractionation process is also inconsistent with the mafic rocks being parents for the syenite porphyries (Fig. 14a). Therefore, it is unlikely that the syenite porphyries simply resulted from fractional crystallization dominated evolution from magmas parental to the coeval mafic suites.

Nevertheless, the magmas parental to the coeval potassic mafic suites may be involved in the petrogenesis of the syenite porphyries as illustrated by mixing modelling (Fig. 13d). The mixing model also explains the continuous trends between the coeval mafic and felsic suites in $SiO_2$ (Fig. 12 a-d) variation plots and in Sr/Y vs. Y space (Fig. 14a).

The syenite porphyries have a narrow bulk-rock $\varepsilon_{Nd}(t)$ (−5.4–−3.3) and $^{87}Sr/^{86}Sr$ (0.707407–0.707774; Fig. 11a), and a varying zircon $\varepsilon_{Hf}(t)$ range with up to 7 epsilon units (Fig. 8), which is similar to a previous study (e.g., Lu et al., 2013). In the Sr-Nd isotopic mixing modelling, all the syenite porphyry samples plot along the mixing curve between the Jinshanjiang MORB and the Yangtze craton amphibolite (Fig. 11a). These observations indicate mantle material contribution. Mature continental crustal material is also important for the petrogenesis of the syenite porphyries as evidenced by the captured zircons (Fig. 7a-c).

Diverse crustal xenoliths are entrained in the potassic felsic intrusions (especially syenite porphyry). We have done a detailed mineralogical study and thermodynamic modelling on the granulite xenoliths in the syenite porphyries (Fig. 15) to constrain the source (see below).

#### 6.2.2. Petrogenesis of the monzogranite porphyries

The monzogranite porphyries in this study have high Sr, low Y, and Yb contents, with Sr/Y ratios of 30.5–148, resembling adakite-like rocks (Fig. 14). The adakitic signature could be achieved through (a) melting of subducted young and hot oceanic crust (Defant and Drummond, 1990); (b) melting of the subducted continental crust (Wang et al., 2008); (c) fractional crystallization of clinopyroxene which is selectively enriched in HREEs (Richards and Kerrich, 2007); (d) melting of delaminated lower continental crust (Wang et al., 2006); and (e) melting of thickened mafic lower continental crust (Chung et al., 2003).

Given the post-collisional intracontinental setting of the Yangtze craton in Eocene-Oligocene (Yang, 1998), we can rule out the scenarios of melting subducting oceanic or mafic lower continental crust, which is also consistent with the low $Mg^{\#}$, MgO, Cr and Ni in these rocks (Fig. 16). In the case of the monzogranite porphyries, there is no decrease in Dy/Yb (Fig. 13b) and Sc (not shown) with increasing $SiO_2$. Amphibole fractionation would preferentially remove middle REEs, leading to concave-up REE patterns, which is not observed (Fig. 10c). Hence, the adakitic signature is unlikely caused by HREE-rich minerals fractionation. Melting of delaminated lower crust could produce melts with adakitic signature, but their reaction with mantle peridotite would result in elevated MgO, Cr and Ni (Wang et al., 2006), but the monzogranite porphyries do not have such signature (Fig. 16). Hence, the monzogranite porphyries with an adakitic signature is most consistent with their derivation from melting of the thickened lower crust (Fig. 16; Wang et al., 2006).

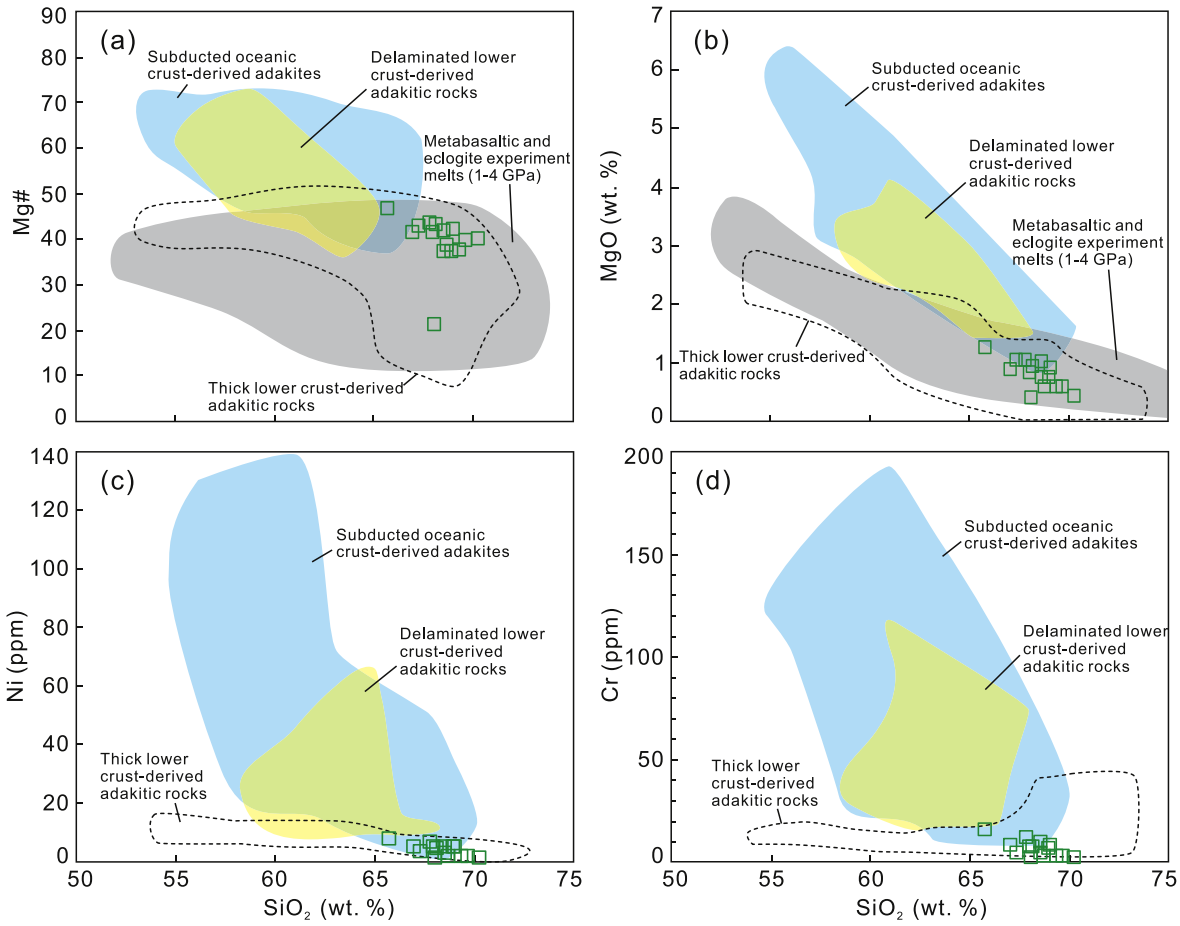


**Fig. 16.** Mg-number ($Mg^{\#}$) vs. $SiO_2$ (wt%) (a), MgO (wt%) vs. $SiO_2$ (wt%) (b), Ni (ppm) vs. $SiO_2$ (wt%) (c) and Cr (ppm) vs. $SiO_2$ (wt%) (d) plots showing the sources of adakitic rocks in western Yunnan (modified from Wang et al., 2006).

In comparison with typical adakitic melts (Defant and Drummond, 1990), the monzogranite porphyries have higher Y contents, and most of the samples are plotted on the boundary of the field of adakite (Fig. 14a). Like the coeval potassic mafic suites, the felsic adakitic rocks from western Yunnan show a wide range of bulk-rock $\varepsilon_{Nd}(t)$ of −7.8 to +1.8 (Fig. 11a). The monzogranite porphyries have a wide span of zircon $\varepsilon_{Hf}(t)$ (−0.1 to +6.3, >6 epsilon units; Fig. 8). These observations imply the involvement of mantle-derived material.

Dioritic mafic microgranular enclaves (MMEs) are present in the monzogranite porphyries, that could represent mafic melts involved in the origin of the monzogranites (e.g., Barbarin, 2005). It is suggested that the dioritic enclaves were formed coeval with the hosted in Eocene at ca. 36 Ma by mixing between mafic potassic and adakite-like melts, derived from metasomatized lithospheric mantle and thickened lower crust, respectively (cf. He et al., 2016), emphasizing the importance of both thermal and compositional input of the mantle-derived mafic potassic component into the petrogenesis of the monzogranite porphyries.

Mixing models between the adakitic monzogranite porphyries and the potassic mafic rocks from western Yunnan with the variates of Sr/Y and Y are shown in Fig. 14a, and most of the monzogranite porphyries samples plot along a mixing curve, indicating the involvement of coeval mafic melts.

The monzogranite porphyries have Nd and Hf isotopic decoupling (Fig. 8, 11a). Based on the zircon $\delta^{18}O$ data, there is no significant supracrustal contamination to these potassic suites (Lu et al., 2013). The potassic mafic suites and amphibolite from western Yunnan share the same enriched Nd isotope compositions (Fig. 11a). Therefore, this isotopic decoupling might be inherited from the source or controlled by magma mixing.

*6.2.3. Petrogenesis of the granite porphyries*

The granite porphyries show varying major and trace element compositions with a wide range of DI (Fig. 9b, c, Fig. 10e, f). A positive correlation between DI and A/CNK is present (Fig. 9c). All these imply the process of fractional crystallization, which could be distinguished using incompatible trace elements with different bulk solid/melt partition coefficients (Schiano et al., 2010). The granite porphyries show an almost horizontal line in the La/Sm vs. La diagram (Fig. 17a), suggesting effect of fractional crystallization.

The negative correlation of $Eu/Eu^*$ with $SiO_2$ and DI (Fig. 17b, c) are linked to significant fractionation of plagioclase+K-feldspar (cf. Hanson, 1978; Shao et al., 2015). The positive correlation between Sr and Ba and the negative correlation defined by Sr vs. Rb/Sr (Fig. 18) are related to K-feldspar fractionation (e.g., Wang et al., 2015). But, as the product in the late stage of magmatic evolution, it is unlikely to be caused by K-feldspar fractionation. This signature could also be interpreted as fractionation of plagioclase and biotite. The crystallization modelling shows that the Ba, Sr and Rb data can be achieved by 10–70% fractionation of 63% plagioclase and 37% biotite starting from the assumed parent composition represented by the least fractionated sample of XY1504 (Fig. 18).

The granite porphyries display a negative correlation between La/Yb and $SiO_2$ (Fig. 13a). The least fractionated sample (XY1504) has higher ΣREE relative to most of the fractionated samples (Fig. 10e). These observations are opposite to the expected trend of magmatic evolution. Considering the low La/Yb values of the mafic suites from western Yunnan, and the concentrated zircon $\varepsilon_{Hf}(t)$ of the granite porphyries (Fig. 8, Fig. 13a), it is unlikely such trend can be caused by the involvement of the mafic component.

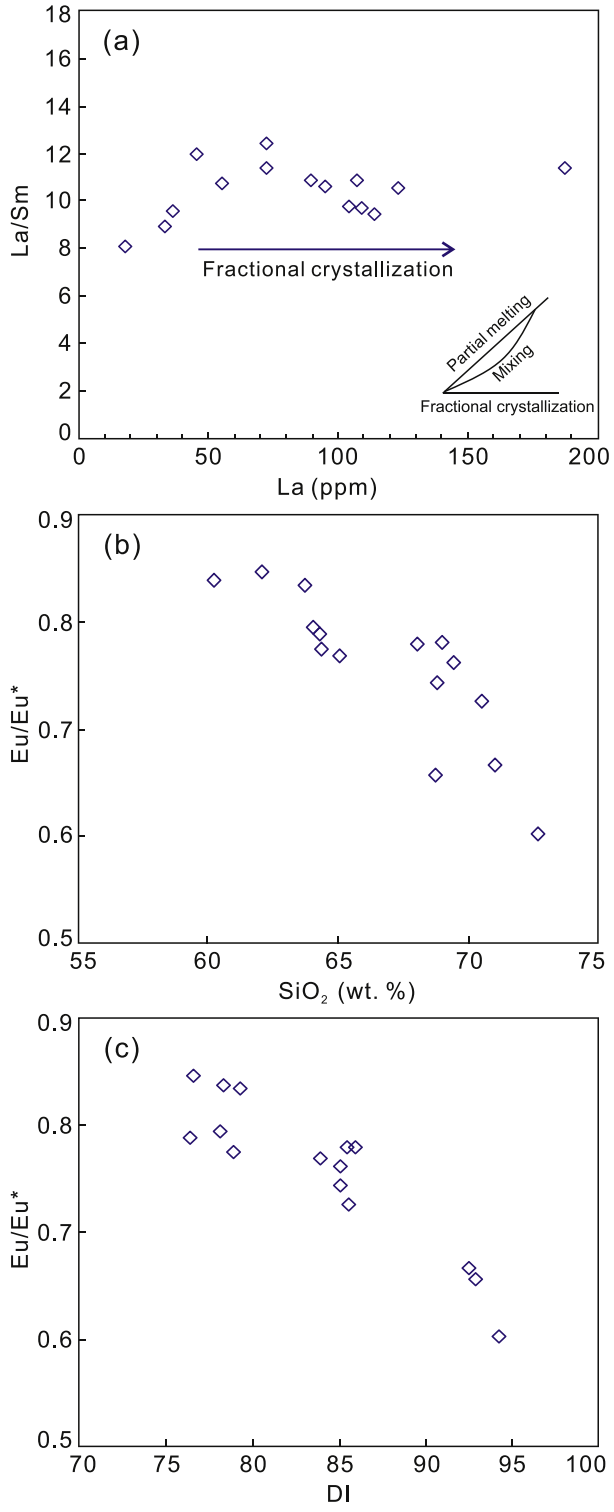


**Fig. 17.** La/Sm vs. La (ppm) (a, modified from Schiano et al., 2010), Eu/Eu* vs. $SiO_2$ (wt%) (b) and Eu/Eu* vs. DI (c) plots showing granite porphyries controlled by fractional crystallization.

However, the inverse La/Yb-$SiO_2$ correlation can be readily explained by apatite fractionation as modeled (see Fig. 10e) and as indicated by the significant positive La/Y-$P_2O_5$ correlation ($r = 0.75$) and inverse La/Y-$P_2O_5$ correlation ($r = -0.91$). The modelling shows that the varying REE abundances of the granite porphyries can be achieved by 1–8% fractional crystallization of apatite from the assumed compositions (Fig. 10e).

*6.2.4. Granulite xenolith and the source of the potassic felsic suites*

Diverse crustal xenoliths from different depth are entrained by the potassic felsic intrusions (especially syenite porphyry), which including garnet clinopyroxenite, garnet two-pyroxene granulite, banded gneiss, and amphibolite (Fig. 3a–c). Xenoliths from the mantle are absent. According to the estimated formation conditions, garnet-diopside amphibolite and pyroxene granulite xenoliths are thought to have originated from a depth of ca. 45 to 55 km, and ca. 30 km depth for a garnet amphibolite xenolith (Zhao et al., 2003). We have also studied the petrology and mineral chemistry on a garnet-clinopyroxene granulite xenolith (LHB1717) from the syenite porphyries. As described above, the garnet-clinopyroxene granulite was formed under the conditions of high-pressure granulite facies, and only the peak assemblage of Gt + Cpx + Pl + Qtz is considered.

Garnet is widely spread in various metamorphic rocks with variable compositions under different metamorphic facies. Forming conditions of metamorphic rocks can be estimated using garnet compositions in terms of members. Garnet formed under amphibolite facies are dominated by almandine, and more pyrope under granulite and eclogite facies (cf. Jin and Li, 1986). Garnets from the garnet-clinopyroxene granulite (LHB1717) plot in the eclogite field near the boundary of granulite facies (Fig. 5b), corresponding to the petrographical observation of high-pressure granulite facies conditions.

Geothermobarometers are widely used to deduct P-T conditions of metamorphic rocks. However, diffusion and re-equilibrium are common during the retrograde stage (Fig. 4c, d), and it is important to determine the equilibrium between garnet, clinopyroxene, and plagioclase. The impact of retrograde is related to temperature and grain size. In fine-grained minerals, diffusion effect may completely change the original compositions. Hence, the core compositions of coarse grains of garnet, clinopyroxene, and plagioclase are used to constrain the peak temperature and pressure of the garnet-clinopyroxene granulite (LHB1717). Gt-Cpx-Pl-Qtz geobarometer calibrated by Newton and Perkins (1982) and different Gt-Cpx geothermometers calibrated by Ellis and Green (1979), Powell (1985), Krogh (1988) and Ravna (2000) are used to determine the peak conditions of equilibrium between garnet, clinopyroxene, and plagioclase. These give temperature in the range of 800 °C to 840 °C and pressure of ~ 13 kbar to 14 kbar, which corresponds to depth of ca. 40–42 km (Fig. 15a), similar to the conditions of high-pressure granulite facies (O'Brien and Rötzler, 2003), coinciding with the experimental results of partial melting of amphibolites under lower crust conditions (PatiÑO Douce and Beard, 1995).

Garnet from the garnet-clinopyroxene granulite has a homogeneous core domain, as described above, indicating continual intra-crystalline diffusion under a high temperature. Therefore, the actual peak temperature might be higher than calculated.

Thermodynamic modelling is increasingly used to reveal crystallization and melting in magmatic systems. The thermodynamic modelling software rhyolite-MELTS (Gualda et al., 2012) is designed for capturing the initiation and evolution of silicic magmas (Gualda and Ghiorso, 2015). Considered that the calibration for mafic systems is identical to felsic systems, and the software takes advantage of the much-improved calculation algorithms covered in it, it could also be used in mafic magma systems (Gualda and Ghiorso, 2015).

Thermodynamic modelling is performed, under the pressure of 14 kbar, on the xenolith of amphibolite (HQBT14, Fig. 15b), which has the same Sr-Nd-Pb isotopic compositions with the host Liuhe syenite porphyries. This modelling illustrates the compositions of the melt derived from partial melting of the amphibolite with increasing temperature. In the temperature measured by geothermobarometers range of 800–840 °C, the melt has the largest $SiO_2$ content of 61.08–61.78 wt%, which is very close to the average $SiO_2$ content of the syenite porphyries (61.10 wt%) (Fig. 15b). In the temperature range from 800 °C to 910 °C, the melts, account for 17–26 wt% in the system, show a similar composition, except for $TiO_2$, with a narrow $SiO_2$ range of 61.08–61.78 wt%,

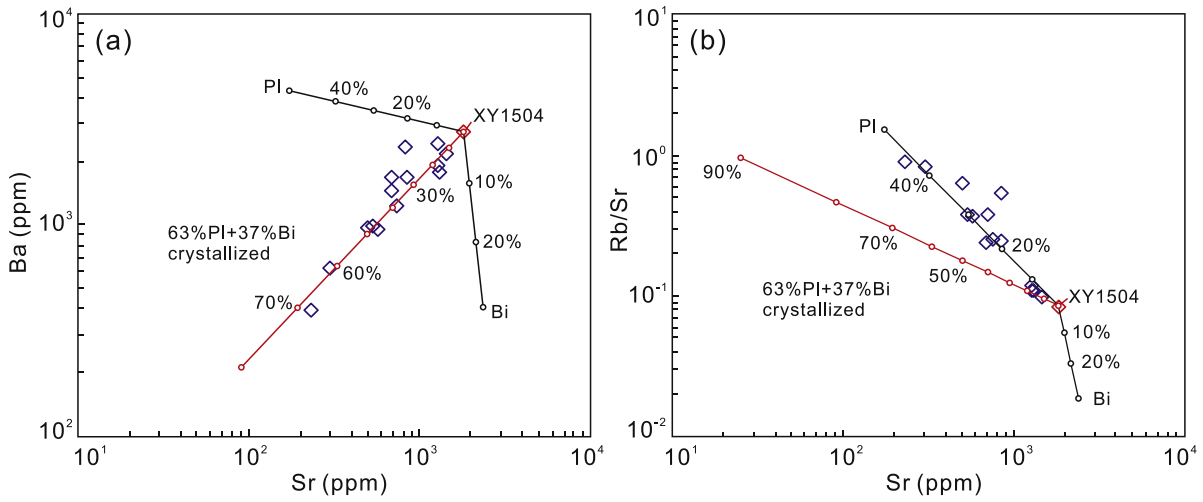


**Fig. 18.** Ba (ppm) vs. Sr (ppm) (a) and Rb/Sr vs. Sr (ppm) (b) showing fractionation of plagioclase and biotite. Partition coefficients are from Wang et al. (2015) and references therein.

MgO of 0.09–0.19 wt% (Fig. 15b), and have the highest $K_2O$ varying from 3.45 wt% to 4.88 wt%, with an average of 4.41 wt%. However, the MgO contents of the melts under the temperature of 800–910 °C (0.09–0.19 wt%, Fig. 15b) are far less than that of the measured syenite porphyries (1.18–3.90 wt%, Fig. 12c).

The syenite porphyries have a varying zircon $\varepsilon_{Hf}(t)$ values (Fig. 8). The potassic mafic suites in western Yunnan are derived from the metasomatized lithospheric mantle under the Yangtze craton (Guo et al., 2005; Huang et al., 2010; Li et al., 2002; Lu et al., 2015; Xu et al., 2001). These suites have a relatively wide bulk-rock $\varepsilon_{Nd}(t)$ range (−11.8 to +3.9) and $^{87}Sr/^{86}Sr$ (0.705053–0.709781) (Li et al., 2002; Guo et al., 2005; Lu et al., 2015, Fig. 11a). Hence, additional input from coeval potassic mafic melts explains the higher MgO in the samples than in the model results.

These modelling results suggest that the amphibolites from the lower crust have the potential to be the source rocks of the potassic felsic suites in western Yunnan, which is also supported by the overlap major element compositions within the fields of experimental melts of amphibolites (Fig. 12a–d), although melt loss and addition may occur subsequently.

All these three groups of potassic felsic rocks share the same bulk-rock Sr-Nd-Pb isotopic compositions with the adakitic rocks in western Yunnan and the amphibolite from the western Yunnan lower crust (Fig. 11), implying a common mafic lower crust source.

For the syenite porphyries, partial melting occurred under the conditions of the high-pressure granulite facies. High-pressure granulite mostly represents rocks formed as a result of short-lived tectonic events that led to crustal thickening or subduction of the crust into the mantle (O'Brien and Rötzler, 2003). Considering the intracontinental setting in the period of Eocene-Oligocene in the west margin of the Yangtze craton, (Yang, 1998) the potassic syenite porphyries in western Yunnan were more likely derived from partial melting of thickened mafic lower crust in the depth of 40–42 km or deeper. The main melt extraction process occurred under the temperature of 800–910 °C, with the extent of 17–26% of partial melting of the amphibolites from the lower crust.

For the adakite-like monzogranite porphyries, the fractionated REE patterns, with $(La/Yb)_N$ range from 14.01 to 24.32, imply garnet exists in the source as a residual phase, which is also suggested by the positive correlation between La/Yb, Dy/Yb and $SiO_2$ (Fig. 13a,b). In contrast, the flat middle to heavy REE patterns of the syenite and granite porphyries (Fig. 10a, e) suggest these are not partial melts of a garnet-bearing protolith.

For the granite porphyries, they contain the highest LREE contents (Fig. 10e). The abundance of LREE depends on degrees of partial melting. The lower of the degree of partial melting, the higher LREE content be obtained. These three groups of potassic felsic rocks are originated from a common mafic lower crust. The highest LREE contents of the granite porphyries indicates the lowest degree of partial melting in the source. Although LREE-rich mineral fractionated, the features of high LREE content remain on the less evolved samples (Fig. 10e).

In summary, the Eocene-Oligocene potassic felsic rocks in western Yunnan share a common mafic lower crust. The syenite and granite porphyries were derived by partial melting of garnet-free amphibolite from the mafic lower crust, and the adakite-like monzogranite porphyries by garnet-bearing amphibolite in a thickened lower crust.

### *6.3. Genetic relationships between the potassic intrusions and the ASRR sinistral shearing*

Analog experiments and various onland large-scale geological features, including ophiolite belts, Mesozoic basins, Permian basalts, Triassic arc volcanos, Cretaceous granites, and Permian gabbros indicate that the total left-lateral offset along the ASRR shear zone is 700 ± 200 km, and was accompanied by the opening of the South China Sea (Briais et al., 1993; Leloup et al., 1995; Tapponnier et al., 1990). The resultant 550 km of N-S extension in the South China Sea was also postulated to represent the total left-lateral offset (Briais et al., 1993). However, integrating the onland left-lateral displacements with offshore right-lateral movements along a transcurrent fault, the left-lateral displacement is less than ~ 280 km (Clift et al., 2008). By considering the E-W extension offshore northern Vietnam, Mazur et al. (2012) suggested that the total offset along the Ailaoshan-Red River shear zone is ~ 250 km. Four narrow NW-SE oriented high-grade metamorphic complexes, that are, from north to south, are Xuelongshan, Diancangshan, Ailaoshan metamorphic complexes in China and Day Nui Con Voi metamorphic complex in Vietnam, are exposed along the ASRR shear zone. Intense ductile deformation showing sinistral shearing were detected widely in these metamorphic rocks. It is generally accepted that Cenozoic strike-slip shearing along the shear zone is the main process for the occurrence of these structural characteristics in high-grade metamorphic rocks.

For the spatial association between the potassic suites and the ASRR shear zone, it has long been emphasizing that there is a genetic link between them (e.g., Guo et al., 2005). Based on the zircon and titanite U-Pb age of 35.0 ± 0.1 Ma for a monzonitic intrusion from Jianchuan, Schärer et al. (1994) argue that the potassic intrusions which follow the trend of the shear zone most likely represent the surface expression of early activity of the shear zone; the strike-slip movement had already occurred

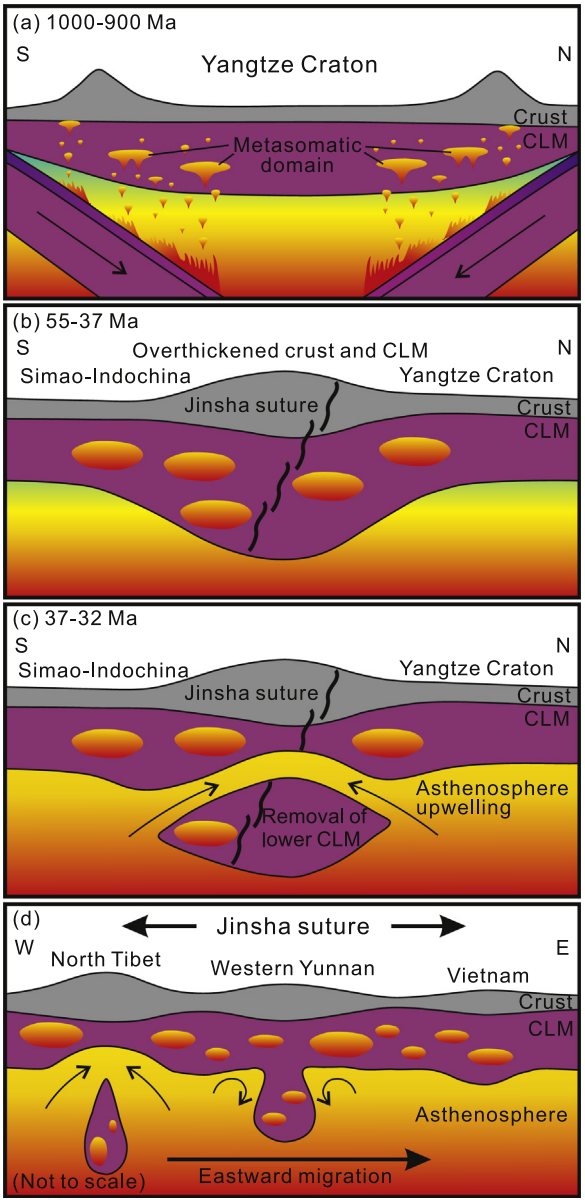


**Fig. 19.** Schematic illustration for the tectonic evolution of the west margin of the Yangtze Craton and Jinsha suture (modified from Lu et al., 2013). (a) Symmetrical seafloor subduction from the northern and southern margins of the Yangtze Craton before 900 Ma; (b) India-Asia continental collision overthickened the crust and continental lithospheric mantle (CLM) between ca. 55 and 37 Ma; (c) The lower overthickened CLM removed along the Jinsha suture between ca. 37 and 32 Ma; (d) Eastward dischronal thickening and removing of the lower CLM along the Jinsha suture in Eocene-Oligocene.

as early as ~ 35 Ma, and potassic magmatism initiated in direct relation to this activity. Based on the zircon U-Pb age of 36.3 ± 0.5 Ma for a quartz monzonite porphyry from Beiya, Liang et al. (2007) suggested the onset of the sinistral movement began at or slightly before 36 Ma.

Alternatively, it is suggested that most leucogranites and potassic granites within the ASRR shear zone are pre-kinematic and deformed, after crystallization, at high temperatures within solid-state ductile regime (Chung et al., 2008). Integrating the emplacement ages of potassic felsic intrusions within the ASRR shear zone, Lu et al. (2012) concluded that the sinistral movement along the shear zone was commencing after 31.9 Ma and terminating before 21.7 Ma. suggested that the left-lateral shearing occurred from 34 Ma to 21 Ma, based on in situ Th-Pb ion microprobe dating of monazite from garnet mica schist and paragneiss within the shear zone. According to the research of leucogranitic dikes within the shear zone, Zhang and Schärer (1999) proposed that strike-slip displacement lasted from 33 Ma to 22 Ma. SHRIMP monazite Th-Pb ages of variably-deformed leucogratic dikes sampled inside of the shear zone are between 29.9 Ma and 22.6 Ma (Sassier et al., 2009). Based on the structural and microstructural analysis, the pre-, *syn*-, and post-kinematic granitic intrusions in the Diancangshan complex were distinguished, respectively, which were spatially confined to the shear zone and temporally related to the sinistral movement along the ASRR shear zone (Cao et al., 2011). Combined with the results of zircon SHRIMP and LA-ICP-MS U-Pb isotopic dating, it is suggested that the left-lateral shearing was initiated at ca. 31 Ma, culminated between ca. 27 Ma and 21 Ma resulting in high-temperature conditions and diminished at ca. 20 Ma at relatively low temperatures (Cao et al., 2011).

U-Pb dates of potassic intrusions along the ASRR shear zone were determined to be 34.0–36.3 Ma (12 samples, Liang et al., 2007), 32.5–36.9 Ma (22 samples, Lu et al., 2012), and 36.0–36.7 Ma (Beiya monzogranite porphyries, He et al., 2016). There are no potassic suites younger than 32 Ma occurring away from the ASRR shear zone (Lu et al., 2012). Our 15 new zircon U-Pb ages (34.5 to 36.9 Ma; Fig. 6, Fig. 7) for the potassic magmatism in western Yunnan supports the previously published results.

The Eocene-Oligocene potassic magmatism, as mentioned above, has occurred throughout north Tibet extending to western Yunnan and Vietnam, and continued from ~ 44 Ma to ~ 24 Ma (Chung et al., 2005, 2008). In western Yunnan, it extends over a 300 km wide zone across the Simao-Indochina block and Yangtze craton (Fig. 2, Guo et al., 2005; Lu et al., 2012).

Hence, the Eocene-Oligocene potassic magmatism in western Yunnan predates the initiation of the ASRR shear zone. These intrusions within or away from the ASRR shear zone cannot constrain the timing of the shearing. There is neither temporal nor spatial correlation between the potassic magmatism and the shearing activity, let alone genetic. The potassic magmatism is more likely related to a regional thermal anomaly (Chung et al., 2005).

### 6.4. Geodynamic and tectonic implications

All the samples in this study are from western Yunnan, the western margin of the Yangtze Craton. The coeval mafic suites in western Yunnan have been argued as resulting from partial melting of metasomatically enriched subcontinental lithospheric mantle (e.g., Chen et al., 2017; Guo et al., 2005; Huang et al., 2010; Li et al., 2002; Lu et al., 2015; Xu et al., 2001). Several models have been proposed to explain the origin of the metasomatism: (1) The lithospheric mantle beneath western Yangtze Craton in western Yunnan was heterogeneously enriched by fluids derived from earlier phases of late Proterozoic and Paleozoic subduction beneath the western part of the Yangtze Craton (e.g. Deng et al., 2014; Guo et al., 2005; He et al., 2016; Lu et al., 2013, 2015). (2) Assuming that the late Permian Emeishan flood basalt volcanism would have purged the lithospheric mantle of all its fusible constituents, the metasomatism is thought to be younger than 250 Ma (Huang et al., 2010; Xu et al., 2001), probably more recent than the Emeishan large igneous province magmatism in the late Permian in the region, and the metasomatic agent must have been melt from the seismic low-velocity zone beneath the lithosphere (Huang et al., 2010). (3) A younger enriched lithospheric mantle at 40–50 Ma was invoked as an exotic Tibetan lithosphere extrusion towards beneath the Yangtze Craton (Xu et al., 2001). Meanwhile, there have also been models proposed to explain cause of the magmatism: (a) The ASRR shearing sliced the lithosphere (Leloup et al., 1995), causing reactivation of pre-existing lithosphere faults (Guo et al., 2005), asthenosphere upwelling and decompression melting of metasomatized mantle lithosphere (Liang et al., 2007). (b) Considering the shearing movement was sinistral and transpressional during the period of middle Eocene to late Oligocene (Wang and Burchfiel, 1997), Liang et al. (2006) proposed that there was a nonnegligible vertical component of the overall compressional component of the shearing movement. This vertical

component pushed adjacent continental blocks into the upper mantle and caused local eastward continental subduction of Simao-Indochina block along the ASRR shear zone, and fluid infiltration into the overlying mantle wedge and subsequent melting (Wang et al., 2001). (c) Removal of the lower continental lithospheric mantle by convective thinning (Deng et al., 2014; He et al., 2016) or delamination (Chen et al., 2017; Lu et al., 2015; Zhao et al., 2009).

The western Yangtze Craton has been shown to have undergone seafloor subduction from ~ 1040 Ma to ~ 900 Ma, beneath its northern and southern margins. This was followed by mantle plume-related magmatic activity from ~ 825 Ma to ~ 750 Ma associated with Rodinia breakup, leaving behind widespread mafic dike swarms, continental flood basalts, and continental rifting over much of the margin of the Yangtze Craton (Li et al., 2008) although there are different views (Xia et al., 2018). Then the Yangtze Craton became an isolated terrane floating in the Paleo-Pacific Ocean with a passive continental margin on the west of the craton until the Late Triassic (Pullen et al., 2008). At ~ 260–250 Ma, the craton was thermally eroded by the Emeishan mantle plume-related activity (Huang et al., 2010; Lu et al., 2013). Since the Late Triassic, the Yangtze Craton had occupied an intracontinental setting (Yang, 1998).

The enriched bulk-rock Sr-Nd-Pb isotopic compositions of the Eocene-Oligocene potassic mafic suites indicate a long-lived enrichments of the Yangtze lithospheric mantle. These mafic rocks share the same enriched Sr-Nd isotopic compositions with the Neoproterozoic mafic rocks and Late Permian Emeishan low-Ti basalts (Lu et al., 2015). This suggests that the metasomatism as a result of seafloor subduction remained preserved in the lithospheric mantle despite the possible influence of plume activities in the Neoproterozoic and Permian (Lu et al., 2015). The Paleogene post-collisional lamprophyres from western Yunnan (Lu et al., 2015), are consistent with a model of subcontinental lithospheric mantle metasomatism by melt from the seismic low-velocity zone (depleted upper mantle) beneath the lithosphere (Huang et al., 2010). Hence, it is more likely that the enriched lithospheric mantle was metasomatized by Proterozoic seafloor subduction beneath the Yangtze Craton (Fig. 19a, e.g., Lu et al., 2013, 2015; Deng et al., 2014; He et al., 2016).

Although the ASRR shearing zone is tectonically important, it is not the cause of the magmatism under study in western Yunnan because there is no spatial and temporal correspondence.The close association of the potassic mafic and felsic suites in space and time in western Yunnan indicates their petrogenesis resulting from the same tectonic process as a consequence of partial melting of metasomatized mantle lithosphere with the melts (parental to the mafic suites) providing both heat and material for thickened lower crustal melting responsible for the felsic suites (Zeng et al., 2011).

The question is what may have caused the lithospheric mantle melting. We suggest that removal of the lower subcontinental lithospheric mantle occurred beneath the western margin of the Yangtze craton following the India-Asia collision, which may have induced asthenosphere upwelling (Fig. 19b,c). This is consistent with the suggestion for a large-scale mantle diapir derived from ~450 km depth beneath the western Yunnan shown by the seismic tomography (Lei et al., 2009). Upwelling of the hot asthenosphere resulted in partial melting of the metasomatized continental lithospheric mantle, producing the potassic mafic suites in western Yunnan (Fig. 20). Underplating and intrusion of

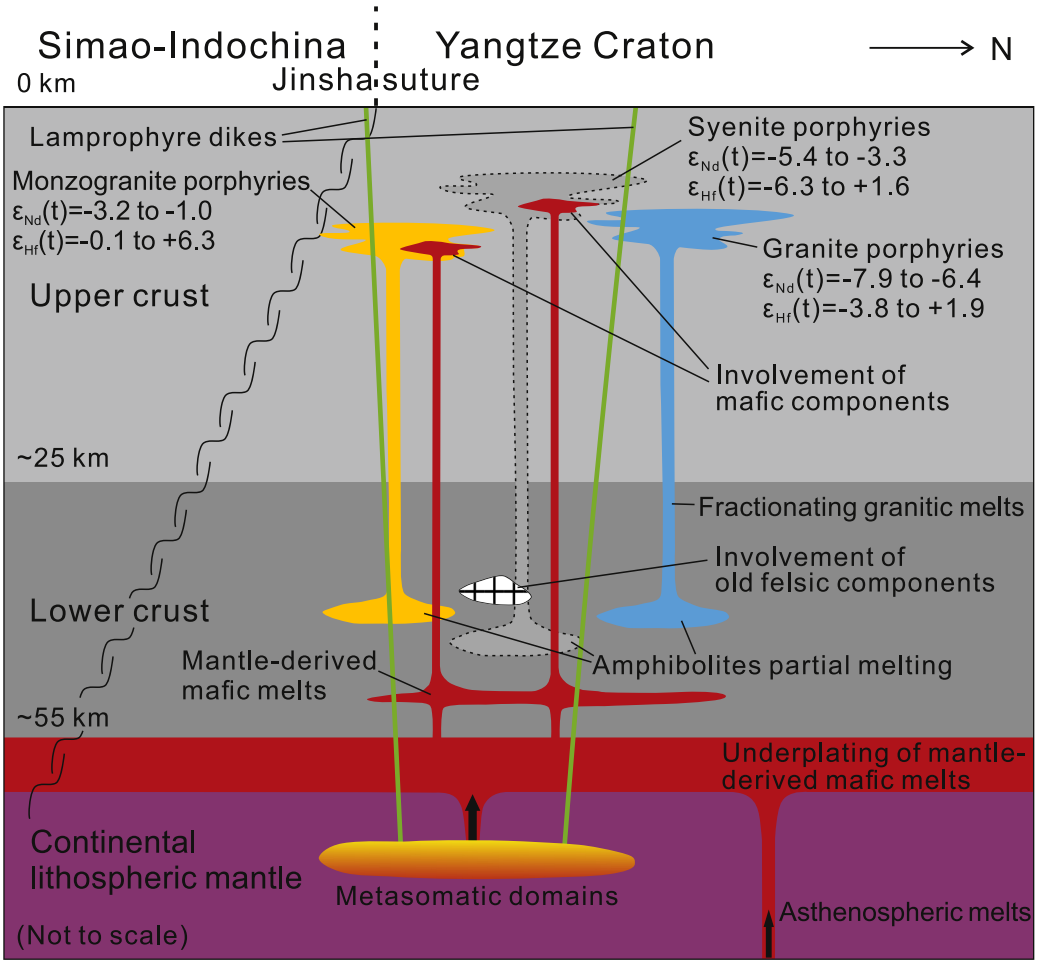


**Fig. 20.** Schematic crustal section during the formation of the potassic suites in western Yunnan in Eocene-Oligocene (modified from Guo et al., 2007; Lu et al., 2013).

these mantle-derived hot mafic melts provide additional heat to the thickened lower crust, causing partial melting and generating the potassic felsic suites in western Yunnan (Fig. 20), These potassic suites are comparable to those in the Qiangtang block (e.g., Long et al., 2015; Zhao et al., 2009). Furthermore, the syenite and monzogranite porphyries resulted from mixing of melts, respectively, parental to the mafic and the felsic suites with the granite porphyries formed as the result of fractional crystallization of plagioclase, biotite, and apatite produces (Fig. 20).

During an intra-plate orogenic event, the lithospheric deformation is localized in the suture zones (Gorczyk et al., 2012), and we conclude that the thickening of the lower crust was localized around the Jinsha suture. The potassic suites in northern Tibetan Plateau have a tectonic setting identical to potassic suites in western Yunnan, both are of Eocene-Oligocene age, and were triggered by removal of the lower lithospheric mantle (Zhao et al., 2009), resulting in the distribution of an Eocene-Oligocene potassic magmatic belt along the entire Jinsha suture (Fig. 1b).

The removal of the lower continental lithospheric mantle could be caused by Rayleigh-Taylor convective instability or lithospheric delamination. Rayleigh-Taylor convective instability depends strongly on the constitutive law relating stress and strain rate, and the bottom of a layer of dense material could be swept into drips and thins in response to subjacent asthenospheric convection (Houseman and Molnar, 1997). In contrast, lithospheric delamination emphasizes the peeling of the entire mantle lithosphere (Bird, 1979), which is unlikely because of the presence of the Eocene potassic mafic suites that require a metasomatized lithospheric mantle source (e.g., Guo et al., 2005; Huang et al., 2010; Lu et al., 2015). Therefore, the lithospheric mantle beneath the Jinsha suture was removed by Rayleigh-Taylor convective instability.

The ongoing India-Asia convergence resulted in clockwise rotation of the Indochina, Sibumasu and west Burma blocks, and the extrusion of the Indochina block (Deng et al., 2014). These lithospheric deformations occurred along with shearing along the ASRR shear zone (Deng et al., 2014), which postdates the Eocene-Oligocene potassic magmatism. In this period, the Jinsha suture occupied an NWW strike rather than its present orientation (Deng et al., 2014).

On the northern Tibetan Plateau, the potassic suites exposed in the west are younger than that in the east (Chung et al., 2005). In Vietnam and western Yunnan, the potassic intrusions in the south are younger than that in the north (Fig. 1b, 2, Chung et al., 2008; Zhang and Schärer, 1999; He et al., 2016). For the entire Jinsha suture, the potassic suites in Vietnam and western Yunnan are younger than that in north Tibet (Fig. 1b). All these indicate eastward-migration of the potassic magmatism along the Jinsha suture, further implying eastward thickening and removing of the manlte lithosphere along the Jinsha suture (Fig. 19d).

The removal of the mantle lithosphere followed the Indian-Asian continental collision (Lu et al., 2013; Zhao et al., 2009). Based on the evidence from Cenozoic Gangdese volcano-magmatic rocks in south Tibet, Hou et al. (2006) suggested that tearing of the Indian continental slab took place intensively in the early Eocene (ca. 52 Ma), resulting in dischronal subduction along the India-Asia collision zone. The west part of the subducted continental slab has a gentle angle, whereas it becomes steeper to the east (Hou et al., 2006).

Therefore, within the same period, the subducted continental slab in the west could reach to a far distance than that in the east, causing the dischronal thickening and removing of the mantle lithosphere along the Jinsha suture. The subsequent eastward-migrating potassic magmatism along the Jinsha suture is more likely a tectonic response to the dischronal subduction of the torn Indian continental slab along the India-Asia collision zone.

## 7. Conclusions

(1) The magmas parental to the potassic felsic suites in western Yunnan are generated by partial melting of the thickened mafic lower crust at a depth >40–42 km. The crustal melting is caused by mantle derived mafic magmas (parental to the mafic potassic suites). Mixing of the mafic and felsic melts explains the syenite and monzogranite porphyries and their extended fractional crystallization of plagioclase, biotite and apatite gives rise to the granite porphyries.

(2) The removal of the lower mantle lithosphere and asthenosphere upwelling occurred following the India-Asia collision, which triggers partial melting of the metasomatized mantle lithosphere. Underplating of such mantle-derived mafic melts triggered the thickened lower crust melting.

(3) The initiation of the potassic magmatism predates the ASRR sinistral shearing. There are no temporal, spatial or genetic relationships between the potassic magmatism and the ASRR shear zone activity.

(4) The Eocene-Oligocene potassic magmatism along the Jinsha suture migrates eastward over time, indicating eastward thickening and removing of the mantle lithosphere along the Jinsha suture, as a tectonic response of the dischronal subduction of the torn Indian continental slab along the India-Asia collision zone.

Supplementary data to this article can be found online at https://doi.org/10.1016/j.lithos.2019.04.023.

## Acknowledgments

The authors are indebted to Liangliang Zhang and Zhenzhen Wang for their help with zircon U-Pb isotopic analysis. Yiyun Yang, Jingkai Wu and Zhuang Miao help with EPMA work. This study was funded by grants from the National Key Project for Basic Research of China (2015CB452604), National Key R & D Project of China (2016YFC0600304) and the open research project from the state key laboratory of GPMR (GPMR201817). We are grateful for careful reviews by anonymous reviewers, which greatly helped us improve the paper. Editor Xian-Hua Li was thanked for editorial handling.

## References

Barbarin, B., 2005. Mafic magmatic enclaves and mafic rocks associated with some granitoids of the central Sierra Nevada batholith, California: nature, origin, and relations with the hosts. Lithos 80, 155–177.

Bird, P., 1979. Continental delamination and the Colorado Plateau. J. Geophys. Res. Solid Earth 84, 7561–7571.

Briais, A., Patriat, P., Tapponnier, P., 1993. Updated interpretation of magnetic anomalies and seafloor spreading stages in the south China Sea: Implications for the Tertiary tectonics of Southeast Asia. J. Geophys. Res. Solid Earth 98, 6299–6328.

Cao, S., Liu, J., Leiss, B., Neubauer, F., Genser, J., Zhao, C., 2011. Oligo-Miocene shearing along the Ailao Shan–Red River shear zone: Constraints from structural analysis and zircon U/Pb geochronology of magmatic rocks in the Diancang Shan massif, SE Tibet, China. Gondwana Res. 19, 975–993.

Chen, B., Long, X., Wilde, S.A., Yuan, C., Wang, Q., Xia, X., Zhang, Z., 2017. Delamination of lithospheric mantle evidenced by Cenozoic potassic rocks in Yunnan, SW China: a contribution to uplift of the Eastern Tibetan Plateau. Lithos 284-285, 709–729.

Chung, S.L., Liu, D.Y., Ji, J.Q., Chu, M.F., Lee, H.Y., Wen, D.J., Lo, C.H., Lee, T.Y., Qian, Q., Zhang, Q., 2003. Adakites from continental collision zones: Melting of thickened lower crust beneath southern Tibet. Geology 31, 1021–1024.

Chung, S.L., Chu, M.F., Zhang, Y.Q., Xie, Y.W., Lo, C.H., Lee, T.Y., Lan, C.Y., Li, X.H., Zhang, Q., Wang, Y.Z., 2005. Tibetan tectonic evolution inferred from spatial and temporal variations in post-collisional magmatism. Earth Sci. Rev. 68, 173–196.

Chung, S.L., Searle, M.P., Yeh, M.W., 2008. The age of the potassic alkaline igneous rocks along the Ailao Shan-Red river shear zone: implications for the onset age of left-lateral shearing: a discussion. J. Geol. 116, 201–204.

Clift, P., Lee, G.H., Anh Duc, N., Barckhausen, U., Van Long, H., Zhen, S., 2008. Seismic reflection evidence for a dangerous Grounds miniplate: no extrusion origin for the South China Sea. Tectonics 27.

Cousens, B.L., 1996. Magmatic evolution of Quaternary mafic magmas at Long Valley Caldera and the Devils Postpile, California: Effects of crustal contamination on lithospheric mantle-derived magmas. J. Geophys. Res. Solid Earth 101, 27673–27689.

Cousens, B.L., Chiarenzelli, J.R., Aspler, L.B., 2004. An unusual Paleoproterozoic magmatic event, the ultrapotassic Christopher Island Formation, Baker Lake Group, Nunavut, Canada: Archean mantle metasomatism and Paleoproterozoic mantle reactivation.

In: Eriksson, P., Altermann, W., Nelson, D.R., Mueller, W.U., Catuneanu, O. (Eds.), The Precambrian Earth: Tempos and Events. Elsevier, Amsterdam, pp. 183–201.
Cousens, B.L., Henry, C.D., Harvey, B.J., Brownrigg, T., Prytulak, J., Allan, J.F., 2011. Secular variations in magmatism during a continental arc to post-arc transition: Plio-Pleistocene volcanism in the Lake Tahoe/Truckee area, Northern Sierra Nevada, California. Lithos 123, 225–242.
De la Roche, H., Leterrier, J., Grandclaude, P., Marchal, M., 1980. A classification of volcanic and plutonic rocks using R1R2-diagram and major-element analyses — its relationships with current nomenclature. Chem. Geol. 29, 183–210.
Defant, M.J., Drummond, M.S., 1990. Derivation of some modern arc magmas by melting of young subducted lithosphere. Nature 347, 662.
Deng, W., Huang, X., Zhong, D., 1998. Alkali-rich porphyry and its relation with intraplate deformation of north part of Jinsha River belt in western Yunnan, China. Sci. China Ser. D 41, 297–305.
Deng, J., Wang, Q.F., Li, G.J., Santosh, M., 2014. Cenozoic tectono-magmatic and metallogenic processes in the Sanjiang region, southwestern China. Earth Sci. Rev. 138, 268–299.
Droop, G.T.R., 1987. A general equation for estimating Fe3+ concentrations in ferromagnesian silicates and oxides from microprobe analyses, using stoichiometric criteria. Mineral. Mag. 51, 431–435.
Ellis, D.J., Green, D.H., 1979. An experimental study of the effect of Ca upon garnet-clinopyroxene Fe-Mg exchange equilibria. Contrib. Mineral. Petrol. 71, 13–22.
Gorczyk, W., Hobbs, B., Gerya, T., 2012. Initiation of Rayleigh–Taylor instabilities in intracratonic settings. Tectonophysics 514-517, 146–155.
Gualda, G.A.R., Ghiorso, M.S., 2015. MELTS_Excel: A Microsoft Excel-based MELTS interface for research and teaching of magma properties and evolution. Geochem. Geophys. Geosyst. 16, 315–324.
Gualda, G.A.R., Ghiorso, M.S., Lemons, R.V., Carley, T.L., 2012. Rhyolite-MELTS: a Modified Calibration of MELTS Optimized for Silica-rich, Fluid-bearing Magmatic Systems. J. Petrol. 53, 875–890.
Guo, Z.F., Hertogen, J., Liu, J.Q., Pasteels, P., Boven, A., Punzalan, L., He, H.Y., Luo, X.J., Zhang, W.H., 2005. Potassic magmatism in western Sichuan and Yunnan Provinces, SE Tibet, China: Petrological and geochemical constraints on petrogenesis. J. Petrol. 46, 33–78.
Guo, Z.F., Wilson, M., Liu, J.Q., Mao, Q., 2006. Post-collisional, potassic and ultrapotassic magmatism of the northern Tibetan Plateau: Constraints on characteristics of the mantle source, geodynamic setting and uplift mechanisms. J. Petrol. 47, 1177–1220.
Guo, Z., Wilson, M., Liu, J., 2007. Post-collisional adakites in South Tibet: Products of partial melting of subduction-modified lower crust. Lithos 96, 205–224.
Hanson, G.N., 1978. The application of trace elements to the petrogenesis of igneous rocks of granitic composition. Earth Planet. Sci. Lett. 38, 26–43.
Hart, S.R., 1984. A large-scale isotope anomaly in the Southern Hemisphere mantle. Nature 309, 753–757.
He, W.Y., Mo, X.X., Yang, L.Q., Xing, Y.L., Dong, G.C., Yang, Z., Gao, X., Bao, X.S., 2016. Origin of the Eocene porphyries and mafic microgranular enclaves from the Beiya porphyry Au polymetallic deposit, western Yunnan, China: Implications for magma mixing/mingling and mineralization. Gondwana Res. 40, 230–248.
Hoskin, P.W.O., Schaltegger, U., 2003. The Composition of Zircon and Igneous and Metamorphic Petrogenesis. Rev. Mineral. Geochem. 53, 27–62.
Hou, Z.Q., Ma, H.W., Zaw, K., Zhang, Y.Q., Wang, M.J., Wang, Z., Pan, G.T., Tang, R.L., 2003. The Himalayan Yulong porphyry copper belt: product of large-scale strike-slip faulting in eastern Tibet. Econ. Geol. Bull. Soc. Econ. Geol. 98, 125–145.
Hou, Z.Q., Zhao, Z.D., Gao, Y.F., Yang, Z.M., Jiang, W., 2006. Tearing and dischronal subduction of the Indian continental slab: evidence from Cenozoic Gangdese volcano-magmatic rocks in South Tibet. Acta Petrol. Sin. 22, 761–774 (in Chinese with English abstract).
Houseman, G.A., Molnar, P., 1997. Gravitational (Rayleigh–Taylor) instability of a layer with non-linear viscosity and convective thinning of continental lithosphere. Geophys. J. Int. 128, 125–150.
Huang, X.L., Niu, Y.L., Xu, Y.G., Chen, L.L., Yang, Q.J., 2010. Mineralogical and Geochemical Constraints on the Petrogenesis of Post-collisional Potassic and Ultrapotassic Rocks from Western Yunnan, SW China. J. Petrol. 51, 1617–1654.
Jin, S.Q., Li, H.C., 1986. Introduction to Genetic Mineralogy. Jilin University Press, Changchun, pp. 1–521 (in Chinese).
Krogh, E.J., 1988. The garnet-clinopyroxene Fe-Mg geothermometer — a reinterpretation of existing experimental data. Contrib. Mineral. Petrol. 99, 44–48.
Lei, J., Zhao, D., Su, Y., 2009. Insight into the origin of the Tengchong intraplate volcano and seismotectonics in southwest China from local and teleseismic data. J. Geophys. Res. Solid Earth 114.
Leloup, P.H., Lacassin, R., Tapponnier, P., Scharer, U., Zhong, D.L., Liu, X.H., Zhang, L.S., Ji, S.C., Trinh, P.T., 1995. The Ailao Shan-Red River shear zone (Yunnan, China), Tertiary transform boundary of Indochina. Tectonophysics 251, 3–10.
Li, X.-H., Zhou, H., Chung, S.-L., Lo, C.-H., Wei, G., Liu, Y., Lee, C.-y., 2002. Geochemical and Sr-Nd Isotopic Characteristics of Late Paleogene Ultrapotassic Magmatism in Southeastern Tibet. Int. Geol. Rev. 44, 559–574.
Li, Z.X., Bogdanova, S.V., Collins, A.S., Davidson, A., De Waele, B., Ernst, R.E., Fitzsimons, I.C.W., Fuck, R.A., Gladkochub, D.P., Jacobs, J., Karlstrom, K.E., Lu, S., Natapov, L.M., Pease, V., Pisarevsky, S.A., Thrane, K., Vernikovsky, V., 2008. Assembly, configuration, and break-up history of Rodinia: a synthesis. Precambrian Res. 160, 179–210.
Liang, H.Y., Campbell, I.H., Allen, C., Sun, W.D., Liu, C.Q., Yu, H.X., Xie, Y.W., Zhang, Y.Q., 2006. Zircon Ce4+/Ce3+ ratios and ages for Yulong ore-bearing porphyries in eastern Tibet. Mineral. Deposita 41, 152–159.
Liang, H.Y., Campbell, I.H., Allen, C.M., Sun, W.D., Yu, H.X., Xie, Y.W., Zhang, Y.Q., 2007. The age of the potassic alkaline igneous rocks along the Ailao Shan-Red River shear zone: Implications for the onset age of left-lateral shearing. J. Geol. 115, 231–242.
Liu, Y., Hu, Z., Gao, S., Günther, D., Xu, J., Gao, C., Chen, H., 2008. In situ analysis of major and trace elements of anhydrous minerals by LA-ICP-MS without applying an internal standard. Chem. Geol. 257, 34–43.
Liu, Y., Gao, S., Hu, Z., Gao, C., Zong, K., Wang, D., 2010. Continental and oceanic crust recycling-induced melt–peridotite interactions in the trans-north China Orogen: U–Pb dating, Hf isotopes and trace elements in zircons from mantle xenoliths. J. Petrol. 51, 537–571.
Long, X., Wilde, S.A., Wang, Q., Yuan, C., Wang, X.-C., Li, J., Jiang, Z., Dan, W., 2015. Partial melting of thickened continental crust in central Tibet: evidence from geochemistry and geochronology of Eocene adakitic rhyolites in the northern Qiangtang Terrane. Earth Planet. Sci. Lett. 414, 30–44.
Lu, Y.J., Kerrich, R., Cawood, P.A., McCuaig, T.C., Hart, C.J.R., Li, Z.X., Hou, Z.Q., Bagas, L., 2012. Zircon SHRIMP U-Pb geochronology of potassic felsic intrusions in western Yunnan, SW China: Constraints on the relationship of magmatism to the Jinsha suture. Gondwana Res. 22, 737–747.
Lu, Y.J., Kerrich, R., McCuaig, T.C., Li, Z.X., Hart, C.J.R., Cawood, P.A., Hou, Z.Q., Bagas, L., Cliff, J., Belousova, E.A., Tang, S.H., 2013. Geochemical, Sr-Nd-Pb, and zircon Hf-O isotopic compositions of eocene-oligocene shoshonitic and potassic adakite-like felsic intrusions in Western Yunnan, SW China: petrogenesis and tectonic implications. J. Petrol. 54, 1309–1348.
Lu, Y.J., McCuaig, T.C., Li, Z.X., Jourdan, F., Hart, C.J.R., Hou, Z.Q., Tang, S.H., 2015. Paleogene post-collisional lamprophyres in western Yunnan, western Yangtze Craton: Mantle source and tectonic implications. Lithos 233, 139–161.
Ludwig, K.R., 2003. ISOPLOT 3.0: A Geochronological Toolkit for Microsoft Excel. Berkeley Geochronology Center Special Publication.
Mazur, S., Green, C., Stewart, M.G., Whittaker, J.M., Williams, S., Bouatmani, R., 2012. Displacement along the Red River Fault constrained by extension estimates and plate reconstructions. Tectonics 31.
Morimoto, N., 1988. Nomenclature of Pyroxenes. Mineral. Petrol. 39, 55–76.
Newton, R., Perkins, D., 1982. Thermodynamic calibration of geobarometers based on the assemblages garnet-plagioclase-orthopyroxene (clinopyroxene)-quartz. Am. Mineral. 67.
O'Brien, P.J., Rötzler, J., 2003. High-pressure granulites: formation, recovery of peak conditions and implications for tectonics. J. Metamorph. Geol. 21, 3–20.
PatiÑO Douce, A.E., Beard, J.S., 1995. Dehydration-melting of Biotite Gneiss and Quartz Amphibolite from 3 to 15 kbar. J. Petrol. 36, 707–738.
Petford, N., Atherton, M., 1996. Na-rich partial melts from newly underplated basaltic crust: the cordillera Blanca batholith, Peru. J. Petrol. 37, 1491–1521.
Phan, C.T., 1991. Geology of Campuchea, Laos, and Vietnam. Hanoi, Geological Survey Vietnam. p. 158.
Powell, R., 1985. Regression diagnostics and robust regression in geothermometer/geobarometer calibration: the garnet-clinopyroxene geothermometer revisited. J. Metamorph. Geol. 3, 231–243.
Pullen, A., Kapp, P., Gehrels, G.E., Vervoort, J.D., Ding, L., 2008. Triassic continental subduction in central Tibet and Mediterranean-style closure of the Paleo-Tethys Ocean. Geology 36, 351–354.
Ravna, K., 2000. The garnet–clinopyroxene Fe2+–Mg geothermometer: an updated calibration. J. Metamorph. Geol. 18, 211–219.
Richards, J.P., Kerrich, R., 2007. Special paper: adakite-like rocks: their diverse origins and questionable role in metallogenesis. Econ. Geol. 102, 537–576.
Rickwood, P.C., 1989. Boundary lines within petrologic diagrams which use oxides of major and minor elements. Lithos 22, 247–263.
Roger, F., Tapponnier, P., Arnaud, N., Schärer, U., Brunel, M., Zhiqin, X., Jingsui, Y., 2000. An Eocene magmatic belt across central Tibet: mantle subduction triggered by the Indian collision? Terra Nova 12, 102–108.
Sassier, C., Leloup, P.H., Rubatto, D., Galland, O., Yue, Y., Lin, D., 2009. Direct measurement of strain rates in ductile shear zones: a new method based on syntectonic dikes. J. Geophys. Res. Solid Earth 114.
Schärer, U., Lian-Sheng, Z., Tapponnier, P., 1994. Duration of strike-slip movements in large shear zones: the Red River belt, China. Earth Planet. Sci. Lett. 126, 379–397.
Schiano, P., Monzier, M., Eissen, J.-P., Martin, H., Koga, K.T., 2010. Simple mixing as the major control of the evolution of volcanic suites in the Ecuadorian Andes. Contrib. Mineral. Petrol. 160, 297–312.
Shao, F., Niu, Y., Regelous, M., Zhu, D.C., 2015. Petrogenesis of peralkaline rhyolites in an intra-plate setting: Glass House Mountains, Southeast Queensland, Australia. Lithos 216-217, 196–210.
Smith, J.V., 1974. Nomenclature and General Properties of Feldspars, Feldspar Minerals: Crystal Structure and Physical Properties 1. Springer Berlin Heidelberg, Berlin, Heidelberg, pp. 415–460.
Sun, S.S., McDonough, W.F., 1989. Chemical and isotopic systematics of oceanic basalts: implications for mantle composition and processes. Geol. Soc. Lond. Spec. Publ. 42, 313.
Tanaka, T., Togashi, S., Kamioka, H., Amakawa, H., Kagami, H., Hamamoto, T., Yuhara, M., Orihashi, Y., Yoneda, S., Shimizu, H., Kunimaru, T., Takahashi, K., Yanagi, T., Nakano, T., Fujimaki, H., Shinjo, R., Asahara, Y., Tanimizu, M., Dragusanu, C., 2000. JNdi-1: a neodymium isotopic reference in consistency with LaJolla neodymium. Chem. Geol. 168, 279–281.
Tapponnier, P., Lacassin, R., Leloup, P.H., Schärer, U., Dalai, Z., Haiwei, W., Xiaohan, L., Shaocheng, J., Lianshang, Z., Jiayou, Z., 1990. The Ailao Shan/Red River metamorphic belt: Tertiary left-lateral shear between Indochina and South China. Nature 343, 431.
Todt, W., Cliff, R.A., Hanser, A., Hofmann, A.W., 1996. Evaluation of a 202Pb–205Pb Double Spike for High - Precision Lead Isotope Analysis, Earth Processes: Reading the Isotopic Code. Geophysical Monograph 95. The American Geophysical Union.
Wang, E., Burchfiel, B.C., 1997. Interpretation of Cenozoic tectonics in the right-lateral accommodation zone between the Ailao Shan shear zone and the eastern Himalayan xyntaxis. Int. Geol. Rev. 39, 191–219.

Wang, J.-H., Yin, A., Harrison, T.M., Grove, M., Zhang, Y.-Q., Xie, G.-H., 2001. A tectonic model for Cenozoic igneous activities in the eastern Indo–Asian collision zone. Earth Planet. Sci. Lett. 188, 123–133.

Wang, Q., Xu, J.-F., Jian, P., Bao, Z.-W., Zhao, Z.-H., Li, C.-F., Xiong, X.-L., Ma, J.-L., 2006. Petrogenesis of Adakitic Porphyries in an Extensional Tectonic setting, Dexing, South China: implications for the Genesis of Porphyry Copper Mineralization. J. Petrol. 47, 119–144.

Wang, Q., Wyman, D.A., Xu, J., Dong, Y., Vasconcelos, P.M., Pearson, N., Wan, Y., Dong, H., Li, C., Yu, Y., Zhu, T., Feng, X., Zhang, Q., Zi, F., Chu, Z., 2008. Eocene melting of subducting continental crust and early uplifting of Central Tibet: evidence from central-western Qiangtang high-K calc-alkaline andesites, dacites and rhyolites. Earth Planet. Sci. Lett. 272, 158–171.

Wang, Q., Zhu, D.-C., Cawood, P.A., Zhao, Z.-D., Liu, S.-A., Chung, S.-L., Zhang, L.-L., Liu, D., Zheng, Y.-C., Dai, J.-G., 2015. Eocene magmatic processes and crustal thickening in southern Tibet: insights from strongly fractionated ca. 43Ma granites in the western Gangdese Batholith. Lithos 239, 128–141.

Woodhead, J.D., Hergt, J.M., 2005. A preliminary Appraisal of seven Natural Zircon Reference Materials for in Situ Hf Isotope Determination. Geostand. Geoanal. Res. 29, 183–195.

Xia, Y., Xu, X., Niu, Y., Lei, L., 2018. Neoproterozoic amalgamation between Yangtze and Cathaysia blocks: the magmatism in various tectonic settings and continent-arc-continent collision. Precambrian Res. 309, 56–87.

Xu, Y.-G.A., Menzies, M., Thirlwall, M., Xie, G.H., 2001. Exotic Lithosphere Mantle Beneath the Western Yangtze Craton: Petrogenetic Links to Tibet Using Highly Magnesian Ultrapotassic Rocks *Geology* **29**. Geology 29.

Yang, K.H., 1998. A Plate Reconstruction of the Eastern Tethyan Orogen in Southwestern China, Mantle Dynamics and Plate Interactions in East Asia.

Zeng, L., Gao, L.-E., Xie, K., Liu-Zeng, J., 2011. Mid-Eocene high Sr/Y granites in the Northern Himalayan Gneiss Domes: melting thickened lower continental crust. Earth Planet. Sci. Lett. 303, 251–266.

Zhang, L.-S., Schärer, U., 1999. Age and origin of magmatism along the Cenozoic Red River shear belt, China. Contrib. Mineral. Petrol. 134, 67–85.

Zhao, X., Mo, X.X., Yu, X.H., Lu, B.X., Zhang, J., 2003. Mineralogical characteristics and petrogenesis of deep-derived xenoliths in Cenozoic syenite porphyry in Liuhe, western Yunnan province. Earth Sci. Front. 10, 93–104 (in Chinese with English abstract).

Zhao, Z., Mo, X., Dilek, Y., Niu, Y., DePaolo, D.J., Robinson, P., Zhu, D., Sun, C., Dong, G., Zhou, S., Luo, Z., Hou, Z., 2009. Geochemical and Sr–Nd–Pb–O isotopic compositions of the post-collisional ultrapotassic magmatism in SW Tibet: petrogenesis and implications for India intra-continental subduction beneath southern Tibet. Lithos 113, 190–212.

Zhu, D.-C., Zhao, Z.-D., Niu, Y., Dilek, Y., Hou, Z.-Q., Mo, X.-X., 2013. The origin and pre-Cenozoic evolution of the Tibetan Plateau. Gondwana Res. 23, 1429–1454.